Max-Planck-Institut
für Meteorologie

MAX-PLANCK-GESELLSCHAFT

International Max Planck Research School
on Earth System Modelling

Using CALIPSO and CloudSat satellite retrievals to evaluate low-level cloud parameterizations in ECHAM5 for cloud-climate feedback implications

Christine Cheung-Wai Nam

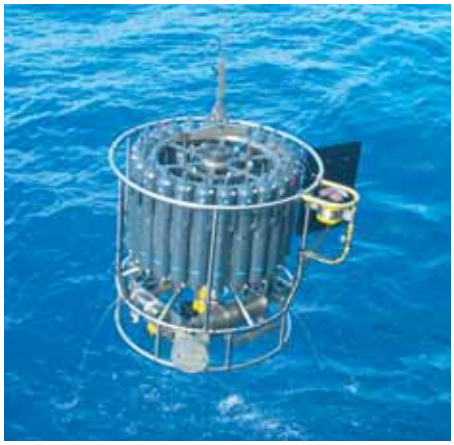

Berichte zur Erdsystemforschung 88/2011

Reports on Earth System Science

Hinweis

Die Berichte zur Erdsystemforschung werden vom Max-Planck-Institut für Meteorologie in Hamburg in unregelmäßiger Abfolge herausgegeben.

Sie enthalten wissenschaftliche und technische Beiträge, inklusive Dissertationen.

Die Beiträge geben nicht notwendigerweise die Auffassung des Instituts wieder.

Die "Berichte zur Erdsystemforschung" führen die vorherigen Reihen "Reports" und "Examensarbeiten" weiter.

Notice

The Reports on Earth System Science are published by the Max Planck Institute for Meteorology in Hamburg. They appear in irregular intervals.

They contain scientific and technical contributions, including Ph. D. theses.

The Reports do not necessarily reflect the opinion of the Institute.

The "Reports on Earth System Science" continue the former "Reports" and "Examensarbeiten" of the Max Planck Institute.

Anschrift / Address

Max-Planck-Institut für Meteorologie
Bundesstrasse 53
20146 Hamburg
Deutschland

Tel.: +49-(0)40-4 11 73-0
Fax: +49-(0)40-4 11 73-298
Web: www.mpimet.mpg.de

Layout:

Bettina Diallo, PR & Grafik

Titelfotos:
vorne:
Christian Klepp - Jochem Marotzke - Christian Klepp
hinten:
Clotilde Dubois - Christian Klepp - Katsumasa Tanaka

Berichte zur Erdsystemforschung 88/2011

Using CALIPSO and CloudSat satellite retrievals to evaluate low-level cloud parameterizations in ECHAM5 for cloud-climate feedback implications

Christine Cheung-Wai Nam

aus Saskatoon, Canada

Hamburg 2010

Reports on Earth System Science 88/2011

ISSN 1614-1199

Christine Cheung-Wai Nam
Max-Planck-Institut für Meteorologie
Bundesstrasse 53
20146 Hamburg
Germany

Als Dissertation angenommen
vom Department Geowissenschaften der Universität Hamburg

auf Grund der Gutachten von
Prof. Dr. Björn Stevens
und
Dr. Johannes Quaas

Hamburg, den 22. November 2010
Prof. Dr. Jürgen Oßenbrügge
Leiter des Departments für Geowissenschaften

ISSN 1614-1199

Using CALIPSO and CloudSat satellite retrievals to evaluate low-level cloud parameterizations in ECHAM5 for cloud-climate feedback implications

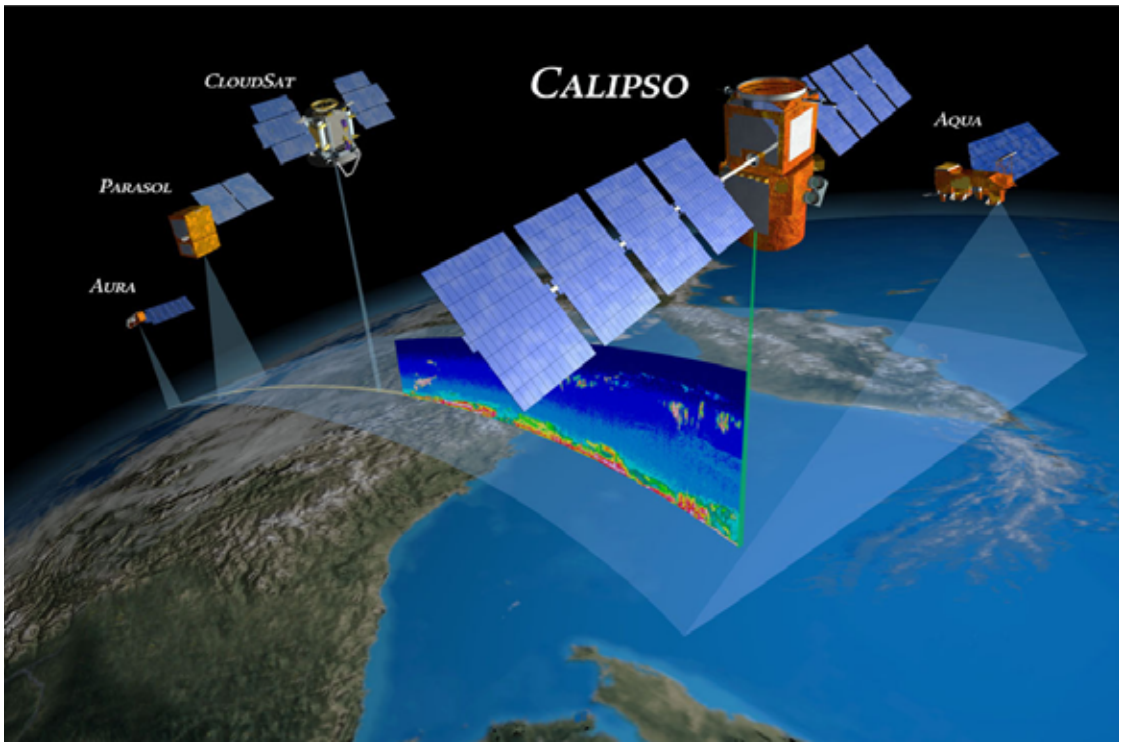

Christine Cheung-Wai Nam

Hamburg 2010

Title Page Image Credit: NASA Langley Research Center.
http://earthobservatory.nasa.gov/Newsroom/NasaNews/ReleaseImages/20050624/02_a-train%28CALIPSO%29.jpg

Acknowledgements

I would like to express my utmost gratitude to my supervisor Johannes Quaas for his advice, encouragement and enthusiasm throughout my Ph.D. work. I greatly appreciate his open door policy which always made me feel welcome to ask questions. I would also like to thank the members of my advisory panel, Björn Stevens, Marco Giorgetta and Martin Claußen for their valuable ideas and guidance during the course of my studies.

I would like to acknowledge Alejandro Bodas-Salcedo from the MetOffice and Sandrine Bony, Helene Chepfer and Gregory Cesana from the LMD for sharing their knowledge regarding the CALIPSO and CloudSat simulators. In addition, I would also like to acknowledge Erich Roeckner and Monika Esch from MPI-M, Roel Neggers from the KNMI and Ulrike Lohmann, Colombe Siegenthaler-Le Drian and Francesco Isotta from the ETHZ, for providing the code to the various boundary layer schemes.

The International Max Planck Research School on Earth System Modelling (IMPRS-ESM) has offered me many opportunities. Their financial support has allowed me to participate in many international collaborations and for that I am truly grateful. I would like to acknowledge the dedication shown by Antje Weitz and Cornelia Kampmann who go above and beyond their job descriptions to provide both administrative and moral support.

It was a great pleasure to be a part of the AES department; especially the Cloud-Climate Feedbacks group. Thank you to everyone for providing me with a wonderful working environment filled with scientific discussions and unfailing support. I would like to thank my colleagues: Sabrina Melchionna, Daniel Klocke, Louise Nuijens, Suvarchal Kumar, Thijs Heus, Irina Sandu, Swati Gehlot, Nadine Schneider, Torsten Weber, Karsten Peters, Francesca Guglielmo, Sebastian Rast and many, many others for sharing their vast knowledge and good spirits.

I was fortuitous to have had two incredible office-mates. The time, patience and energy Irene Stemmler and Katrin Lonitz spent debugging with me, discussing ideas, listening to rehearsals, and reading my theisis are both greatly appreciated and invaluable to me; but most of all I am thankful for the laughter which filled the office.

I want to thank Heather, Wendy, Monica, Kelly, Anna, Alysia, Jenny, Bhavanni, Faye, Sam, and Grace for the phone calls, cards, pictures and visits that made home feel much closer and to Bijal for providing me with a home away from home. Last but not least, I want to thank my mom, dad and Jen for their unconditional love and faith in me. With out them I could not have reached for the stars.

Ad Astra

Abstract

In recent decades the uncertainty in climate sensitivity has been traced back to cloud-climate feedbacks; a fact reiterated by the Intergovernmental Panel on Climate Change (Solomon et al., 2007). The magnitude which clouds respond to radiative forcings effectively determines the extent to which the Earth's temperature will amplify due to an increase in greenhouse gases. Boundary layer clouds, which reside in the lowest few kilometers of the atmosphere, are known to play a vital role in cloud-climate feedbacks. Currently, however, general circulation models are unable to realistically represent the cloudy boundary layer well.

This thesis uses cutting edge satellite retrievals from the CALIPSO and CloudSat satellites to evaluate different boundary layer cloud parameterization schemes in the ECHAM5 atmospheric general circulation model. The CALIPSO and CloudSat satellites host active lidar and radar instruments which provide global coverage of the vertical distribution of clouds and their properties. To compare CALIPSO and CloudSat retrievals with the ECHAM5 modelled output, the Cloud Feedback Model Intercomparison Project's CALIPSO and CloudSat simulators was first implemented into ECHAM5. The satellite simulators account for the sensitivity of the lidar and radar instruments, as well as the satellite's viewing geometry and perception of multi-layered clouds. This allows for a truer evaluation of the modelled boundary layer clouds with satellite retrievals.

Comparison of ECHAM5 with CALIPSO and CloudSat found that the geographical distribution of high-level clouds and cloud characteristics associated with the Hadley circulation are well captured. High-level cloud cover, however, is overestimated in certain situations; particularly for optically thin clouds. It was shown that an increase of the assumed ice crystal effective radius renders the highest level clouds detectable to the radar simulator, in better agreement with satellite retrievals. The increase in ice crystal effective radius also causes the lidar simulator to produce lower, more realistic scattering ratios and attenuating the lidar lower in the atmosphere, also in better agreement with the retrievals.

ECHAM5 was also shown to significantly underestimate the mid-level clouds, and even more so, the (Sub)Tropical low-level clouds. The low-level clouds which were produced were consistently perceived to be optically too thick by the lidar. In order to address these deficiencies, four boundary layer schemes were included within ECHAM5. They include: a standard convective mass-flux scheme (referred to as ECHAM5_Std; Tiedtke, 1989); a modified version of the Tiedtke (1989) scheme in which a new convective trigger alters the statistics of shallow convection (referred to as ECHAM5_Trig; Roeckner & Esch, 2010); a bulk parameterization of the effects of transient shallow cumulus clouds (referred to as ECHAM5_VSMF; Von Salzen & McFarlane, 2002; Isotta, 2010); and an eddy diffusivity Dual Mass Flux scheme adjusted to better represent shallow convection (referred to as ECHAM5_DMF; Neggers et al., 2009).

The four boundary layer parameterization schemes are run for first the present day climate. The question of how well does ECHAM5 represent clouds and precipitation in the present climate and whether the different representations of boundary layer clouds perform better compared to the CALIPSO and CloudSat retrievals is addressed. This is done by comparing the high, mid and low-level cloud cover maps derived by the lidar, the lidar and radar zonal hydrometeor fraction, lidar and radar joint cloud frequency-altitude histograms from the satellite retrievals and the model.

The evaluation of the ECHAM5_Trig, ECHAM5_VSMF and ECHAM5_DMF boundary layer cloud schemes found that all three schemes improved the representation of low-level clouds. The changes, however, were not always captured by the lidar and radar simulators; especially where there were fewer clouds. This is likely due to the fact that many of the new clouds were optically thin or lying beneath higher-level clouds. Although all three schemes increased the low-level cloud cover, including a significant amount by the ECHAM5_DMF, the schemes continued to underestimate the low-level cloud cover compared to satellite retrievals.

The radar reflectivity histograms showed that the three schemes have different distributions of moisture and cloud properties regardless of having similar projected cloud covers. The ECHAM5_Trig and ECHAM5_VSMF models increased the frequency of occurrence of high-level clouds and precipitation. In all versions of ECHAM5 the frequency of precipitation in ECHAM5 was found to be too high and its intensity too low. The schemes, however, did improve the frequency of large-scale precipitation; decreasing the number of low-intensity events and increasing the higher intensity events.

In order to assess cloud-climate feedbacks, and their sensitivity to boundary layer clouds, idealized climate change experiments were performed. In these experiments, the comparison of the cloud-climate feedbacks of the ECHAM5_Std, ECHAM5_Trig and ECHAM5_VSMF models showed that all three have positive, highly-sensitive cloud-climate feedback parameters. The three cloud-climate feedback parameters are of similar magnitude due to similar projected cloud covers.

Sensitivity experiments with the ECHAM5_Trig model showed that experiments with fewer present day low-level clouds produced lower cloud-climate feedbacks; whereas experiments with a greater amount of present day low-level cloud cover produced higher cloud-climate feedbacks. If indeed the present day low-level cloud cover is related to the cloud-climate feedback, then cloud-climate feedbacks to date may be underestimated as many general circulation models underestimate low-level cloud cover.

Zusammenfassung

In den letzten Jahrzehnten wurden, wie wiederholt auch vom Weltklimrat betont, Unsicherheiten in Bezug auf die Sensitivität des Klimas auf Rückopplungsmechanismen zwischen Wolken und Klima zurückgeführt. Das Ausmaß der Erderwärmung in Folge ansteigender Treibhausgaskonzentrationen wird im wesentlichen dadurch bestimmt, wie stark Wolken auf Strahlungsantriebe reagieren. Es ist bekannt, dass Grenzschichtwolken, d.h. Wolken, die in den unteren Kilometern der Atmosphäre vorkommen, eine wichtige Rolle für die Wolken-Klima-Wechselwirkungen spielen. Zur Zeit jedoch sind Modelle der allgemeinen atmospärischen Zirkulation nicht in der Lage Grenzschichtwolken realistisch abzubilden.

In dieser Arbeit werden aktuelle Daten der Satelliten CALIPSO und CLOUDSAT verwendet, um verschiedene Parameterisierungen von Grenzschichtwolken in dem atmosphärischen Zirkulationsmodell ECHAM5 zu evaluieren. CALIPSO und CLOUDSAT sind Träger von Lidar- und Radar-Instrumenten, welche mit globaler Abdeckung vertikale Verteilungen von Wolken und ihren Eigenschaften liefern. Um die Satellitendaten mit den Modellresultaten von ECHAM5 zu vergleichen, wurden die CALIPSO- und CLOUDSAT-Simulatoren des "Cloud Feedback Model Intercomparison Project″ in ECHAM5 implementiert. Die Satellitensimulatoren berücksichtigen Unsicherheiten der Lidar- und Radar-Instrumente, die Messgeometrie der Satelliten und deren Möglichkeit mehrschichtige Wolken zu beobachten, so dass ein verbesserter Vergleich der simulierten Grenzschichtwolken mit den Satellitendaten möglich ist.

Der Vergleich von ECHAM5 mit CLOUDSAT und CALIPSO erwies, dass die geographische Verteilung von hohen Wolken und Charakteristika von Wolken, die mit der Hadley-Zirkulation zusammenhängen, gut wiedergespiegelt werden, jedoch der Bedeckungsgrad hoher Wolken, insbesondere optisch dünner Wolken, in manchen Situationen überschätzt wird. Es wurde gezeigt, dass eine Erhöhung des apriori angenommenen effektiven Radius von Eiskristallen zu vom Radar-Simulator besser detektierbaren hohen Wolken führt, was in besserer Übereinstimmung mit Satellitenbeobachtungen ist. Zusätzlich führt die Erhöhung des effektiven Radiuses dazu, dass der LIDAR-Simulator niedrigere, realistischere Streuverhältnisse erzeugt, sowie dazu, dass die Extinktion des Signals des Lidar-Simulators weiter unten in der Atmosphre stattfindet. Auch diese Ergebnisse sind in besserer Übereinstimmung mit den Satellitenbeobachtungen.

Es wurde desweiteren gezeigt, dass ECHAM5 mittlere und, weiteraus stärker noch, (sub)tropische tiefe Wolken signifikant unterschätzt. Die simulierten tiefen Wolken wurden durchgehend vom Lidar als optisch zu dick erkannt. Um dieses Unvermögen in ECHAM5 genauer zu untersuchen wurden vier Schemata zur Parameterisierung von Grenzschichtwolken in ECHAM5 eingebaut: ein Standardschema für konvektiven Massenfluss (im Folgenden ECHAM5_Std genannt; Tiedtke, 1989); eine modifizierte Version

dieses Tiedke-Schemas (Tiedtke, 1989), in welchem ein neuer konvektiver Auslöser die Statistik der hochreichenden Konvektion verändert (ECHAM5_Trig; Roeckner & Esch, 2010), eine generische Parameterisierung der Effekte von (transienten) flachen Cumuluswolken (ECHAM5_VSMF; Von Salzen & McFarlane, 2002; Isotta, 2010); und ein zwei Massenflüsse berücksichtigendes Turbulenzsschema, welches so angepasst wurde, dass die flache Konvektion besser repräsentiert wird (ECHAM5_DMF; Neggers et al., 2009).

Für alle vier Parameterisierungen wurden zunächst Modellexperimente in einem aktuellen Klima durchgeführt um zu untersuchen wie gut ECHAM5 Wolken und Niederschlag simuliert und ob die verschiedenen Parameterisierungen von Grenzschichtwolken zu Verbesserungen der Modellresultate im Vergleich zu CALIPSO und CLOUDSAT Daten führen. Dazu wurden Vergleiche von vom Lidar bestimmten Bedeckungsgraden tiefer, mittlerer und hoher Wolken und zonale Hydrometeorkonzentrationen des Lidars und Radars betrachtet. Zusätzlich wurden kombinierte Lidar und Radar höhen-und frequenzaufgelöste Wolkenhistogramme aus Modellvorhersagen und Satellitenbeobachtungen untersucht.

Die Evaluierung der Resultate von ECHAM5_DMF, ECHAM5_Trig und ECHAM5_VDMF offenbarte, dass alle drei Parameterisierungen von Grenzschichtwolken die Repräsentation von tiefen Wolken im Modell verbessert. Änderungen wurden jedoch nicht immer vom Radar- und Lidar-Simulator detektiert, insbesondere nicht, wenn weniger tiefe Wolken simuliert wurden. Dies ist hchstwahrscheinlich dadurch zu begründen, dass die neuen Wolken optisch dünn waren oder unterhalb von hohen Wolken auftraten. Obwohl alle drei Schemata die Bedeckung tiefer Wolken erhöhten, insbesondere ECHAM5_DMF, wurde diese im Vergleich zu den Satellitendaten weiterhin unterschätzt.

Die kombinierten Lidar und Radar höhen-und frequenzaufgelösten Wolkenhistogramme zeigten, dass die drei Parameterisierungen zu unterschiedlichen Verteilungen von Feuchte und Wolkeneigenschaften führen, trotz ähnlicher simulierter Bedeckungsgrade. ECHAM5_Trig und ECHAM5_VSMF erhöhten die Häufigkeit von hohen Wolken und Niederschlag. In allen Versionen von ECHAM5 war die Niederschlagshäufigkeit zu hoch und die Niederschlagsintensität zu niedrig, obwohl eine Verbessung des großskaligen Niederschlags durch eine geringere Anzahl von schwachen Niederschlagsereignissen und größere Anzahl stärkerer Niederschlagsereignisse zu verzeichnen war.

Um die Wolken-Klima-Wechselwirkungen und den Einfluss von Grenzschichtwolken darauf zu untersuchen wurden Experimente mit einer idealisierten Klimanderung durchgeführt. Der Vergleich der Wolken-Klima-Rückkopplungen in ECHAM5_Trig, ECHAM5_Std und ECHAM5_VSMF zeigte, dass alle drei Modelle positive, stark sensitive Rückkopplungsparameter für den Wolken-Klima-Antrieb mit ähnliche Beträgen haben, aufgrund ähnlicher Bedeckungsgrade.

Sensitivitätsstudien mit ECHAM5_Trig zeigten, dass Experimente mit weniger tiefen Wolken im aktuellen Klima zu einer schwächeren Wolken-Klima-Wechselwirkung führten, während Experimente mit mehr tiefen Wolken im akutellen Klima zu einer stärkeren Wolken-Klima-Wechselwirkung führten. Sollte tatsächlich die Bedeckung der heutigen tiefen Wolken den Wolken-Klima-Antrieb beeinflussen, dann unterschätzen aktuelle Zirkulationsmodelle diesen, da sie den Bedeckungsgrad tiefer Wolken unterschätzen.

Contents

Acknowledgements **5**

Abstract **i**

Zusammenfassung **iii**

List of Abbrevations **ix**

1 Introduction **1**
1.1 Climate Sensitivity . . . 1
1.2 Cloud-climate-feedback . . . 1
1.3 General Circulation Models . . . 2
1.3.1 Clouds in GCMs . . . 2
1.3.2 Boundary layer clouds . . . 3
1.4 Satellite retrieval of cloud properties . . . 3
1.5 Satellite simulator . . . 4
1.6 Scope & Content of Thesis . . . 5

2 ECHAM5 Model Description **7**
2.1 ECHAM5 Model and Experiment Description . . . 7
2.2 Stratiform Cloud Scheme . . . 7
2.3 Convective Cloud Scheme . . . 8
2.4 Turbulence Scheme . . . 9

3 Satellites and Satellite Simulators **11**
3.1 Satellite Description . . . 11
3.1.1 CALIPSO . . . 12
CALIPSO Satellite Data . . . 12
3.1.2 CLOUDSAT . . . 15
CLOUDSAT Satellite Data . . . 15
3.1.3 ISCCP . . . 16
ISCCP Satellite Data . . . 17
3.2 CFMIP Observational Simulator Package . . . 18
3.2.1 CALIPSO Simulator . . . 18

3.2.2 CLOUDSAT Simulator . . . 22
3.2.3 ISCCP Simulator . . . 23
3.3 Summary . . . 24

4 Evaluating ECHAM5 clouds 25
4.1 Cloud Cover Maps: Active vs. Passive . . . 26
4.1.1 High-level Clouds . . . 27
4.1.2 Mid-level Clouds . . . 27
4.1.3 Low-level Clouds . . . 28
4.1.4 Cloud Cover Maps . . . 29
4.2 Zonal Hydrometeor Fraction: Lidar vs. Radar . . . 32
4.2.1 Zonal Hydrometeor Fraction: Lidar derived . . . 32
4.2.2 Zonal Hydrometeor Fraction: Radar derived . . . 34
4.2.3 Zonal Hydrometeor Fraction . . . 35
4.3 Lidar Scattering Ratio Joint Histograms . . . 36
4.3.1 Californian Stratocumulus . . . 37
4.3.2 Hawaiian Shallow Cumulus . . . 38
4.3.3 North Pacific . . . 38
4.3.4 Tropical West Pacific . . . 39
4.3.5 Lidar Scattering Ratio Histogram . . . 39
4.4 Sensitivity Experiments: Ice Radius and Content . . . 40
4.4.1 Impact on Lidar Simulator . . . 40
4.4.2 Impact on Radar Simulator . . . 43
4.4.3 Sensitivity Experiments Summary . . . 43
4.5 Radar Reflectivity Joint Histograms . . . 44
4.5.1 Californian Stratocumulus . . . 46
4.5.2 Hawaiian Shallow Cumulus . . . 47
4.5.3 North Pacific . . . 47
4.5.4 Tropical West Pacific . . . 48
4.5.5 Radar Reflectivity Histogram . . . 48
4.6 Non-Precipitating Radar Reflectivity Histograms . . . 49
4.7 Dynamical Regimes Radar Reflectivity Histograms . . . 51
4.8 Conclusions . . . 52

5 Comparing Boundary Layer Schemes 57
5.1 Boundary Layer Scheme Descriptions . . . 58
5.1.1 Convective Mass-flux with Modified Convective Trigger . . . 58
5.1.2 Bulk Parameterization: Effects of transient shallow cumulus . . . 58
5.1.3 Dual Mass Flux . . . 59
5.2 Comparison of Boundary Layer schemes . . . 63
5.2.1 Differences in purely modelled cloud cover . . . 63
Differences in high-level cloud cover . . . 63

Differences in mid-level cloud cover . . . 64
Differences in low-level cloud cover . . . 64
Summary of differences of the purely modelled clouds . . . 65
5.2.2 Cloud Radiative Forcing . . . 65
5.2.3 Difference in lidar detected cloud cover . . . 67
Difference in lidar high-level cloud cover . . . 67
Difference in lidar mid-level cloud cover . . . 68
Difference in lidar low-level cloud cover . . . 68
Summary of differences in lidar cloud cover . . . 69
5.2.4 Using CloudSat Radar Observations and Simulator . . . 73
Difference in radar reflectivities to ECHAM5_Std . . . 73
Difference in radar reflectivities to CloudSat retrievals . . . 74
5.3 Changes in precipitation . . . 75
5.4 Conclusions . . . 76

6 Cloud Climate Feedbacks 79
6.1 Cloud-Climate Feedbacks . . . 80
6.2 Cloud-Climate Feedback: Comparison of Schemes . . . 81
Summary . . . 83
6.3 Convective Trigger sensitivity . . . 84
Summary . . . 88
6.4 Outlook: Application of Satellite Simulators . . . 89
6.5 Conclusions . . . 89

7 Conclusions and Outlook 91
7.1 Summary and Conclusions . . . 91
7.1.1 Evaluation of ECHAM5 . . . 92
7.1.2 Boundary Layer Schemes . . . 93
7.1.3 Cloud Climate Feedbacks . . . 94
7.2 Outlook . . . 95

Appendixes 96

A Parasol 101
A.1 PARASOL Retrievals and Simulator . . . 101
A.1.1 PARASOL Reflectivity Maps . . . 101
A.1.2 PARASOL Reflectivity Histograms . . . 102

List of Abbrevations

ACTISM	CALIPSO lidar simulator
ATB	Attenuated Backscatter
CALIOP	Cloud-Aerosol Lidar with Orthogonal Polarization
CALIPSO	Cloud-Aerosol Lidar and Infrared Pathfinder Satellite Observation
CAPE	Convective Available Potential Energy
CCF	Cloud-Climate Feedback
CFAD	Contour Frequency by Altitude Diagrams
CFMIP	Cloud Feedback Model Intercomparison Project
CLIMSERV	Service de donnes et de calcul de l'Institut Pierre Simon Laplace
CloudSat	Cloud Satellite
COSP	CFMIP Observational Simulator Package
CRF	Cloud Radiative Forcing
DMF	Eddy Diffusivity Dual Mass Flux
ECMWF	European Centre for Medium-Range Weather Forecasts
ERA-Interim	ECMWF reanalysis data set
GCM	General Circulation Model
GeoProf	Geometric Profile Data Set
GOCCP	GCM-Oriented CALIPSO Cloud Product
IIR	Imaging Infrared Radiometer
IPCC	Intergovernmental Panel on Climate Change
ISCCP	International Satellite Cloud Climatology Project
ITCZ	Intertropical Convergence Zone
JJA	June-July-August

KNMI	Koninklijk Nederlands Meteorologisch Instituut
LFC	Level of Free Convection
LNB	Level of Neutral Buoyancy
LTS	Lower Tropospheric Stability
LW	Longwave
MMF	Multiscale Modeling Framework
PDF	Probability Density Function
SCOPS	Subgrid Cloud Overlap Profile Sampler
SR	Scattering Ratios
SST	Sea Surface Temperature
SW	Shortwave
TKE	Turbulent Kinetic Energy
TOA	Top of Atmosphere
WFC	Wide Field Camera

Chapter 1

Introduction

The Earth's climate is a complex system of interactions amongst the atmosphere, hydrosphere, cryosphere, lithosphere and biosphere measured in timescales on the order of hours to millennia. As the climate changes over time, due to natural variability and anthropogenic influences, the interactions amongst these components will change. These changes will affect humanity by way of water scarcity, food security and transmission of disease. The significance of these impacts increases with an increased change to the Earth's mean surface temperature (Solomon et al., 2007).

1.1 Climate Sensitivity

Climate sensitivity, as defined by the Intergovernmental Panel on Climate Change (IPCC), is the change in the Earth's mean surface temperature with a doubling of greenhouse gases expressed as carbon dioxide equivalents, after equilibrium has been reached (Solomon et al., 2007). Climate sensitivity is dependent on many feedback parameters including water vapor, surface albedo, lapse rate and clouds. These feedback parameters can be positive and negative in sign implying they will either amplify or diminish the climate system's response, respectively. It has been shown that cloud feedbacks remain the largest source of uncertainty in climate sensitivity (Cess et al., 1990; Soden & Held, 2006; Ringer et al., 2006).

1.2 Cloud-climate-feedback

The cloud-climate feedback is dependent on the complex relationship clouds have with the climate system. Clouds influence climate through various processes including the transport of mass, moisture, heat and momentum throughout the atmosphere, as well as interacting with the Earth's radiation budget. Clouds have a significant influence on the Earth's radiation budget, both reflecting incoming short-wave solar radiation and absorbing outgoing

long-wave terrestrial radiation. Depending on a cloud's particle distribution, altitude, and thickness the effect of clouds on the radiation budget differs (Stubenrauch et al., 1997). Clouds that contain ice crystals in addition to liquid water particles have different reflection and absorption properties. High, optically thin cirrus clouds transmit most of the incoming solar radiation but trap outgoing terrestrial infrared radiation; conversely, low, optically thick cumulus clouds reflect solar radiation yet because its temperature is similar to the surface temperature, the emitted long-wave radiation is similar to the Earth's surface. These characteristics cause high, optically thin clouds to have a net warming effect on the earth's surface and low, optically thick clouds to have a net cooling effect. Changes to the altitude, thickness and composition; as well as the amount and geographical distribution of clouds in a perturbed climate can have a profound affect on the Earth's radiation budget. Currently the magnitude of cloud-climate feedbacks differs strongly amongst General Circulation Models (GCM) depending on how the clouds are represented.

1.3 General Circulation Models

State-of-the-art coupled GCMs represent the large-scale dynamics and interactions of the atmosphere, ocean, land (soil and vegetation) and cryosphere by solving a series of equations conserving mass, momentum and energy. These equations include the continuity equation (mass), equation of state (thermodynamics), and horizontal and vertical momentum. Within atmospheric GCMs, these equations are numerically solved in a discretized grid or in Fourier space; grids typically have resolutions of approximately 100-200 km horizontally and 100-500 m vertically. Processes which occur at scales much smaller than those resolved, including cloud cover and convection, are accounted for using parameterizations. Parameterizations endeavor to represent the collective effect of the small-scale processes in terms of the large-scale resolved variables.

1.3.1 Clouds in GCMs

In a GCM the collective effects of clouds are parameterized. This includes the effect of clouds on the Earth's radiation budget, as well as the distribution of moisture, mass, heat and momentum throughout the atmosphere. The effects depend on cloud type. Generally, clouds in a GCM are classified as either stratiform or convective clouds. It is generally assumed that only stratiform clouds affect the radiation, while only convective clouds affect the vertical transport of mass and momentum. Both cloud types, however, affect the distribution of heat (via condensation and evaporation) and precipitation. A detailed description of how clouds are represented in the ECHAM5 Atmospheric GCM is presented in the following section (See 2.1). This will include the representation of cloud

cover, stratiform and convective clouds and turbulent fluxes.

1.3.2 Boundary layer clouds

Boundary layer clouds, those within the lowest 3 km of the Earth's atmosphere, are directly affected by the surface topography and surface fluxes. The cloudy boundary layer is often classified into two cloud regimes: stratocumulus and shallow cumulus. Not only do these clouds cover a significant part of the Earth's surface, but they also have a large net radiative cooling effect (Harrison et al., 1990; Hartmann et al., 1992). Understanding how these clouds change in a perturbed climate is vital to the cloud-climate feedback problem.

Boundary layer clouds are largely determined by the turbulent kinetic energy and inversion strength. The turbulent kinetic energy is related to the coupling of various processes in the boundary layer, such as cloud top entrainment and radiative cooling, neither of which are properly represented in a GCM. The coarse vertical resolution of GCMs and the inability of the advection scheme to capture sharp gradients makes modelling the inversion difficult in GCMs. Since neither the turbulent kinetic energy nor inversion stability are modelled well, GCMs are currently unable to realistically represent boundary layer clouds; which is essential to cloud-climate feedbacks.

Each model employs a different parameterization of boundary layer clouds which deal with the representation of turbulent kinetic energy and inversion stability differently. In order to evaluate how well these parameterizations represent boundary layer clouds, it is helpful to compare the modelled clouds with observations.

1.4 Satellite retrieval of cloud properties

Evaluation of global models call for global observations. With their unique, un-obscured vantage point, satellites provide the best platform for observing clouds globally. Since the 1960s satellites have provided information regarding the composition, size, distribution and motion of clouds. The instruments onboard the satellites are able to retrieve these properties by measuring any of the following three radiative components: (i) solar radiation scattered by atmospheric particles, (ii) infrared radiation emitted by the clouds; or (iii) scattered radiation emitted by active instruments onboard the satellite. Active instruments are instruments which emit electromagnetic radiation and measure the returned signal, as opposed to passive instruments which measure the reflected incident or emitted electromagnetic radiation. The radiative components measured depends on the number and width of the instrument's spectral channels; as well as the viewing geometry (limb or nadir); swath width and spatiotemporal resolution of the instrument. In addition to an instrument's properties, the choice of orbit determines the temporal and spatial scale of the measurements. Instruments on-board geostationary satellites, which appear

stationary over the Earth, provide high-temporal sampling over a region. Comparably, sun-synchronous polar orbiting satellites, with their lower orbits, can pass over the same geographical area at the same time every day, providing global coverage in high-spatial resolution swaths.

Satellite retrievals comprise of three stages: (i) cloud detection, (ii) cloud attribute retrieval and (iii) data processing. The first stage, cloud detection, determines whether there is a cloud present or not within a pixel. The absence or presence of a cloud is defined by a cloud mask which is normally based on a threshold of radiance. This threshold differs over different background scenes. Clouds above high albedo surfaces, such as snow, deserts, or sun-glinted sea surfaces are difficult to distinguish from the surface in the visible spectrum. Thus, the detection of clouds greatly depends on the sensitivity, viewing angle, sampling area and resolution of the instrument. Additionally, the cloud detection algorithm is used to produce a cloud amount (i.e. number of cloudy pixels / total number of pixels) in aggregated products. Once a cloud has been identified, it's attributes are determined by a retrieval algorithm. Retrieval algorithms must overcome challenges related to cloud heterogeneity. For example, retrieval algorithms often assume clouds are homogeneous plane-parallel grid-boxes from which radiative properties are derived. In reality, however, the heterogeneous nature and irregular shape of clouds have different radiative properties. The irregular shape of clouds lead to 3-D shadowing effects which impact on the radiative properties and depending on the instrument's angle of view, can be significant (Seethala & Horváth, 2010). Lastly, as satellite coverage changes over the years, with the launch of new satellites and decommissioning of old satellites, it is necessary to take into account the sampling frequency when using data sets from different satellites. Areas which have had greater satellite coverage over longer periods of time may inadvertently bias the data products, and as such must be accounted for when applying the data set. Each of stage of satellite retrieval may inadvertently bias the satellite product due to assumptions.

1.5 Satellite simulator

Despite these biases, satellite retrievals remain very valuable for the evaluation of clouds in GCMs. To account for biases in the detection and retrieval algorithms of satellite retrievals, satellite simulators have been developed. Satellite simulators facilitate the comparison of GCMs with satellite data by accounting for: an instrument's sensitivity (using the same thresholds employed in the cloud detection algorithm); accounting for the satellite's viewing geometry; and perception of multi-layered clouds.

The definition of cloud and cloud amount differs amongst both GCM models and amongst satellite retrievals, and as such the comparison between modelled clouds and those retrieved by satellites requires a consistent definition (Chepfer et al., 2010). One manner to do so is via satellite simulators. Satellite simulators take atmospheric profiles

of modelled variables such as temperature, pressure, cloud water content and cloud fraction, then mimics the retrieval, including its sensitivity and assumptions, to produce a cloud field consistent with satellite retrievals. Simply put, satellite simulators strive to diagnose the quantities as would be seen by the satellite if it was flying above an atmosphere similar to that predicted by the model (Chepfer et al., 2010).

1.6 Scope & Content of Thesis

This work assesses ECHAM5's representation of clouds and precipitation in the present climate using CALIPSO and CloudSat satellite retrievals, as well as evaluates different representations of boundary layer clouds for the purposes of better understanding cloud-climate feedbacks. It does so by asking the following three questions:

- How well does ECHAM5 represent clouds and precipitation in the present climate?
- How do different representations of boundary layer clouds in the ECHAM5 GCM improve the present cloud and precipitation distributions?
- How do cloud-climate feedbacks differ due to different representations of low-level clouds?

These questions are addressed by first using CALIPSO and CloudSat satellite retrievals to evaluate several low-level cloud parameterizations in ECHAM5 for cloud-climate feedback implications. CALIPSO and CloudSat retrievals offer the *first* global profile of the vertical structure of clouds in the atmosphere from satellites. A detailed description of the CALIPSO and CloudSat satellites, in addition to the satellite products used in this work are presented in Chapter 3.

In order to compare CALIPSO and CloudSat satellite retrievals with ECHAM5 modelled output, the Cloud Feedback Model Intercomparison Project's (CFMIP) CALIPSO and CloudSat simulators have been implemented in ECHAM5 (see Chp. 3). The initial comparison of ECHAM5 using the satellite simulators and satellite retrievals, presented in Chapter 4, compares the cloud cover distribution of high, middle and low clouds, zonal cloud fraction, radar reflectivities and lidar scattering ratios.

This study focuses its evaluation of ECHAM5 on the low-level cloud scheme. Three new boundary layer schemes are applied within ECHAM5 and compared to both the standard ECHAM5 model and satellite retrievals. These three boundary layer schemes include: a modified version of the Tiedtke (1989) scheme in which a new convective trigger alters the statistics of shallow convection; a bulk parameterization of the effects of transient shallow cumulus clouds (Von Salzen & McFarlane, 2002); and an Eddy Diffusivity Dual Mass Flux (DMF) scheme adjusted to better represent shallow convection (Neggers et al., 2009). The description of these three schemes and their evaluation are presented in Chapter 5.

Lastly, the low-cloud parameterization schemes are run for both the present day climate and in an idealized climate change scenario. From this, their corresponding cloud-climate feedbacks are calculated. The results are presented in Chapter 6. This chapter will be followed by Chapter 7 which contains a summary of the main findings of the thesis and the conclusions.

Chapter 2

ECHAM5 Model Description

2.1 ECHAM5 Model and Experiment Description

This study uses the atmospheric general circulation model ECHAM5 developed at the Max Planck Institute for Meteorology (Roeckner et al., 2003). ECHAM5 solves the prognostic equations for temperature, vorticity, divergence, logarithm of surface pressure, and the mass mixing ratios of water vapor and cloud liquid and ice water (Roeckner et al., 2003). The equations are solved on a hybrid terrain-following sigma-pressure 31 vertical level coordinate system (denoted as L31). The spectral transform method with triangular truncation at wavenumber 63 (T63), which corresponds to a resolution of 1.8 ° x 1.8 ° (∼200 km x ∼200 km), is used. They are evaluated using a semi-implicit leapfrog time integration scheme with a time-step (Δt) of 12 Min. At each grid point, the water vapor, cloud liquid water and cloud ice are transported using a flux form semi-Lagrangian transport scheme (Lin & Rood, 1996). From these prognostic grid-mean variables, clouds and their properties are parameterized. ECHAM5 parameterizes clouds in two manners - stratiform and convective clouds. A brief description of the parameterizations for stratiform cloud formation, cloud cover, cumulus convection and turbulence are described below. Further information can be found in Roeckner et al. (2003), including detailed descriptions of the radiation scheme, cloud micro-physics, and parameterizations for surfaces processes such as heat and water budget, gravity wave drag, orbit variation, and sub-grid scale orography.

2.2 Stratiform Cloud Scheme

As previously mentioned, the cloud fraction of each grid-box must be first determined in order to calculate the radiative impacts of clouds. In ECHAM5 the cloud fraction can be determined using either: Sundqvist et al. (1989) which parameterizes cloud fraction as a nonlinear function of grid-box mean relative humidity, or Tompkins (2002) which calculates cloud fraction from a statistical sub-grid scale distribution of total water content. For this

study the latter is used.

The cloud fraction in the Tompkins (2002) statistical cloud scheme is determined by integrating over the saturated part of the total water mixing ratio probability density function (PDF). The total water mixing ratio is calculated from the mass mixing ratios of water vapor, cloud liquid water and cloud ice. These in turn have been calculated prognostically using the bulk cloud micro-physics scheme presented in Lohmann & Roeckner (1996). The cloud micro-physics scheme accounts for phase changes between water via condensation/evaporation, deposition/sublimation, and freezing/melting; and precipitation via autoconversion, accretion, and aggregation.

The shape of the PDF, defined by the variance and skewness parameters, is related to sub-grid scale processes such as turbulence and convection. Turbulence governs the width of the distribution and convection mainly governs the skewness. A wider PDF implies there is a wide range of total water mixing-ratios within the grid box. A positively skewed PDF implies there are areas with concentrate water contents, e.g. convective cells.

Once the cloud fraction of a grid-box is know, the projected 2-D total cloud cover can be determined. Total cloud cover, for the purposes of this study, is the area covered by clouds if one looked down upon a column of atmospheric grid-boxes. The vertical cloud overlap is often applied in one of three manners: maximum, random or maximum-random overlap assumption (Nam, 2007). In this study cloud cover is determined by assuming maximum-random overlap.

In summary, the stratiform clouds are represented by three components: prognostic equations for water vapor, cloud liquid and ice; a micro-physical scheme, followed by a cloud cover scheme.

2.3 Convective Cloud Scheme

The convective parameterization scheme within ECHAM5, representative of an *ensemble* of convective clouds, is based on the mass-flux concept and bulk cloud model of Tiedtke (1989). In this scheme, cumulus convection is divided into three types: shallow, mid-level and penetrative convection. Shallow convection occurs when the surface evaporation is larger than the large-scale convergence of moisture into a column. Shallow convection is mainly driven by the turbulent surface moisture flux in the boundary layer. Conversely, penetrative convection, which is representative of deep tropical towers, occurs when large-scale convergence is greater than the surface evaporation. The representation of penetrative convection has been slightly modified according to a cloud-base mass-flux adjustment closure proposed by Nordeng (1994). Nordeng (1994) determines the cloud-base mass-flux from the convective available potential energy (CAPE). CAPE influences the vertical transport of heat and moisture, entraining and detraining cloud air with the

surrounding environmental air. Mid-level convection, which initiates above the boundary layer, forms when large-scale convergence at low levels is inhibited by a temperature inversion and instead air is lifted adiabatically to the lifting condensation level. If it is positively buoyant with respect to its surrounding, convection is activated.

Once convection occurs, convective clouds are represented by updrafts and downdrafts in steady state. Updrafts interact with the environment through convective entrainment and detrainment. Entrainment and detrainment are turbulent (lateral mixing) and/or organized (outflow at cloud top). The organized entrainment and detrainment rates of the ensemble are governed by the type of convection (shallow, mid-level, or penetrative). Within the bulk scheme, only one cloud type is present in each model grid box and so shallow clouds, which are more turbulent than deep clouds, have entrainment rates much larger than those used for deep convection. The organized entrainment for shallow clouds is based on a moisture convergence hypothesis, whereas for penetrative convection, organized entrainment occurs when the air parcel's buoyancy is positive (Roeckner et al., 2003). Organized detrainment for all cloud types occurs when the parcel's buoyancy becomes negative. The detrained cloud water at the cloud top, in addition to that of shallow non-precipitating cumulus clouds, is a source term in the stratiform cloud water transport equation (Lohmann & Roeckner, 1996). Following the calculation of the updraft bulk equations, the downdraft equations are calculated. Downdrafts arise when precipitation in updrafts evaporate, cooling mixtures of cloud and environmental air to its wet bulb temperature (Roeckner et al., 2003).

2.4 Turbulence Scheme

Turbulence plays a vital role in transfer of moisture, heat and momentum throughout the atmosphere. The exchange of heat and moisture can be broken up into two parts: (i) the tendency due to turbulent mixing and convection; and (ii) the tendency due to advection and diabatic processes. The latter of which is defined in terms of the large-scale specific humidity and temperature. The tendency due to turbulent mixing and convection, which occurs at sub-grid scales, is parameterized in terms of the large-scale model variables. In the ECHAM5 model, the convective term is parameterized in terms of the mass-flux described above and turbulent mixing is broken into two components: surface fluxes and those occurring above the surface layer. Turbulent surface fluxes for momentum, heat, and moisture are calculated using the bulk transfer model by computing the differences between the surface and the lowest model level for: wind velocity and transfer coefficients. The latter are obtained using Monin-Obukhov similarity theory by integrating the flux profile relationships between the surface and the lowest model level (Louis, 1979). Above the surface layer, turbulence is parameterized in using an eddy diffusion method terms of turbulent kinetic energy. This is described in detail in Chp. 5.1. The interaction between

clouds and turbulence occurs through the cloud top radiative cooling, the buoyancy flux and cloud top entrainment.

Chapter 3

Satellites and Satellite Simulators

3.1 Satellite Description

On April 28, 2006 the CALIPSO (Cloud-Aerosol Lidar and Infrared Pathfinder Satellite Observation) satellite was launched along with the CloudSat (Cloud Satellite) cloud profiling radar satellite. Together these two satellites produced the *first* global survey of the vertical structure of cloud systems; providing a 3-D perspective of the formation, evolution and distribution of clouds and aerosols (Fig. 3.1). As part of the A-train constellation of satellites, CALIPSO and CloudSat provide comprehensive measurements of the vertical profiles of clouds and precipitation, cloud ice and liquid water contents, cloud heights and multi-layered clouds; ultimately contributing to the understanding of cloud-radiation interactions (Stephens et al., 2002).

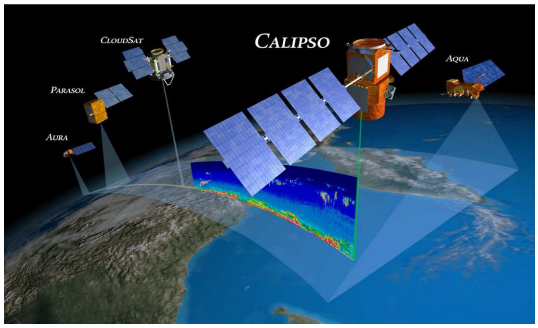

Figure 3.1— Vertical profile of clouds and aerosols as measured by the lidar instrument onboard CALIPSO. Background depicts the A-Train constellation of Earth-observing satellites. Image Credit: NASA Langley Research Center.
http://earthobservatory.nasa.gov/Newsroom/NasaNews/ReleaseImages/20050624/02_a-train%28CALIPSO%29.jpg

Both CALIPSO and CloudSat are in a sun-synchronous polar orbit 705 km above the sea surface with an inclination of 98.2 °. They cross the equator at approximately 13:30 hrs, local solar time, and have a 16-day repeat cycle providing coverage from 82 °S to 82 °N (Winker et al., 2007).

This chapter provides a detailed description of each satellite in turn. Special attention will be paid to lidar and radar instruments onboard. The cloud detection algorithms of each instrument and satellite data sets used in this study will also be reviewed. Lastly, an introduction to the CALIPSO and CloudSat satellite simulators will be presented.

3.1.1 CALIPSO

The CALIPSO satellite was designed to provide global profiling measurements of cloud and aerosol distributions (Winker et al., 2004). In order to provide high-resolution profiles of the vertical structure of clouds and aerosols, an active lidar instrument CALIOP (Cloud-Aerosol Lidar with Orthogonal Polarization) is used. CALIOP is a near-nadir two-wavelength polarization-sensitive lidar which uses one channel to measure the 1064 nm lidar backscatter intensity and two channels to measure the orthogonally polarized components of the 532 nm backscattered signal (Winker et al., 2007). At the 532 nm wavelength, atmospheric cloud particles and gas molecules contribute to scattering but not absorption and so the two-wavelength signals are able to provide information regarding particle size, shape (spherical vs. non-spherical) and type (Chepfer et al., 2008; Winker et al., 2007). As such CALIOP is also able to provide information regarding the micro-physical and optical properties of the clouds and aerosols.

The sampling resolution of CALIOP is a function of altitude. In order to capture the spatial variability of cloud and aerosols in the lower troposphere and weak atmospheric signals of the upper troposphere, the vertical resolution at 532 nm below 8 km is 30 m and 60 m above. Correspondingly, the horizontal resolution for 532 nm below 8 km is 333 m (along-track) by 75 m (cross-track) and 1 km by 75 m above. CALIOP has a pulse duration of 20 ns.

In addition to CALIOP, CALIPSO has a near-nadir imaging infrared radiometer (IIR) and a high-resolution wide field camera (WFC) onboard. The IIR is used for retrieving cirrus cloud emissivity and particle size with its non-scanning imager. The imager has a swath of 64×64 km^2 and a pixel size of 1 km and operates with three channels in the thermal infrared region (8.7 μm, 10.5 μm, and 12.0 μm) in addition to a microbolometer detector array and a rotating filter wheel. Together with the IIR, the WFC provides the radiances and reflectances of atmospheric particles. The WFC operates at 620 nm to 670 nm with a swath of 61 km and a spatial resolution of 125 m.

CALIPSO Satellite Data

For the purposes of this study the GCM-Oriented CALIPSO Cloud Product (CALIPSO-GOCCP) observational dataset, provided by the Institut Pierre Simon Laplace CLIMSERV, will be used. The CALIPSO-GOCCP dataset is derived from CALIOP Level 1B NASA Langley Atmospheric Sciences Data Center CALIPSO data sets. Level 1B data

profiles have been time-referenced, geo-located, and corrected for things such as offset voltage, background signals and instrument artifacts (Winker et al., 2006). Geolocation of CALIOP lidar profiles consists of determining the profile's height above the earth geoid from the footprint location, spacecraft altitude and ephemeris data. Geolocation accuracies are approximately 50 m in the horizontal and 10 m in the vertical (Winker et al., 2009). Calibration consists of converting the measured lidar signal profile into profiles of attenuated backscatter (i.e. measured loss of light intensity returned from the laser as it encounters atmospheric particles) (Winker et al., 2009). The Level 1B instantaneous profiles of the lidar Scattering Ratios (SR) (i.e., ratio of light scattered by particles to light scattered by molecules) are then averaged onto a GCM grid (Chepfer et al., 2008). Averaging onto a GCM grid means the retrievals and modelled data have the same horizontal and vertical resolution. Lastly, cloud diagnostics are then inferred from these profiles (Chepfer et al., 2010).

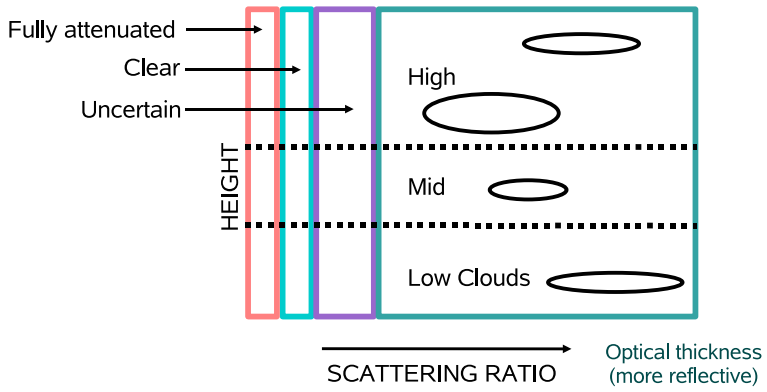

Figure 3.2— Schematic of lidar joint altitude-scattering ratio histogram. Frequency of occurrence for each lidar SR bin interval is plotted against height. The sum of a given altitude in a longitude/latitude box is normalized to 1.

The CALIPSO-GOCCP products of interest to this study include:

- ***Lidar Scattering Ratio Histograms*:** which show the frequency of occurrence of 15 different Scattering Ratio (SR) bins (x-axis) plotted as a function of height (y-axis) (Fig.3.2). The 15 SR are organized into the following bin intervals: 0, 0.01, 1.2, 3, 5, 7, 10, 15, 20, 25, 30, 40, 50, 60, 80, and 10000. The SR bin intervals indicate:

$SR < 0.01$	Lidar signal fully attenuated
$0.01 < SR < 1.2$	Clear sky
$1.2 < SR < 5$	Unclassified
$5 < SR$	Cloudy

The larger the particle number concentration, the greater the reflectivity. Highly reflective clouds, with SR $>$ 60, are associated with optically thick clouds while clouds with SR $<$ 20 are deemed optically thin (Chepfer et al., 2008).

- ***3D - Cloud Fraction*:** which contains the cloud fraction, clear fraction, and uncertainty fraction for retrievals at each longitude/latitude/altitude grid-box. The sum of these three fractions in a longitude/latitude/altitude box is equal to 1. The cloud detection algorithm in this product has an additional cloud threshold variable called DeltaATB, which aims to reduce the noise in the stratosphere. DeltaATB is set to 2.5 x $10^{-3} km^{-1} sr^{-1}$ and should $ATB - ATB_{mol} <$ DeltaATB clouds are deemed unclassified to avoid false cloud detection, as frequently occurring in the upper troposphere/lower stratosphere where ATB_{mol} is very low (Chepfer et al., 2010).

- ***Cloud Fraction Maps*:** which provide the low, mid, and high cloud fraction.

Low level clouds :	P $\geq$ 680 hPa	z $<$ 3.5 km
Mid level clouds :	680 $>$ P $\geq$ 440 hPa	3.5 $<$ z $<$ 7.2 km
High level clouds :	P $<$ 440 hPa	z $>$ 7.2 km

where P denotes cloud top pressures and z is cloud top height above sea level.

The lidar joint altitude-scattering ratio histograms, commonly known as lidar contour frequency by altitude diagrams (CFAD), will be studied for four different regions (Fig. 3.3).

North Pacific Fronts & Stratocumulus	30 ° - 60 °N ; 160 °E - 140 °W
Hawaiian Trade Cumulus	15 ° - 35 °N ; 160 °E - 140 °W
California Stratocumulus Region	15 ° - 35 °N ; 110 °W - 140 °W
Tropical Western Pacific (warm pool)	5 °S - 20 °N ; 70 °E - 150 °E

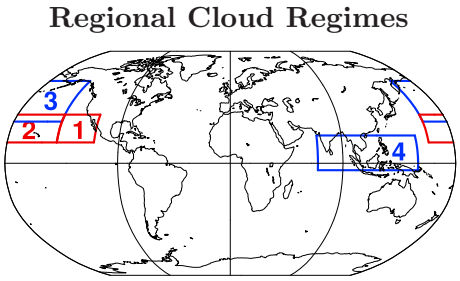

Figure 3.3— Geographical cloud regimes: (1) Californian Stratocumulus; (2) Hawaiian Trade Cumulus; (3) North West Pacific; (4) Tropical West Pacific.

Each region, as defined in Webb et al. (2001), has a different cloud regime affiliated with it; and as such each regime has a correspondingly distinct lidar signal. Comparison of the lidar CFADs allow us to compare cloud properties such as optical thickness, typical cloud height, and their frequency of occurrence.

3.1.2 CLOUDSAT

The CloudSat satellite has a 94 GHz, near-nadir millimeter-wavelength cloud radar onboard which probes the atmosphere and provides a vertical profile of clouds and precipitation. Cloud and precipitation particles, as in Marchand et al. (2009), will henceforth be collectively referred to as hydrometeors. The reflectivity of a hydrometeor is measured by the cloud radar as CloudSat passes overhead, creating a cross section through the atmosphere. With a pulse of approximately 3.3 μs, the hydrometeor reflectivity can be measured from the power of the backscattered radar beam as a function of distance from the radar. The measured hydrometeor reflectivities have a vertical resolution of $\sim$480 m and horizontal resolution of 1.7 km (along-track) by 1.4 km (cross-track).

CLOUDSAT Satellite Data

The CloudSat satellite data set, as with the CALIPSO-GOCCP data set, is provided by the Institut Pierre Simon Laplace (IPSL) CLIMSERV. The retrievals are based upon the operational CloudSat Geometric Profile data set 2B-GeoProf (hereafter GeoProf). GeoProf data contains a hydrometeor detection mask (indicating the likelihood hydrometeor presence and the probability of false detection), the radar reflectivity and estimation of gas absorption due to oxygen and water vapor (Marchand et al., 2008). Due to the fact that CloudSat operates at a shorter wavelength than most weather radars it is possible for CloudSat to become fully attenuated or have the measured return power be dominated by multiple scattering by hydrometeors (Mace et al., 2007; Marchand et al., 2008). As a result, CloudSat has a minimum detectable signal of approximately -30 dBZe and the lowest 1 km of reflectivities are commonly discarded due to ground clutter (Tanelli et al., 2008; Marchand et al., 2008).

As with the lidar retrievals, CloudSat's radar reflectivities will be constructed into contour frequency by altitude diagrams (CFAD). The same four cloud regions, will be compared with the modelled regions. The radar CFADs offers more detailed information than CALIPSO regarding the frequency of precipitating vs. non-precipitating clouds and are able to probe much deeper into the atmosphere before becoming attenuated.

The CloudSat cloud cover maps are determined by the GeoProf-2B Hydrometeor cloud detection algorithm described in Marchand et al. (2008). The cloud detection algorithm is briefly reviewed here. Upon measuring the power returned to the radar, a cloud mask is

created by determining whether an initial set of hydrometeor has been detected. Hydrometeors are detected by comparing the target power P_T (i.e. difference between the raw measured return power (P_{raw}) and mean power noise (P_n)), to the standard deviation of mean noise (σ_{Pn}). If $P_T > \sigma_{Pn}$, hydrometeors have potentially been detected, though due to noise there is a 16 % chance false detection. This initial detection mask undergoes a spatial box filter several times, and the raw return power is averaged in the along-track direction to increase the spatial correlation of the noise and target power. The new cloud mask is compared to a reduced resolution version of the previous mask, to avoid artificially expanding objects in the previous mask, and run through the spatial filter one last time. Finally, the likelihood of a hydrometeor's presence is determined (Fig.3.4).

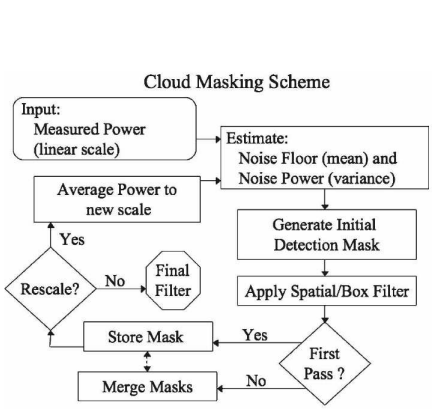

(a) Schematic of CloudSat cloud masking algorithm.

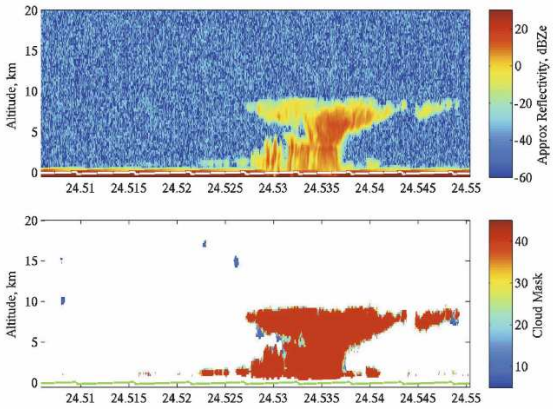

(b) Top: Radar reflectivity of convective and boundary layer clouds as seen by CloudSat; Bottom: CloudSat cloud mask.

Figure 3.4— CloudSat cloud masking algorithm (Marchand et al., 2008).

From this cloud mask, which also includes precipitation, a hydrometeor fraction is determined at a coarser aggregated grid. The hydrometeor fraction is defined as the number of retrievals at a specified altitude and latitude where a hydrometeor is detected relative to the number of retrievals (Marchand et al., 2009).

3.1.3 ISCCP

International Satellite Cloud Climatology Project (ISCCP), operational since 1983, is a collection of radiance measurements from five geostationary and two polar orbiting satellites (Rossow et al., 1996). These include the Tiros-N, INSAT, GMS, GOES, METEOSAT, and NOAA constellations. The aim of the ISCCP data product is to infer the global distribution of cloud radiative properties from satellite radiances to improve the modelling of cloud effects on climate (Schiffer, 1983).

ISCCP Satellite Data

This study uses the high, mid, and low-level cloud cover maps produced from the ISCCP retrievals provided by the IPSL's CLIMSERV website. The cloud cover maps which will be used have been based on the original ISCCP-D2 monthly mean data available from *http://eosweb.larc.nasa.gov/PRODOCS/isccp/table_isccp.html*. The ISCCP-D2 product is derived by combining satellite-measured radiances with the TOVS instrument atmospheric sounding profiles and surface data to obtain information regarding geographically mapped clear sky and cloudy sky radiances (Rossow & Schiffer, 1999). For each satellite data set the presence or absence of clouds in each image pixel is determined, the radiometric properties retrieved and then run through a cloud or clear sky radiation model to derive cloud and surface properties at pixel-level. The pixel-level results are summarized every 3 hours on an equal-area map with 280 km resolution and merged together from the separate satellites to produce a global coverage at each time. Finally the D2 data product is produced by averaging the D1 data product over each month, first at each of the eight three hour time intervals and then over all time intervals (Rossow & Schiffer, 1999).

The D2 product can be used to derive the cloud optical thickness (τ) from the visible channel and cloud top temperature, hence cloud top pressure, from the infrared channel (Gehlot, 2010). The cloud optical thickness and cloud top pressure are used to classify the clouds into nine cloud types. The cloud types can be further arranged to produce a high, mid and low-level cloud product as seen in Figure 3.5.

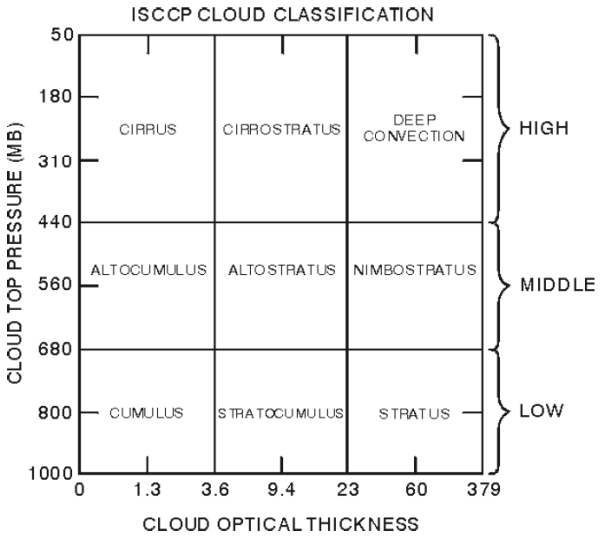

Figure 3.5— ISCCP cloud classification histogram (Rossow & Schiffer, 1999).

3.2 Cloud Feedback Model Intercomparison Project Observational Simulator Package

With the advent of active instruments onboard satellites, vertical profiles of clouds now can be measured at a global scale. The Cloud Feedback Model Intercomparison Project (CFMIP) Observational Simulator Package (COSP), using a common definition of cloud fraction, facilitates the comparison of clouds simulated by climate models with satellite retrievals in a more consistent manner. Modelled outputs are used to ascertain the quantities as would be seen by the satellite; known as the model-to-satellite approach (Chepfer et al., 2010). Within COSP version 1.2.1, which includes several satellite simulators, this study utilizes only the CALIPSO lidar simulator (ACTISM) (Chepfer et al., 2008) and the CloudSat radar simulator (QuickBeam) (Haynes et al., 2007). Utilization of satellite simulators allow for:

- Studies amongst *'satellite retrievals'* and *'model & satellite simulator'* results. The discrepancies between model and retrievals reveal biases in the model's cloudiness rather than differences in the definition of clouds or diagnostics (Chepfer et al., 2010).
- Studies between *'model & satellite simulator'* output and *'original modelled'* output. Comparison of what is originally produced by the model and what is visible to the simulated satellite sensors may allow one to identify properties which may exist in reality but are not captured in retrievals due to the instrument sensitivity.
- Systematic intercomparisons between models. Since the definition of clouds and cloud types differ amongst retrievals and models, the comparison between modelled and retrieved clouds requires a consistent definition of clouds (Chepfer et al., 2010). By utilizing the same definition of clouds, model intercomparison studies can be made more veraciously, allowing for the identification of those cloud regimes contributing the most to inter-model spread in clouds feedback and climate sensitivity (Webb et al., 2007).

3.2.1 CALIPSO Simulator

The ACTISM lidar simulator, as described in Chepfer et al. (2008), converts modelled atmospheric profiles of temperature, pressure, cloud fraction, and cloud condensate into the attenuated backscatter (ATB) signals. At the grid-scale, however, hydrometeor information within a GCM is on a scale of approximately 200 km. At this scale GCMs are generally unable to resolve the sub-grid variability of atmospheric variables; particularly cloud fields, which significantly impact the transfer of radiation through the atmospheric vertical column. As such sub-grid scale sampling procedures are needed before the scattering ratios

may then be compared directly with detected scattering ratios from CALIPSO. For this purpose the Subgrid Cloud Overlap Profile Sampler (SCOPS), developed by Klein & Jakob (1999) for the ISCCP simulator, is used.

SCOPS takes the cloud fraction and cloud condensate of each model grid-box and generates a sub-grid cloud distribution, identifying the areas within each grid-box which have cloud or are cloud-free (Fig. 3.6a). In order to identify this distribution of cloud and cloud-free areas each column is divided into sub-columns; which in our case equals 50. In each sub-column, the cloud fraction is assigned as either zero or one, such that the average over all sub-columns equals the modelled grid-averaged cloud fraction (Klein & Jakob, 1999; Chepfer et al., 2008). Amongst the cloudy sub-columns of each grid box, the liquid and ice is divided equally assuming a constant in-cloud water/ice content (Klein & Jakob, 1999).

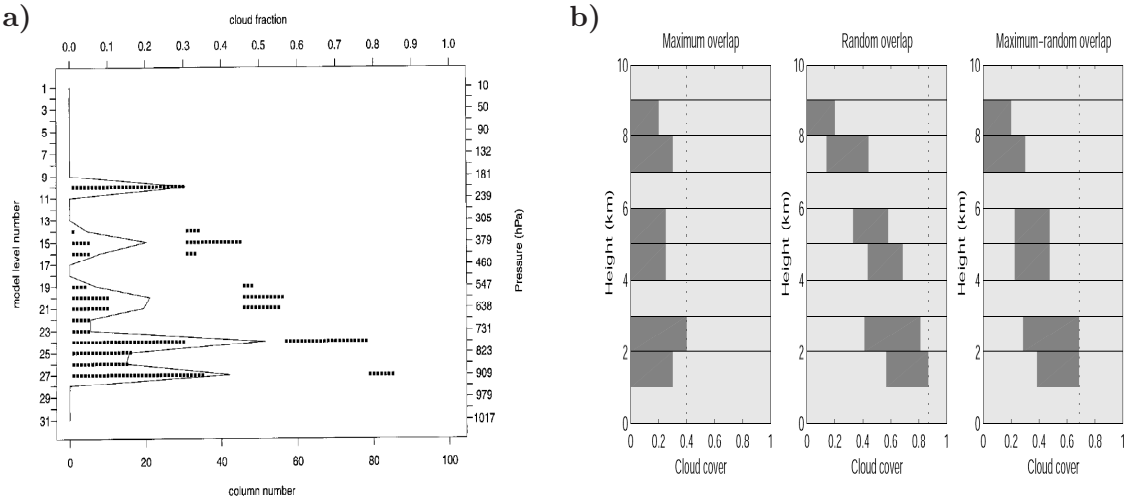

Figure 3.6— a) Vertical profile of cloud fraction (solid line) from ERA data for a single model grid-box. Solid black squares denote occurrence of a cloud at a given sub-column and model level as derived from SCOPS (Klein & Jakob, 1999). b) Schematic of cloud overlap assumptions (Hogan & Illingworth, 2000).

In order for SCOPS to generate sub-grid scale variability and to identify which clouds are visible from space from those which are obscured by higher lying clouds, the model's cloud-overlap assumption is used. The cloud-overlap assumption describes how clouds within a column lay over one another (i.e. multi-layered clouds). In our study ECHAM5, as with the European Centre for Medium-Range Weather Forecasts (ECWMF) model in Fig. 3.6a, the maximum-random overlap assumption is employed. Maximum-random overlap implies that clouds in adjacent vertical layers overlap maximally while groups of clouds separated by one or more clear layers are randomly overlapped. Whilst the cloud fraction at each level is the same, total cloud cover predicted by the three schemes differs greatly (Fig. 3.6b). This difference in total cloud cover can have a significant impact on the radiation budget and in our case the amount of cloud visible to the satellite; as

satellites identify clouds by their tops (Nam, 2007). Upon determining which sub-columns have clouds visible to the satellite, the cloud liquid (l) and ice water (i) mixing ratios within each sub-column are converted to particle concentrations:

$$N_{l,i} = x_{l,i} \frac{\frac{4}{3}\pi r^3 \cdot \rho_{l,i}}{\rho_d} \tag{3.1}$$

where the density of water (ρ_l), ice (ρ_i) and dry air (ρ_d) are determined from the model's pressure and temperature and the radius r is determined from a specified effective radius using the formula:

$$r_e = \frac{\int r^3 n(r) dr}{\int r^2 n(r) dr} \tag{3.2}$$

where n(r) is the particle size distribution. Once the particle concentration is known, the lidar backscatter coefficients ($\beta_{sca,mol}$, $\beta_{sca,part}$) $[m^{-1} sr^{-1}]$ and attenuation coefficients ($\alpha_{sca,mol}$, $\alpha_{sca,part}$) $[m^{-1}]$ for *molecules* and *particles* are calculated separately (Chepfer et al., 2008). The molecular properties ($\beta_{sca,mol}$, $\alpha_{sca,mol}$) (Eq. 3.3 & 3.4) are computed following *Collis & Russell (1976) (p.89, Eq.4.7)* (Chepfer et al., 2008).

$$\begin{aligned} \beta_{sca,mol} &= N_{mol} \cdot \frac{d\sigma_R(\pi)}{d\Omega} \\ &= \left(\frac{P(z)}{T(z)} \cdot \frac{N_a}{R_a}\right) \cdot \left(5.45 \left[\frac{\lambda(\mu m)}{0.55}\right]^{-4} \cdot 10^{-28} cm^2 sr^{-1}\right) \\ &= \frac{P(z)}{k \cdot T(z)} \cdot \zeta_{mol} \end{aligned} \tag{3.3}$$

$\beta_{sca,mol}$ is formally known as the molecular extinction coefficient of the air per volume, and informally known as the lidar backscatter from gas molecules. The gas molecules are much smaller than the laser wavelength and as such the molecular scattering can be described by the Rayleigh scattering approximation. N_{mol} is the molecular number density given in molecules cm^{-3} and $\frac{d\sigma_R(\pi)}{d\Omega}$ is the differential Rayleigh scattering cross-section where the scattering angle (θ) is equal to $\pi = 180°$. N_{mol} can be written as a function of pressure ($P(z)$), temperature ($T(z)$), Avogadro's Number (N_a) and individual gas constant for dry air (R_a = 286.9 J kg^{-1} K^{-1}) (Vergados & Shepherd, 2009). The term $\frac{d\sigma_R(\pi)}{d\Omega}$ can be written as a function of wavelength dependent Rayleigh scattering for the mixture of atmospheric gases below 100 km. Chepfer et al. (2008) further defines $\beta_{sca,mol}$ as a function of the Stefan Boltzmann constant (k=1.38×10^{-23} J K^{-1}) and a wavelength dependent variable ζ_{mol} which is equal to 6.2446×10^{-32} for 532 nm.

The molecular attenuation is defined as:

$$\begin{aligned} \alpha_{sca,mol} &\cong N_{mol} \cdot \sigma_{R} \\ &= \left(\frac{P(z)}{T(z)} \cdot \frac{N_a}{R_a}\right) \cdot \left(4.56 \left[\frac{\lambda(\mu m)}{0.55}\right]^{-4} \cdot 10^{-27} cm^2\right) \\ &= 8.0 \cdot \frac{\pi}{3.0} \cdot \beta_{sca,mol} \end{aligned} \tag{3.4}$$

which Chepfer et al. (2008) has written in terms of $\beta_{sca,mol}$. All other variables are as previously defined. The particle backscatter coefficient $\beta_{sca,part}$ (Eq.3.5) is related to the particle attenuation coefficient $\alpha_{sca,part}$ (Eq.3.6) and the backscatter-to-extinction ratio k_{part} $[sr^{-1}]$ in the following manner:

$$\beta_{sca,part}(z) = k_{part}(z)\alpha_{sca,part}(z) \tag{3.5}$$

$$\alpha_{sca,part}(z) = \int \pi r^2 Q(r) n(r,z) \mathrm{d}z \tag{3.6}$$

$$k_{part} = P(\pi)/4\pi \tag{3.7}$$

where r denotes the particle radius, *n(r,z)* the particle size distribution, *P(π)* the backscattering fraction of the phase function and *Q(r)* the scattering efficiency for cloud particles of radius r. In these equations aerosols are not considered. Cloud particles are assumed to be spherical, and as such, *P(π)* is parameterized as a function of the hydrometeors effective radius using Mie theory. Recalling that CALIOP operates at a wavelength of λ = 532 nm and that cloud particles are of a much larger size, *Q(r)* is set to its asymptotic value for non-absorbing particles of 2.

From equations Eq.3.3 to Eq.3.7, the total ATB lidar profiles for each sub-column can be calculated (Eq. 3.8). Here, the attenuation coefficient for gas molecules and particulate matter is integrated from the top of the atmosphere to some height z. A multiple scattering coefficient (η), whilst dependent upon the size, shape and density of the atmospheric particles and lidar footprint diameter, and thus continuously fluctuating, is set to 0.7 as has been determined for CALIOP in ice clouds by Winker (2003) (Chepfer et al., 2008). Following the calculation of the total ATB, the lidar SR for each sub-column can be derived as the ratio of total ATB over the molecular ATB signal (i.e. $\alpha_{sca,part}(\mathrm{z}) = 0$).

$$ATB(z) = (\beta_{sca,part}(z) + \beta_{sca,mol}(z)) \cdot e^{-2\eta \int_{TOA}^{z} (\alpha_{sca,part}(z) + \alpha_{sca,mol}(z)) \mathrm{d}z} \tag{3.8}$$

Since the scattering ratio is a function of the particle radius, for a given volume, the scattering ratio of many small particles is larger than the scattering ratio of a few large particles. This is because the sum of the surface area of the smaller particles is much greater that of the large particles.

The ACTISM lidar simulator creates cloud maps with a vertical grid of 41 levels equally

spaced 480 m apart starting from 0 km to 19.2 km above sea level. In the horizontal direction, diagnostics are spatially averaged over a horizontal grid of 3.5 ° x 2.5 ° for all variables (Chepfer et al., 2008). The cloud detection thresholds presented here are fully consistent to the cloud diagnostics from the CALIPSO-GOCCP satellite data.

3.2.2 CLOUDSAT Simulator

The QuickBeam radar simulator takes modelled profiles of pressure, temperature, cloud liquid and ice water content, effective radius, cloud cover, and precipitation mixing ratios in order to produce the vertical radar reflectivity profiles at 94GHz (the frequency used by CloudSat). Used in the top-down manner (i.e. satellite-based radar), the scattering properties of hydrometeors are determined using full Mie calculations based upon the hydrometeor size parameter and complex index of refraction. A second option exists to use precalculated look-up tables which are based upon the radar frequency, hydrometeor temperature, ice fraction and array of discrete particles. The look-up tables are more computationally efficient and generally have a reflectivity error of <2 dB compared to the full Mie calculations (Haynes et al., 2007). The radar beam can penetrate all clouds and most precipitation, however, at 94 GHz gaseous attenuation of the radar must be accounted for. This is done by calculating the scattering and absorption by atmospheric gases from modelled temperature and ambient relative humidity profiles. The reflectivity of a particle is a function of the particle's diameter to the sixth power and as such larger particles have much greater radar reflectivities than smaller particles.

The QuickBeam radar simulator includes the following assumptions and one should be aware of resulting limitations:

- ***All hydrometeors, including ice crystals, assumed spherical.*** Ice crystals are modeled using the maximum dimension as the diameter of the sphere. The highly variable nature of ice-crystal shape, density, index of refraction and its existence in mixed-phase clouds makes calculating an ice crystal's scattering ratio highly uncertain; as a result, the effective density and index of refraction are reduced to represent a mixture of ice with air (Liu, 2004; Haynes, 2007; Haynes et al., 2007). An option exists to specify a melted water content for snowflakes in order to represent the radar bright band associated with the presence of the melting layer (Haynes et al., 2007). This approximation is computationally efficient, but errors are incurred and a discrete-dipole approximation look-up table database for QuickBeam is being developed to help reduce these errors (Haynes, 2007).

- ***Neglect of multiple scattering.*** Multiple scattering effects are assumed to be negligible as they only play a role when rain rate exceeds 3 mm h^{-1} (Battaglia & Simmer, 2008; Marchand et al., 2009). For precipitation intensities

greater than a few millimeters per hour, large errors in reflectivity may be expected when simulating higher frequency radars, such as the space-borne CloudSat cloud radar. A correction for multiple scattering is being developed at this time and is expected to be included in future versions (Haynes, 2007).

- ***Sub-grid sampling of GCMs are necessary***. As with the ACTISM lidar simulator, sub-grid scale profiles of the atmosphere are needed before calculation of the radar reflectivities are useful. SCOPS is once again used to generate these sub-grid scale profiles.

3.2.3 ISCCP Simulator

The ISCCP satellite simulator used in this study was developed by Klein & Jakob (1999) and Webb et al. (2001) and further modified by Gehlot (2010). The ISCCP simulator, as with the CALIPSO and CloudSat simulators, is a diagnostic module run on-line in the ECHAM5 GCM. This subsection briefly summarizes the ISCCP simulator presented in detail in Gehlot (2010). The ISCCP simulator accounts for the fact that (i) passive satellite sensors identify clouds by the cloud tops and so the highest-level cloud within a column of multi-layered clouds will generally be identified by the satellite; and (ii) the altitude of optically thin clouds overlying optically thick clouds can be underestimated (Gehlot, 2010). Simply put, the ISCCP simulator shields low-level clouds lying below higher-level clouds from detection.

The vertical profile of the cloud amount, and in particular the information regarding which clouds are visible to, or respectively obscured from, the satellite is determined by SCOPS and the maximum-random overlap assumption (described in Section 3.2.1). The overlap assumption accounts for the vertical sub-grid variability (Klein & Jakob, 1999), while Gehlot (2010) accounts for the horizontal sub-grid variability using a horizontal sub-column generator developed by Raisanen et al. (2004). The horizontal sub-column generator uses the grid box mean values of cloud fraction, liquid water and ice content, in addition to the horizontal probability density function (PDF) of the total cloud water from the Tompkins cloud scheme and vertical maximum-random overlap assumption to stochastically generate either cloudy or clear sub-columns within each grid box (Gehlot, 2010). The vertical profiles are extracted and the ISCCP retrieval algorithms are applied. A grid-box mean cloud top pressure and optical thickness are then produced. These two variables are used to sort the clouds into cloud types and high, mid, and low-level cloud products as mentioned in Sec. 3.1.3.

3.3 Summary

Within GCMs clouds and cloud-related processes are often thought to be the greatest shortcoming. In order to improve their representation within ECHAM5, modelled clouds are evaluated with state-of-the-art retrievals from the CALIPSO and CloudSat satellites. The active lidar and radar instruments onboard these satellites allow for global measurements of 3D atmospheric profiles. The active lidar instrument is able to retrieve the heights of semi-transparent clouds and account for optically thin clouds which passive instruments are unable to do. In addition, the radar instrument is able to retrieve information regarding cloud liquid water and ice particle as well as precipitation. The ability of CALIPSO and CloudSat to detect more than one cloud layer has an important impact on the analysis of the radiative budget of the Earth as it may depend on the multi-layer structure clouds (Winker et al., 2009).

In order to make use of satellite retrievals in the evaluation of clouds in ECHAM5 one should include satellite simulators. The CALIPSO and CloudSat satellite simulators mimic the signals that would be retrieved by the satellite if it were above an atmosphere with the same physical properties as modelled by ECHAM5. The simulators take into account retrieval features, such as the identification of clouds by the cloud top, instrumental features and attenuation of active signals. Without satellite simulators a direct comparison between satellite retrievals and model output could be misleading. One would be comparing the total environment modelled with the limited environment which the satellite instrument is sensitive to. This study is the first to make use of active space-borne lidar and radar measurements as well as their simulators in the evaluation of ECHAM5. These results will be compared with the passive ISCCP satellite retrieval products.

Incorporation of satellite simulators allows for three separate comparisons. The first being, differences between *'satellite retrievals'* and *'ECHAM5 & satellite simulator'*. This comparison provides information regarding model performance and its shortcomings as the comparison only deals with the model output and with which CALIPSO and CloudSat can detect (Marchand et al., 2009). The second comparison with differences between the original *'ECHAM5'* output and the *'ECHAM5 & satellite simulator'* output can provide information regarding model properties and possibly elements which exist in reality but are not captured by the satellite. For example, effects of instrument sensitivity and attenuation by clouds and precipitation (Webb et al., 2007). Lastly, the accuracy of model *intercomparisons* will be greatly improved as the elements compared will have been defined in the same manner. For example, by calculating the lidar scattering ratios from the in-cloud liquid and ice mixing ratio; then using the same threshold for the delimitation of a cloud, the cloud amount is defined in a consistent manner. This is most useful as amongst models, the definition of cloud amount varies generally as function of the relative humidity or parameterized within a statistical scheme.

Chapter 4

Evaluating ECHAM5 clouds with CALIPSO and CloudSat Retrievals

How well does ECHAM5 represent clouds and precipitation in the present climate?

A comparison of the clouds modelled in ECHAM5 with the CALIPSO and CloudSat satellite retrievals is presented in this chapter. The active space-based instruments provide a unique data set to compare the vertical structure of clouds and precipitation in the atmosphere modelled by ECHAM5. Using the satellite simulators described in the previous chapter, this chapter aims to (i) reveal problems in the simulation of clouds, in particular the tropical low-level clouds, and (ii) identify causes and propose possible solutions using the lidar and radar simulators. If GCMs can demonstrate they produce the same features found in the satellite retrievals, it may be concluded that the key processes within the climate system have been accounted for and are accurately represented. If, however, models poorly reproduce cloud distributions in present-day simulations, it is unlikely these models will show much skill in reproducing cloud-climate feedbacks (Webb et al., 2001).

Comparing low-level clouds retrieved by satellites and modelled by ECHAM5 is not trivial. It is not possible to simply compare the low-level cloud cover and their associated scattering ratios and reflectivities. The lidar scattering ratio and radar reflectivity returned from low-level clouds to space depends greatly on the higher-level clouds above. The optical thickness of higher-level clouds governs the depth to which the lidar or radar signal penetrates into the atmosphere and the altitude at which the signals may attenuate. In fact, a first order limitation of retrievals from low-level clouds is attenuation of the lidar and radar signal from higher-lying clouds and hydrometeors. Thus, the vertical distribution of clouds must first be considered. This will done looking at the high, middle and low-level cloud cover maps followed by the zonal hydrometeor fraction. This will give us a greater

understanding when studying the regional and dynamical lidar and radar histograms.

These experiments have been run with COSP-v1.2.1 online in the ECHAM5 GCM for the year 2007 after an initial 3 month spin up. The results presented are for June-July-August (JJA) 2007. The experiments use the CALIPSO, CloudSat and modified ISCCP simulators as described in Chapter 3. The results are compared with the respective satellite data sets provided by the Institut Pierre Simon Laplace ClimServ website (*http://climserv.ipsl.polytechnique.fr/fr/cfmip-observations-2.html*). It should be noted that the focus of this study is on the CALIPSO lidar simulator and CloudSat radar simulator, not the results from the ISCCP simulator. For a detailed evaluation of ECHAM5 using the ISCCP simulator, please refer to Gehlot (2010).

4.1 Cloud Cover Maps: Active vs. Passive

The surface temperature, surface precipitation, and radiation budget at the top of the atmosphere are often used as measures to assess the performance of a GCM (Solomon et al., 2007). These factors are greatly influenced by the distribution of clouds throughout the atmosphere, horizontally, vertically and temporally. The simulated distribution of clouds amongst the high, mid, and low-levels, all of which have significantly different radiative impacts, differs greatly amongst different general circulation models (Chepfer et al., 2009). In the following section, the global distribution of clouds modelled by ECHAM5 will be compared with both active and passive satellite data sets.

The high, mid and low-level cloud cover maps of ISCCP and CALIPSO (GOCCP) satellite retrievals are compared with those modelled by ECHAM5 and emulated with the two simulators in Fig. 4.1. To identify the differences in cloud covers determined by passive and active instruments, this study will be broken up into three sections: high, mid, and low-level clouds. Within each section, the differences between the satellite retrievals will first be compared, followed by the differences between the satellite retrievals and simulators. Lastly, the conclusions which can be drawn about ECHAM5 will be discussed. This structured analysis will allow the features associated with satellite retrievals, satellite simulators and the model to be distinguished.

Table 4.1— Global-mean High, Mid and Low-level cloud cover [%] for June-July-August 2007 average.

Cloud Layer	ISCCP Satellite	ECHAM5 with ISCCP Simulator	ECHAM5 Model	ECHAM5 with CALIPSO Simulator	CALIPSO Satellite
Total	65.59	53.82	63.66	51.90	66.42
High (p <440 hPa)	22.77	19.54	40.65	32.48	31.80
Middle (440 hPa < p < 680 hPa)	18.83	11.96	21.20	9.50	23.23
Low (p > 680 hPa)	24.12	22.32	37.58	22.41	36.83

4.1.1 High-level Clouds

Both the ISCCP and CALIPSO satellite retrievals (Fig. 4.1 a,e) show the greatest amount of high-level cloud cover in the Tropics, near regions of deep convection. CALIPSO, with its 532 nm lidar instrument, is also sensitive to optically thin ice clouds ($\tau \sim 0.03$) and thus detects more clouds than ISCCP and has a greater high-level cloud amount (Table 4.1). An excellent example lies within the subsiding branch of the Hadley cell (30 °S) off the West coast of South America, where little to no high-level clouds appear in the ISCCP satellite data; however, a small fraction of high-level clouds are visible in the CALIPSO data set. Mimicking the satellite retrievals, the active CALIPSO simulator detects more high-level clouds than the passive ISCCP simulator (Fig. 4.1 b,d). The increase in high-level clouds detected can be directly associated with optically thin clouds produced by ECHAM5. Comparison of the high-level clouds from the CALIPSO and ISCCP simulators with their respective satellite retrievals shows that the distribution of high clouds modelled by ECHAM5 agrees well with satellite retrievals though optically thin, cirrus clouds are overestimated almost everywhere (e.g. over the Gulf of Mexico). The differences between the ISCCP and CALIPSO simulators indicate that nearly 30 % of the high-level clouds in ECHAM5 have $\tau < 0.3$ (Table 4.1). Comparing ECHAM5 pure model to the diagnostics with the ISCCP simulator, it is found that 50 % of the high-level clouds are optically thinner than $\tau = 0.3$. Tropical cirrus in ECHAM5, as described in Chp. 1, frequently stem from the moisture transported to the higher levels through the deep convective mass flux. Deep convection, in ECHAM5, has been shown to transport too much mass to the high-levels, resulting in an abundance of high-level cirrus which takes a longer time to sediment and evaporate out (Gehlot, 2010); hence the high cloud fraction in the subsidence regime of ECHAM5's high-levels. Lastly, the comparison between the pure model results and that diagnosed by the CALIPSO simulator (Fig. 4.1 c,d) shows that a substantial part of the high clouds which ECHAM5 produces are associated with scattering ratios lower than the threshold of 5 (approximately $\tau \sim 0.03$) applied in the cloud definition of the CALIPSO simulator. For example, over the Subtropical Pacific ocean these very thin clouds are frequenctly simulated. This implies there are even more optically thin high-level clouds modelled in ECHAM5 than could be detected by a lidar.

4.1.2 Mid-level Clouds

The mid-level cloud cover as seen by both satellites show very good agreement, with a global maximum in the Tropics and over the poles (Fig. 4.1 f,j). Though the mid-level cloud cover looks very similar between the two satellites, ISCCP has been known to overestimate the mid-level clouds. This is because the passive infrared sensors use the cloud top temperature to determine cloud top height and high thin cirrus clouds overlying lower, warmer clouds are often misdiagnosed ($\sim$ 15 - 25 % of the time) (Chen & Rossow,

2002; Raschke et al., 2005). Therefore, the difference in global means amongst the two satellite data sets may actually be greater than they appear (Table 4.1) and the agreement in mid-level clouds is due to a cancellation of errors in ISCCP. It should be noted that no conclusions can be drawn from the Southern Pole in the ISCCP retrievals (i.e. below the white line) because the retrievals used here rely partly on reflected solar radiation which is not present in polar winter. Comparison of the simulators with the satellite data sets show that ECHAM5 greatly underestimates mid-level clouds (Fig. 4.1 g,i). Though GCMs are notorious for underestimating mid-level clouds, it is important that the pure model results be taken into account. It can be seen that not all the mid-level clouds which are produced by ECHAM5 are detected by the CALIPSO simulator (Fig. 4.1 h,i). Thus, the lack of mid-level clouds detected by the lidar simulator is likely three-fold: over the Subtropical oceans, there is simply a lack of mid-level clouds generated by ECHAM5; in the Tropics there may be shielding by high-level clouds; and in the polar regions there may be optically thin cirrus which even the lidar does not define as cloud.

The ISCCP simulator detects a greater amount of mid-level clouds than the CALIPSO simulator. This is very likely the result of the misdiagnoses of high-level clouds overlying low-level clouds, previously described. Taking into account that ECHAM5 very frequently simulates very thin high-level clouds, the fact that the ISCCP mid-level cloud cover appears closer to the modelled cloud cover is merely an artifact. Regardless of the simulator's reduced detection, ECHAM5 generally produces fewer mid-level clouds compared to both satellite retrievals (Table 4.1).

4.1.3 Low-level Clouds

The ISCCP and CALIPSO satellite data both show a common maximum in low-level cloud cover in the stratocumulus regions and minimum over land (Fig. 4.1 k,o). In the polar regions, however, the two satellite retrievals differ. It is evident that CALIPSO detects a greater fraction of lower level clouds which can be attributed to the fact that active lidar can penetrate through optically thin clouds to detect multi-layered clouds; which passive instruments can not. Before the analysis of the simulated and modelled low-level clouds is presented, it should be noted that the wave like features in oceanic cloud cover in the model simulations (Fig. 4.1n, South Pacific) are due to the spectral representation of the orography. The ISCCP and CALIPSO simulators show similar peaks in low-level cloud cover in the stratocumulus regions, however, both simulators also show that ECHAM5 underestimates these clouds (Fig. 4.1 l,n), as well as all low-level Subtropical oceanic clouds (30 °N to 30 °S). In the vicinity of the South Pole the CALIPSO simulator appears to have underestimated the cloud cover compared to the satellite retrievals. Comparison of the CALIPSO simulator with the original ECHAM5 output indicates that the CALIPSO simulator does not detect the large amount of low-level polar clouds which ECHAM5

produces. Comparison with the high and mid-level CALIPSO simulator output indicates that it is likely higher-level clouds have attenuated the lidar signal near the South Pole. Therefore, no conclusion should be drawn about these low-level polar clouds in ECHAM5 as errors, such as an overestimate in higher-level clouds, propagate lower. The low-level clouds produced by ECHAM5 may be correct in these regions, however, an overestimation in high-level clouds may cause the lidar signal to attenuate high in the atmosphere rendering the low-level clouds undetectable.

4.1.4 Cloud Cover Maps

From the cloud cover maps, it can be concluded that CALIPSO's active instruments consistently detect more clouds than passive instruments. This is not surprising as CALIPSO was designed to be more sensitive to smaller cloud particles, and hence optically thinner clouds. The reason CALIPSO has a greater cloud cover than ISCCP, however, differs for each level. For high and mid-level clouds this is because CALIPSO is sensitive to the optically thin clouds which ISCCP is unable to detect. At the lower levels CALIPSO detects more clouds than ISCCP because it is able to penetrate through optically thin high-level clouds to underlying low-level clouds, for example, in the stratocumulus and shallow cumulus regions. ISCCP can only detect those clouds which are not obscured by higher clouds. In case of thin, high-level clouds above thick low-level clouds, ISCCP, using the top-of-atmosphere brightness temperature to estimate cloud top pressure, frequently mis-classifies such multi-layer clouds as single-layer thick mid-level clouds. Overall, the two satellite data sets show similar distributions of clouds. A comparison of the active and passive satellite data sets allows one to distinguish between the optically thick and optically thin fraction of the high-level clouds, the latter of which has a large impact on the radiative warming effects. The optical properties of the clouds in ECHAM5 are briefly discussed in Appendix A.

Despite differences in the satellite data sets, one can still identify model deficiencies. These deficiencies appear as consistent artifacts in the different comparisons with satellite data. Using the satellite simulators, one can deduce that the projected distribution of high-level clouds in ECHAM5 is modelled well, however, ECHAM5 overestimates optically thin clouds compared to the satellite retrievals. Mid-level clouds in ECHAM5 are evidently lacking, as shown by both the ISCCP and CALIPSO simulators. Low-level clouds in ECHAM5 are underestimated in the (Sub)Tropics compared to the retrievals, particularly the marine boundary layer stratocumulus and shallow cumulus clouds. One should be aware that overestimation of high-level clouds can attenuate the lidar signal within the satellite simulator limiting the analysis of low-level clouds in regions where high-level clouds are frequent.

The mean global total cloud covers presented in Table 4.1 show that the two satellite

data sets and satellite simulators, respectively, have similar values. The total cloud covers derived by the two simulators, however, indicate the ISCCP simulator has a greater total cloud cover than the CALIPSO simulator. This is because passive instruments account for the lower cloud layers in multi-layer clouds columns, and as such, the total cloud cover is derived by adding the high, mid and low-level cloud cover. Conversely, CALIPSO accounts for clouds in multiple layers, which in combination with a maximum-random subcolumn derived cloud fraction implies the lidar may arrive at a lower total cloud cover than ISCCP. Both simulators demonstrate that instrument sensitivity leads to an underestimation in the mean global total cloud cover compared to the pure model.

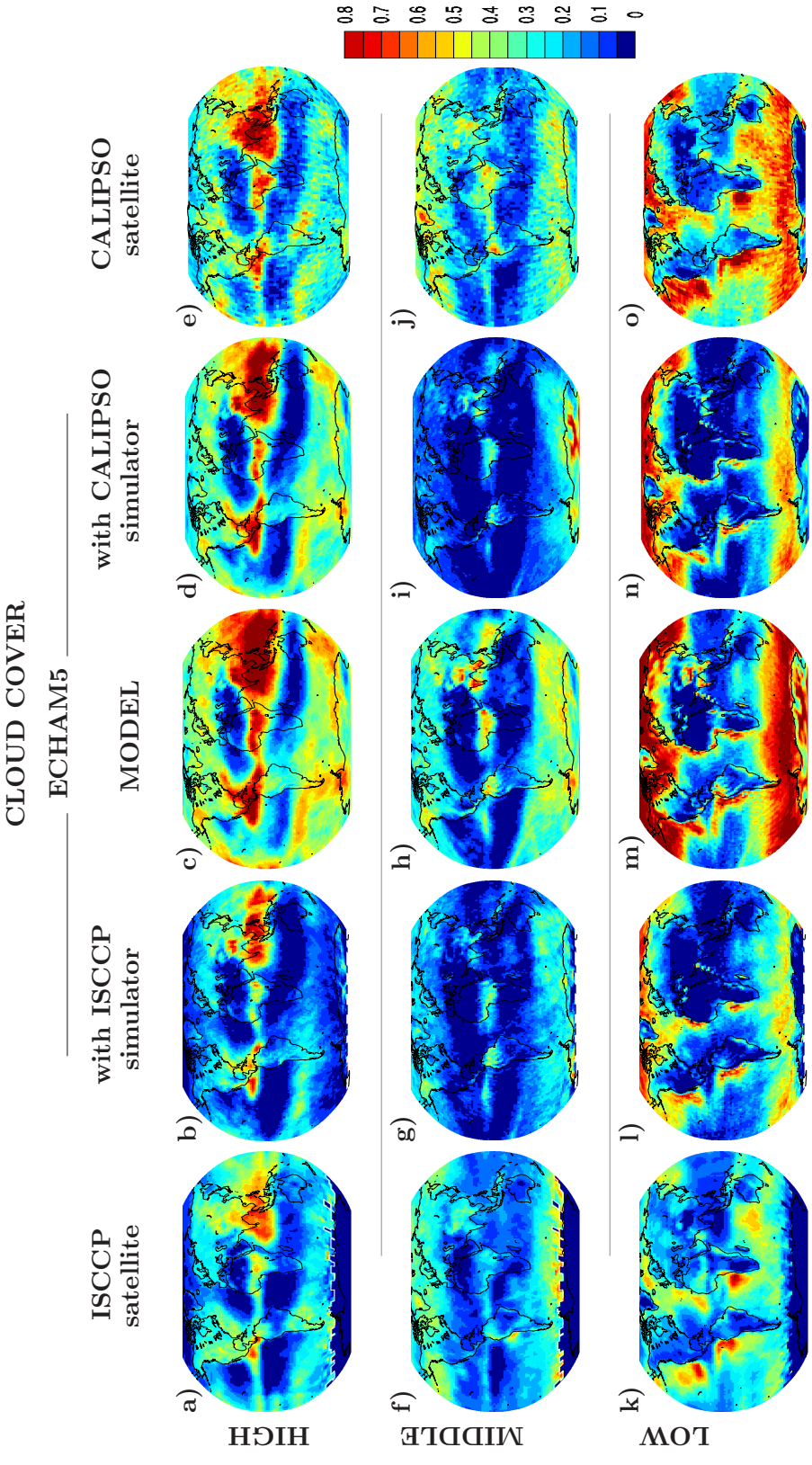

Figure 4.1— High ($p < 440$ hPa), mid (440 hPa $< p <$ 680 hPa), and low-level ($p >$ 680 hPa) cloud cover maps for JJA 2007. Left to Right: ISCCP Satellite Data; ECHAM5 with ISCCP simulator; ECHAM5 modelled data; ECHAM5 with CALIPSO simulator; GOCCP CALIPSO satellite data.

4.2 Zonal Hydrometeor Fraction: Lidar vs. Radar

For the first time, a global picture of the vertical structure of clouds is available from satellite retrievals, making the comparison between models and retrievals possible. The zonal hydrometeor fraction, as diagnosed from the lidar and radar onboard CALIPSO and CloudSat, respectively, are presented in Fig. 4.2 for JJA 2007. The lidar hydrometeor fraction is defined as ice or liquid particles with a scattering ratio > 5 (See Chp. 3.1.1). Comparably, the radar hydrometeor fraction is defined as particles with a radar reflectivity of $>$ -27.5 dBZe following Marchand et al. (2009). The hydrometeor fraction in each layer is defined by the number of positive identifications with reflectivity $>$ -27.5 dBZe divided by the total number of measurements in that layer (Bodas-Salcedo et al., 2008). It should be noted that in the satellite retrievals there is no polar coverage because both CALIPSO and CloudSat are near-nadir pointing on an inclined orbit and therefore do not obtain full polar coverage.

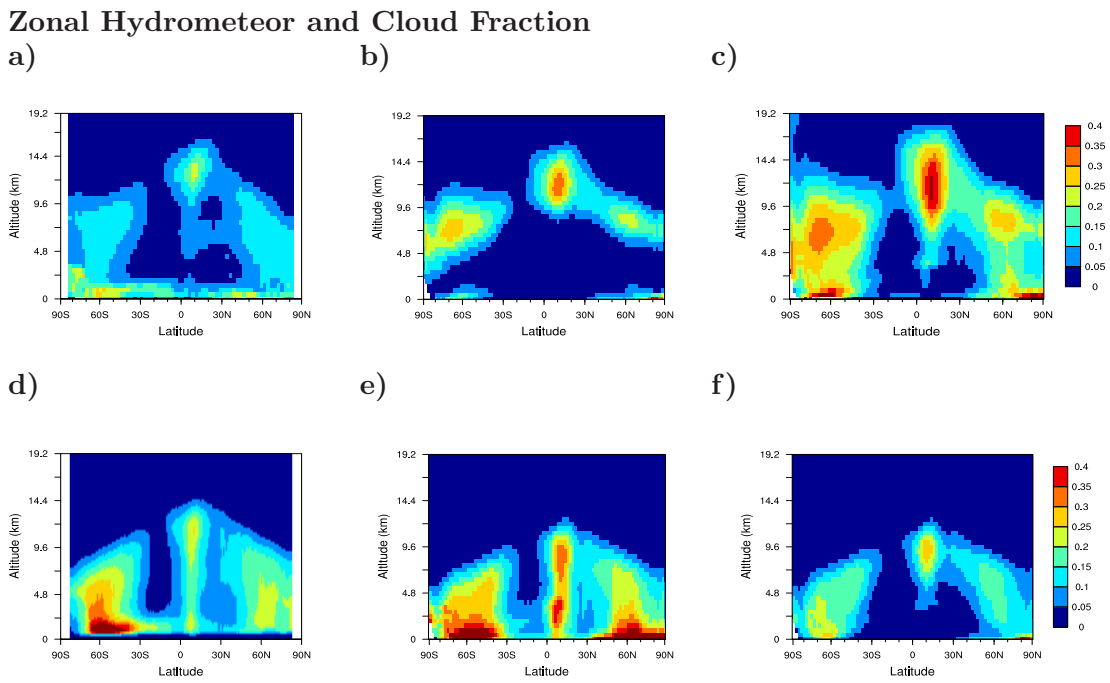

Figure 4.2— Zonal Hydrometeor and Cloud Fraction for JJA 2007. (a) CALIPSO GOCCP satellite data; (b) ECHAM5 with CALIPSO Simulator; (c) ECHAM5 cloud fraction; (d) CloudSat satellite data; (e) ECHAM5 with CloudSat Simulator; (f) ECHAM5 with CloudSat Simulator cloud fraction (-27.5 dBZe to -15 dBZe).

4.2.1 Zonal Hydrometeor Fraction: Lidar derived

The zonal hydrometeor fraction derived from the CALIPSO satellite retrievals and the lidar simulator are shown in Fig. 4.2a and Fig. 4.2b, respectively. These two plots are compared to the original ECHAM5 modelled cloud fraction (Fig. 4.2c). In the case of

lidars, the hydrometeor fraction can be equated with cloud fraction as the lidar signal becomes attenuated within optically thick clouds and under precipitating conditions.

From the CALIPSO satellite retrievals three distinct features can be identified: the high-level clouds in the ITCZ, the cloud-free subsiding branches of the Hadley cell and boundary layer clouds in the Subtropics (Fig. 4.2a). In the satellite retrievals high-level clouds at all latitudes, including the ITCZ, are often sufficiently thin to allow the lidar to penetrate deep into the atmosphere capturing the boundary layer clouds. This is not always the case for clouds modelled in ECHAM5. Compared to the satellite retrievals the lidar simulator shows that ECHAM5 overestimates the zonal mean cloud fraction of all high-level clouds by up to a factor of 2 (Fig. 4.2b). Whilst the cloud cover maps (Fig. 4.1) indicated high-level clouds in ECHAM5 were slightly overestimated in some regions, particularly in the ITCZ, neither the simulated cloud cover maps nor global mean shown in Table 4.1 suggested the extent was so significant. The average high-level cloud fraction from the lidar simulator agrees well with that from satellite retrievals, but in fact the overestimation of clouds in some areas are balanced out by the lack of clouds detected in other areas by the lidar simulator. The overestimation of high-level clouds in the Tropics, as previously mentioned, is caused by an overestimate of the cloud base mass-flux in the Tiedtke (1989) convective scheme (Neggers et al., 2004), which likely causes the lidar to attenuate high in the atmosphere, rendering the mid & low-level clouds produced by the model undetected (Fig 4.2c). Fig. 4.3 shows that the frequency of occurrence of lidar attenuation in ECHAM5 is much greater than for satellite retrievals. The causes of lidar attenuation, in particular the altitude in which attenuation occurs, will be studied further in the following section. As such, only a few conclusions can be drawn regarding the low-level clouds in ECHAM5 using the zonal cloud fraction derived from the lidar simulator.

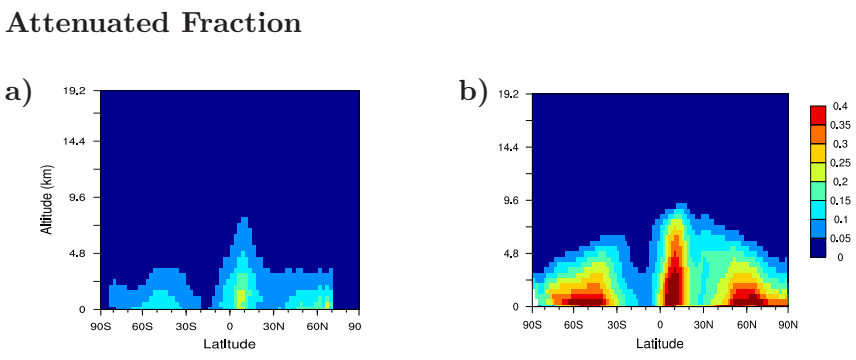

Figure 4.3— Frequency of occurrence of attenuation for JJA 2007. (a) GOCCP CALIPSO retrievals (b) ECHAM5 with CALIPSO simulator.

A comparison with the original ECHAM5 output shows that the highest-levels of stratospheric and Tropical clouds produced by the model remain undetected when processed by the lidar simulator (Fig. 4.2a,b). It is possible that when ECHAM5 models low values of

in-cloud liquid and ice water, the lidar scattering ratio remains below the threshold used to define clouds (see Chp.3.2.1).

4.2.2 Zonal Hydrometeor Fraction: Radar derived

As with the CALIPSO retrievals, the zonal hydrometeor fraction from CloudSat retrievals show a clear indication of the ITCZ and cloud-free subsiding branches of the Hadley cell (Fig. 4.2d). It is evident from the comparison of Fig. 4.2a and Fig. 4.2d that the cloud radar is able to detect a greater fraction of hydrometeors than the lidar at lower altitudes. This is because radar signals do not attenuate as easily as lidars; though they may still be attenuated by large water droplets and precipitation. It should be noted that the lowest 1.2 km of the CloudSat retrievals should not be used due to ground clutter.

The radar simulator shows that ECHAM5 captures the large-scale features including the ITCZ and subsidence branches within the Hadley cell. In addition, ECHAM5 is able to capture the spatial locations of these maxima which include those in the Southern Hemisphere, the ITCZ and boundary layer (Fig. 4.2e). The hydrometeor fraction in ECHAM5, however, is overestimated throughout compared to satellite retrievals (Fig. 4.2d). In order to judge whether this overestimation in hydrometeors is due to clouds or precipitation, or a combination of both, a distinction between their contributions to the hydrometeor fraction must first be made. Comparison of Fig. 4.2e and Fig. 4.2c show that most of the hydrometeor fraction in the ITCZ below 4 km is due to the precipitation modelled in ECHAM5 as there are few clouds modelled in that region that are visible to a radar. In areas where clouds and precipitation coexist, their respective contribution to the hydrometeor fraction is not easily distinguished as radar reflectivities are dominated by the largest particles and thereby can not distinguish between cloud ice/water and precipitating ice/water. A sensitivity experiment, for the same time period, was performed in which the convective and large-scale precipitation were refrained from entering the lidar and radar simulator; thereby isolating the contribution by clouds to the lidar and radar signals. As expected the results for the simulated lidar zonal cloud fraction show negligible differences (not shown), whereas the radar simulator shows significant differences. The radar simulator no longer had radar reflectivities greater than -15 dBZe. Therefore it can be concluded that hydrometeors in ECHAM5 with radar reflectivities between -27.5 dBZe (the lower limit of radar reflectivity) and -15 dBZe (maximum reflectivity without precipitation) are predominantly clouds. The cloud fraction calculated using this definition is shown in Fig. 4.2f.

The cloud fraction derived from the radar simulator does not agree with the originally modelled cloud fraction from ECHAM5 (Fig. 4.2c) as the optically thinnest clouds, with respect to radar reflectivity, have been removed. A comparison of Fig. 4.2d and Fig. 4.2f shows the high-level cloud fraction derived from the radar simulator agrees very well with

satellite retrievals in terms of its general shape. In the Tropical and Subtropical mid and low-levels there is an evident lack of clouds in ECHAM5. This also indicates the convective and large-scale precipitation, which is the only source of radar-visible hydrometeor fraction in this region, produces an overestimate in hydrometeor fraction. The precipitation may overestimate the hydrometeor fraction throughout the atmosphere, and in particular the boundary layer.

Comparison of the satellite retrieval (Fig. 4.2d) with both the radar simulator fractions (Fig. 4.2e,f) shows the height of the uppermost hydrometeor fraction detected by the radar simulator is lower than that retrieved by satellite; despite the large fraction of high-level clouds modelled by ECHAM5. Evidently the high-level clouds are optically thin as they are detected by the lidar simulator, yet remain undetected by the radar simulator. In addition, the difference in cloud top altitude between radar- and lidar-detected clouds is much larger in ECHAM5 than in the observations. This suggests the high-level clouds in ECHAM5 are in fact too optically thin with respect to radar reflectivity. Gehlot (2010) concluded for clouds in the Tropics the convection parameterization in ECHAM5 does not allow for the detrainment at the mid-levels but rather transports an excessive amount of mass to the high-levels before it detrains. As a result, the deep convection transports up too much mass, overestimating the cirrus clouds, which take much longer to sediment and evaporate out.

4.2.3 Zonal Hydrometeor Fraction

The zonal hydrometeor fractions from both the lidar and radar simulators adduce that large scale features, such as the ITCZ and the Hadley cell circulation are modelled well in ECHAM5. The zonal lidar and radar hydrometeor fractions indicate that ECHAM5 overestimates high-level cloud cover compared to satellite retrievals. This is particularly true for optically thin clouds as there are high-level clouds modelled which even the lidar does not detect, and are not visible to the radar until much lower in the atmosphere. Neither the cloud cover maps nor the global means indicate the overestimation of high-level clouds was so significant as the comparison of lidar and radar zonal hydrometeor fractions show. Depending on the overlap scheme employed, however, this overestimation in high-level clouds may not be evident in the projected high-level cloud cover maps (as presented in Section 4.1). An overestimation in high-level clouds can cause premature attenuation of the lidar signal which limits the conclusions which can be drawn for mid and low-level clouds in ECHAM5. The zonal radar hydrometeor fraction captures both clouds and precipitation which are overestimated by ECHAM5 in comparison with satellite retrievals specifically at low and mid-levels. A sensitivity study indicates the overestimation of hydrometeor fraction in the lower (Sub)Tropical troposphere is due solely to precipitation and as such there is evidently a lack of clouds in the (Sub)Tropics.

4.3 Lidar Scattering Ratio Joint Histograms: Cloud Regimes

The lidar joint cloud altitude-scattering ratio histograms of four cloud regimes: Californian Stratocumulus, Hawaiian Trade Cumulus, North Pacific, and Tropical Western Pacific are presented in Fig. 4.4. For each cloud regime the lidar histograms of the GOCCP CALIPSO satellite retrievals and ECHAM5 with the CALIPSO simulator are plotted for June, July, August (JJA) 2007. The lidar scattering ratio histogram shows the frequency of occurrence of clouds every 480 m from 0 to 19.2 km for a specific scattering ratio interval. The two intervals of interest in this analysis are those with scattering ratios < 0.01 and scattering ratios > 5, which denote lidar attenuation and cloud detection, respectively (See Chp. 3.1.1). The frequency of occurrence has been determined by normalizing the histogram such that the frequencies for each altitude sum to one.

Ideally this analysis would be performed by delving into the lidar histogram of the CALIPSO retrievals, then comparing them to those of the lidar simulator. This, however, is not always possible as the lidar signal often becomes attenuated high in the atmosphere in ECHAM rendering a full analysis ineffective. This will become evident in the following section. As such, only the California Stratocumulus region of the lidar simulator will be thoroughly studied, whilst only the retrievals will be discussed for the other cloud regimes.

Regional Lidar Scattering Ratio Joint Histograms

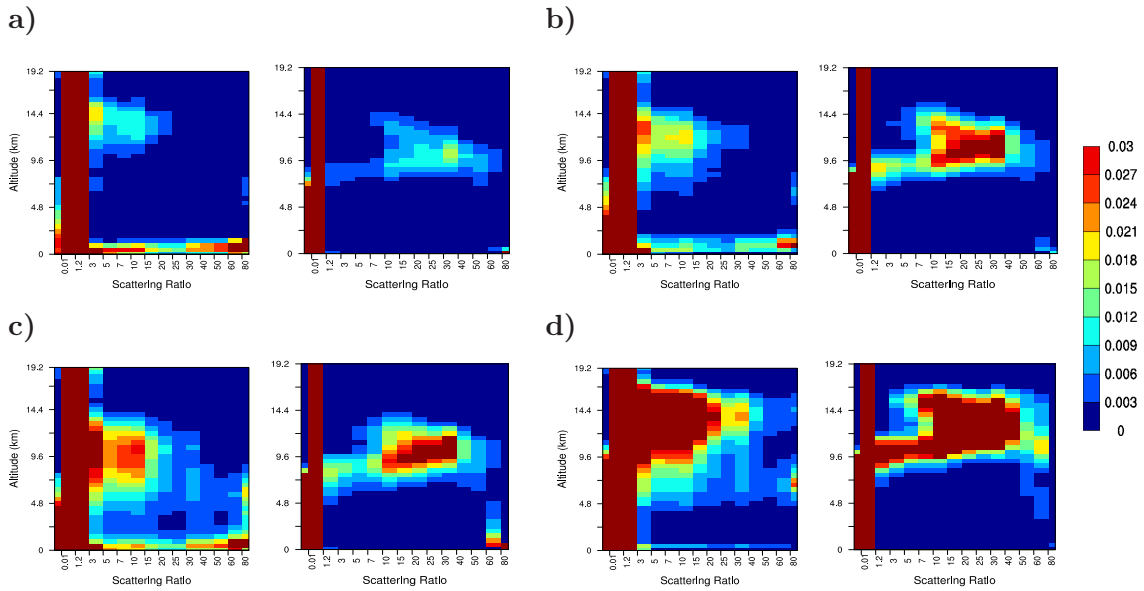

Figure 4.4— Lidar Cloud Altitude-Scattering Ratio Histogram. (a) Californian Stratocumulus: (Left) GOCCP CALIPSO Data and (Right) ECHAM5 with CALIPSO Simulator; (b) Hawaiian Trade Cumulus; (c) North Pacific; (d) Tropical West Pacific.

4.3.1 Californian Stratocumulus

The Californian stratocumulus region (Fig. 4.4a) best demonstrates the capabilities of the lidar instrument and simulator. The CALIPSO retrievals show that the greatest frequency of clouds occurs in the boundary layer. Of these boundary layer clouds, the majority have high scattering ratios (i.e. are optically thick), though they exhibit a range of scattering ratios. The low-level stratocumulus clouds are overlaid with a few high, optically thin cirrus clouds, and separated by clear mid-level atmosphere. The lidar simulator, for the most part, only detects high-level clouds in ECHAM5. These high-level clouds have much larger scattering ratios than those retrieved. For example, the maximum scattering ratio of high-level clouds in CALIPSO is 25 whereas the lidar simulator has a maximum scattering ratio of 60. Since the scattering ratio is a function of the particle size distribution and thus particle radius (Chp. 3.2.1) it important to ensure whether the effective radius of liquid water droplets and ice crystals are realistic. This is because for a given cloud water content, smaller particles have larger scattering cross-sections. Artificially small particles would indeed cause high scattering ratios and cause the lidar signal to attenuate high in the atmosphere, as is seen in Fig. 4.4a. In the ECHAM5 version employed, the particle number concentration is prescribed and as such the particle size is governed by the liquid and ice water content. The JJA 2007 global average of ECHAM5's liquid water droplet effective radius ranges from $\sim$ 4 to 5.5 μm and ice crystal effective radius ranges from $\sim$ 10 to 14.5 μm. This compares to measurements from both continental and marine stratocumulus clouds with liquid water particles with effective radii ranging from $\sim$ 4 to 12 μm (Frisch et al., 2002) and $\sim$20 to 100 μm for ice (Wyser, 1998). The effective radii of liquid particles in ECHAM5 are within the measured range, though leaning towards the lower end. The effective radii of ice particles in ECHAM5 are much lower than those measured. A sensitivity experiment will be presented in the following section in which the impact of assumed ice crystal effective radii will be studied (Sec. 4.4).

In addition to the effective radius assumed for liquid and ice particles, the lidar scattering ratio is also influenced by the cloud liquid and ice water content. The greater the liquid and ice water content within a cloud, the greater its optical thickness which governs the depth in which the lidar can penetrate. Currently, the lidar signal attenuates much more frequently high in the atmosphere ($\sim$ 7 km) as opposed to retrievals which rarely fully attenuate until $\sim$2 km. Fig. 4.1 and Fig. 4.2 show that the high-level clouds in ECHAM5 are sometimes overestimated implying an excessive amount of cloud ice. A second sensitivity experiment will be presented in which the cloud ice content of high-level clouds is reduced and the impact of the optical thickness of high-level clouds on the lidar attenuation will be studied (Sec. 4.4). It should be noted that within the ECHAM5 model, the cloud liquid and ice water are multiplied by an inhomogeneity factor of 0.7 and 0.8, respectively, before they are passed into the radiation scheme. The inhomogeneity factor

accounts for sub-grid variability (e.g. clouds are not rectangular boxes and as such the cloud liquid and ice water are lower in some regions). The simulators do not take into account this inhomogeneity factor. The simulators takes the liquid and ice water mixing ratio directly, accounting for sub-grid variability using a subcolumn generator (SCOPS). Thus, the clouds seen by the radiation scheme in ECHAM5 are optically thinner than those entering the satellite simulators. One must be aware that the satellite simulator explicitly determines what is implicitly taken into account in ECHAM5; and it is hard to say that they are equal. In the future, it would be important to make this consistent and determine the difference between assuming subcolumn liquid and ice water content of a grid box compared to the inhomogeneity factor.

The high-level clouds with large scattering ratios in the lidar histogram may render existing low-level clouds undetected by the lidar simulator by causing premature attenuation. While the lidar scattering ratio histograms provide a rich source of information regarding the high-level clouds, they must be used with caution when evaluating low-level clouds until the scattering ratios of high-level clouds in ECHAM5 are improved. As a result, further analysis of the different cloud regimes using the lidar histograms is limited here to high-level clouds. As shown later in this chapter, the radar reflectivity histograms from the CloudSat simulator, are better for analyzing low-level hydrometeor properties because the radar signal does not attenuate as easily as the lidar signal (Section 4.5).

4.3.2 Hawaiian Shallow Cumulus

The CALIPSO retrievals show shallow cumulus boundary layer clouds underlying high cirrus clouds (Fig. 4.4b). The boundary layer clouds in the Hawaiian region have a large distribution of scattering ratios, though the frequency of occurrence is reduced compared to the Californian stratocumulus region. The high-level cirrus clouds in the retrievals also have a greater scattering ratio compared to the Californian cirrus in Fig. 4.4a. This increase in the cirrus scattering ratio is captured by the lidar simulator, though it is evident the scattering ratio for these clouds are significantly greater than those retrieved. Correspondingly, the lidar signal is attenuated high in the atmosphere. As a result, no conclusions can be drawn for the low-level clouds in ECHAM5 using the lidar scattering ratio histogram.

4.3.3 North Pacific

The North Pacific CALIPSO lidar scattering ratio histogram shows optically thick, frontal clouds extending vertically throughout the atmosphere, as well as optically thick low-level clouds (Fig. 4.4c) as already discussed in Chepfer et al. (2010). These clouds also show a large distribution of scattering ratios, through not so optically thick that the lidar signal becomes fully attenuated high in the atmosphere. In ECHAM5, the clouds in the North

Pacific detected by the lidar simulator have a similar scattering ratio structure as the Hawaiian clouds, though they are lower in the atmosphere. The North Pacific is also the first time a substantial part of the distribution of clouds extending to the low-levels is detected by the lidar simulator. The low-level clouds which are detected by the lidar simulator all have very high scattering ratios, implying all modelled low-level clouds appear optically very thick to the lidar. The satellite retrievals, however, show low-level clouds have a diversity of scattering ratios. As previously discussed, the scattering ratio is a function of the particle radius and size distribution. This implies ECHAM5 has either underestimated the effective radius cloud liquid water droplets or only produces optically thick low-level clouds. The latter implies the ratio of cloud water content to the cloud fraction is always overestimated. The cloud fraction for theses regions in ECHAM5 is rather low, yet the model is tuned to an approximately correct cloud radiative effect, thus there is an overestimation in the cloud water content for a given cloud cover. The sensitivity studies presented in the next section may shed more light on the causes of the large scattering ratios of low-level clouds in ECHAM5.

4.3.4 Tropical West Pacific

Deep convection, as seen in the satellite retrievals (Fig. 4.4d), has a very large amount of high-level clouds with large scattering ratios. Consequently, attenuation frequently is high in the atmosphere, ~ 9.6 km, as opposed to the ~ 4.5 km in the Hawaiian and North Pacific regions. Chepfer et al. (2010) concluded that the secondary maxima in the CALIPSO retrievals, in the mid-troposphere (5 - 9 km) were due to the large abundance of thick congestus clouds over this region and the low-level clouds (below 3 km) were associated with shallow cumulus clouds. Because of the abundance in high-level, optically thick clouds in the Tropics, the lidar scattering ratio histograms of CALIPSO and ECHAM5 have the greatest agreement. ECHAM5 continues to overestimate the scattering ratio of the high-level clouds. However, features such as height and distribution of scattering ratios agree with retrievals.

4.3.5 Lidar Scattering Ratio Histogram

A comparison of the four lidar joint cloud altitude-scattering ratio histograms of each cloud regime, demonstrates the lidar scattering ratio becomes greater at high-levels as one moves towards the equator in both retrievals and in ECHAM5. The satellite retrievals show a very distinct pattern for each cloud regime, which is not visible from the lidar simulator. The lidar simulator shows that high-level clouds which ECHAM5 simulates have a much greater scattering ratios than shown in the satellite retrievals, as well as a greater frequency of attenuation, particularly at mid-level altitudes. The high scattering ratios in ECHAM5 can be partially attributed to the overestimation of high-level clouds,

however, greater understanding is needed in regards to the large frequency of attenuation.

It is vital that the extent to which model errors limit the application of satellite simulators be understood before the lidar simulator is used to draw conclusions about low-level clouds in ECHAM5, especially where high-level clouds are abundant. Most importantly here, an abundance of high-level clouds may influence the detection of low-level clouds by attenuating the lidar signal. The regional lidar histograms produced by the lidar simulator were initially thought to be an innovative tool for analyzing boundary layer clouds in GCMs, especially in the subsidence regimes within the Tropical marine boundary layer, however, Fig. 4.4 showed otherwise. Within the current model configuration, the radar simulator will be more useful in analyzing the low-level clouds as it does not attenuate as easily as the lidar.

4.4 Sensitivity Experiments: Impact of Cloud Ice Effective Radius & Cloud Ice Content

4.4.1 Impact on Lidar Simulator

As previously mentioned two sensitivity experiments were designed to study the causes of: (i) the exceptionally large lidar scattering ratios of clouds in ECHAM5; (ii) the frequent lidar attenuation in ECHAM5; and (iii) the high altitude attenuation in ECHAM5. The first sensitivity experiments doubles the effective radius of ice particles of ECHAM5 entering the simulator. This experiment aims to decrease the scattering by particles and thereby the attenuated backscatter, as can be seen in Equations 3.6 & 3.8. The second sensitivity experiment reduces the cloud ice content by half in clouds entering the simulator with cloud tops $\geq$ 440 hPa. This experiment aims to reduce the optical thickness of high-level clouds in order to determine whether high-level clouds in ECHAM5 are indeed overestimated in terms of ice water content and to which extent they may obscure low-level clouds.

The first sensitivity experiment showed that doubling the effective radius of ice has quite a large impact on the lidar scattering ratios (Fig. 4.5a). The lidar scattering ratios of the high-level clouds are now much smaller and close to satellite retrievals (Fig. 4.4). The greatest frequency of the scattering ratios for high-level clouds occurs in the range of 7 to 20, which is much closer to the scattering ratios of 7 to 15 as seen in the satellite retrievals. The frequency of occurrence of these high-level clouds in ECHAM5 is still much greater than observed, however, if the ice crystal radius in the model simulation was increased, ice particles would sediment faster thereby reducing the amount of high-level clouds. In regards to the altitude of attenuation, the changes are very slight and there is a very little change in the frequency in which low-level clouds are detected. The low-level clouds still remain within largest scattering ratio bins.

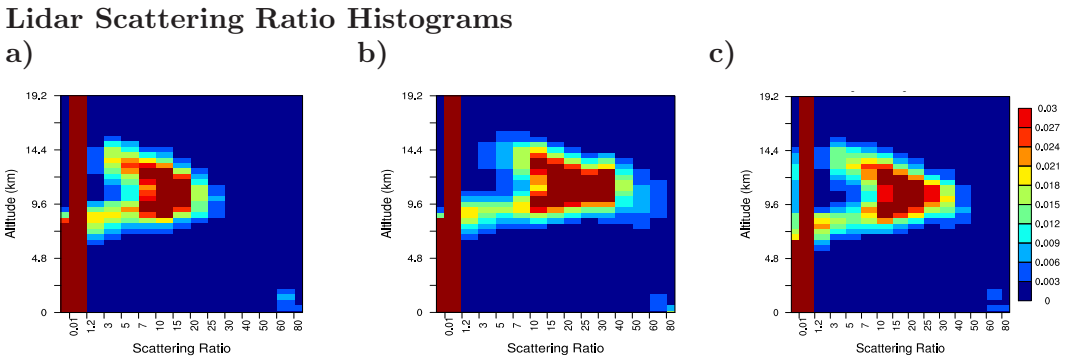

Figure 4.5— Lidar Cloud Altitude-Scattering Ratio Histogram over Hawaii for July 2007. (a) Doubling the effective radius of ice particles entering the CALIPSO Simulator; (b) Control experiment of ECHAM5 with CALIPSO Simulator; (c) Reducing the cloud ice content of clouds higher than 440 hPa entering the CALIPSO Simulator.

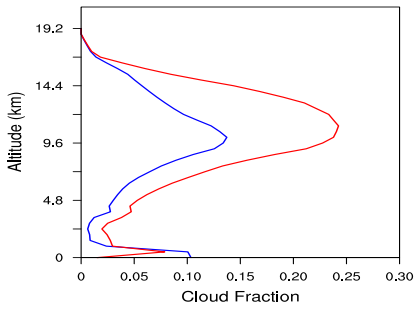

Figure 4.6— Modelled cloud fraction over the Californian and Hawaiian region for JJA 2007. (Blue) California Stratocumulus region; (Red) Hawaiian Shallow Cumulus region.

The second sensitivity experiment shows that decreasing the cloud ice content by half in clouds above 440 hPa has a much smaller affect than doubling the effective radius of ice particles. The lidar scattering ratio of high-level clouds improves slightly, however, remain much larger than those determined by the satellite retrievals. The greatest impact of decreasing the optical thickness of high-level clouds affects the altitude of attenuation. Though the frequency of attenuation at high altitudes increased, the frequency in which the lidar is able to penetrate further into the atmosphere improved. Low-level clouds still have a low frequency of occurrence and they all remain optically thick. From the vertical profile of cloud fraction over the Californian and Hawaiian region for JJA 2007 it can be seen that the greatest amount of cloud occurs in the higher altitudes and that that the low-level cloud fraction is very small (Fig. 4.6). It is possible these modelled clouds are indeed only optically thick. This would imply: (i) the liquid water effective ice radius is underestimated like the ice particles; or (ii) ECHAM5 underestimates the grid-box cloud fraction in respect to the cloud water content; or vice versa (iii) the cloud water content is overestimated for a given grid-box cloud fraction. The modelled liquid water particle radii in ECHAM5 did not differ very much from the measurements, however, they did tend to

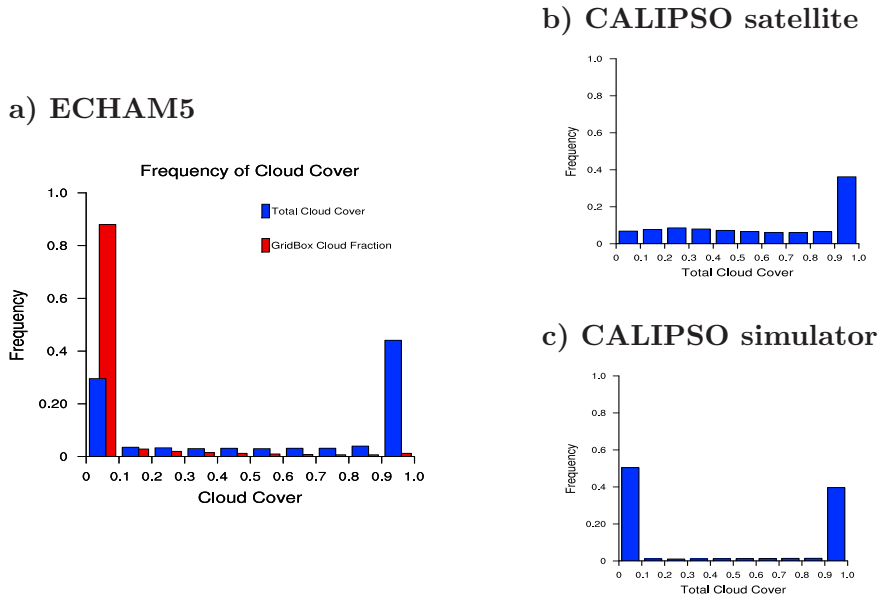

Figure 4.7— Frequency of modelled cloud fraction from 45N to 45S for JJA 2007. (a) ECHAM5 model: (Red) Frequency of cloud cover for low-level (z < 3.5 km) grid-boxes; (Blue) Frequency of total cloud cover over a column. (b) CALIPSO satellite and (c) ECHAM5 with CALIPSO simulator.

be near the lower end. The frequency of cloud fraction in ECHAM5 for the Subtropics, composed from 3 hourly instantaneous values over JJA 2007, is presented in Fig. 4.7. The frequency of occurrence for both the total cloud cover over a column and the grid-box cloud fraction of the low-level clouds (i.e. < 3.5 km) is presented. The frequency of occurance includes clearsky (i.e cloud fraction $= 0$) values. The grid-box cloud fraction refers to the resolved cloud fraction of the model layers below 3.5 km and the total cloud cover of a column is the projected 2-D cloud cover of all the 31 vertical levels. The total cloud cover over a column appears to be a bi-modal. The total cloud cover in ECHAM5 is frequently within one of the two intervals of 0 to 0.1 or 0.9 to 1 and rarely in between. In regards to the individual grid-boxes of the low-level clouds, the greatest frequency of cloud fractions are in the 0 to 0.1 interval. These low cloud fractions in the low-level grid-boxes may be the cause of the large optical thickness. Compared to the CALIPSO satellite retrievals, which show a uni-modal distribution of total cloud cover skewed towards cloud covers between 0.9 and 1.0 (Fig. 4.7), ECHAM5 vastly overestimates the frequency of occurance of low cloud fractions. It would be interesting for future work to study whether the liquid water effective radii are underestimated in ECHAM5; and whether the ratio of cloud water to cloud fraction is correct.

Despite these changes to the ice crystal effective radius and high-level cloud ice content, neither the high, mid, and low-level cloud cover maps, nor the lidar derived zonal cloud fraction change substantially (not shown). This is because whilst the scattering ratios shifted from the very high (SR > 50) values to the mid-range values (SR ~ 15), yet the

changes in scattering ratios mostly remained above the cloud threshold (i.e. SR $>$ 5). Hence the lidar derived fraction of clouds remains the same.

4.4.2 Impact on Radar Simulator

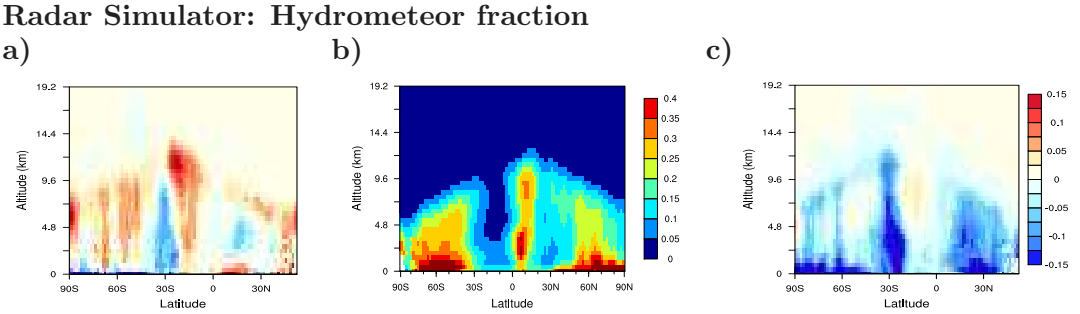

Figure 4.8— Zonal hydrometeor fraction from CloudSat simulator for July 2007. (a) Difference of experiment with doubled cloud ice effective radius, within the CloudSat simulator, to the control experiment; (b) Control experiment ECHAM5 with CloudSat Simulator; (c) Difference of experiment with high-level cloud ice content reduced by half, within the CloudSat simulator, to the control experiment.

Doubling the effective radius of ice particles also improved the problem encountered regarding the zonal hydrometeor fraction derived from the radar simulator. Previously produced high-level clouds by ECHAM5 were not detected by the radar simulator, despite being abundant; which underestimated their altitude compared to the satellite retrievals (Fig. 4.8). By doubling the effective radius of ice crystals the high-level clouds have larger reflectivities and are now detected by the radar simulator and comparable to the satellite retrievals. The second sensitivity experiment which reduced the optical thickness of high-level clouds reduced the hydrometeor fraction derived from the radar.

4.4.3 Sensitivity Experiments Summary

Doubling the effective radius of ice particles has a significant impact on the lidar scattering ratio histograms. The lidar histograms produced by the sensitivity study are now more similar to those derived from the satellite retrievals in terms of the scattering ratio range and the effective radius of ice is closer to measured ranges. In addition to improving the lidar scatter ratios, doubling the effective ice radius improved the radar hydrometeor fraction. High-level clouds previously undetected are now captured and the altitude of the highest-level clouds is closer to the satellite retrieved range.

Reducing the ice content of high-level clouds improved the frequency of attenuation of mid-level clouds, allowing the lidar to penetrate further into the atmosphere more often. The frequency of attenuation, however, remains high compared to the satellite retrievals.

Neither sensitivity experiment improved the detection of low-level clouds significantly. Those which are detected remain optically thick. The few clouds which do exist at the lower levels (i.e. less than 0.1 cloud fraction) are optically too thick within the model. In order to derive a distribution of lidar scattering ratios for low-level clouds, either: (i) the low-level cloud fraction must be increased in respect to the cloud water content; or (ii) the effective radius of liquid water particles must be increased. In the future, the latter will be tested.

4.5 Radar Reflectivity Joint Histograms: Cloud Regimes

In the following section, the radar joint cloud altitude-reflectivity histograms of the four aforementioned cloud regimes will be analyzed for JJA 2007 (Fig. 4.9). As with the lidar scattering ratio histograms, the radar reflectivity histograms of CloudSat retrievals and ECHAM5 with the CloudSat Simulator are compared. The radar reflectivity histograms show the frequency of occurrence of clouds every 480 m from 0 to 19.2 km for a specific reflectivity interval (from -30 dBZe to 20 dBZe). The histograms are normalized such that the frequency of occurrence for each altitude sums to one.

Each radar reflectivity histogram can be divided into four regions of interest: precipitating and non-precipitating, liquid water and ice hydrometeors. These four regions can be roughly divided by altitude and radar reflectivity. Above 5 km are predominantly ice hydrometeors and below are mainly liquid hydrometeors following Marchand et al. (2009). As discussed in Sec. 4.2, radar reflectivities $<$ -15 dBZe indicate non-precipitating hydrometeors, while $\geq$ -15 dBZe indicate precipitating hydrometeors. Hydrometeors, following Bodas-Salcedo et al. (2008) and Marchand et al. (2009), are characterized as particles with a radar reflectivity $>$ -27.5 dBZe. As such, Marchand et al. (2009) states that CloudSat is not sensitive to much of the non-drizzling boundary layer clouds predicted by the model, though precipitation is indicative of the presence of clouds. Below this threshold, the likelihood of false detection increases as the limits of radar sensitivity are approached (Marchand et al., 2008). Keeping in mind radar reflectivity is most sensitive to the largest particles, rain and drizzle with diameters on the order of $\sim$ 2 mm will dominate the signal despite the presence of more numerous smaller cloud droplets ($\sim$ 0.02 mm in diameter). As such, while the radar reflectivity may be within the precipitating region of the histogram, non-precipitating clouds may exist.

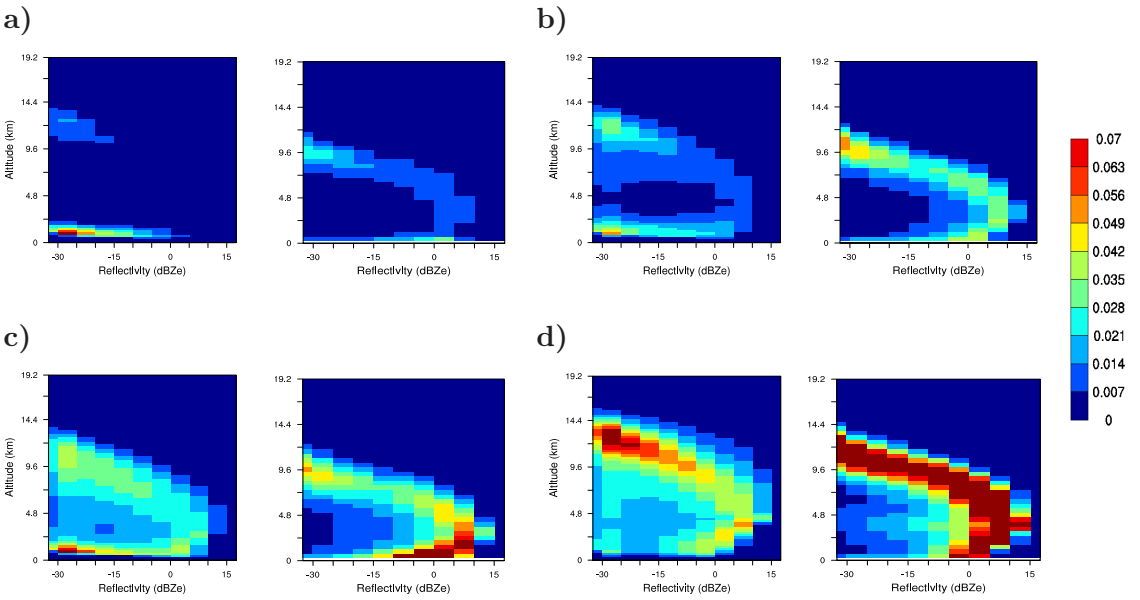

Figure 4.9— Radar Cloud Altitude-Reflectivity Histogram for JJA 2007. (a) Californian Stratocumulus: (Left) CloudSat Satellite and (Right) ECHAM5 with CloudSat Simulator; (b) Hawaiian Trade Cumulus; (c) North Pacific; (d) Tropical West Pacific.

Table 4.2— Simulated regional large-scale and convective precipitation [mm day $^{-1}$] for JJA 2007.

	Californian Stratocumulus	Hawaiian Shallow Cumulus	North Pacific	Tropical West Pacific
Convective	0.64	1.43	0.32	9.10
Large-scale	0.41	0.83	3.02	2.77

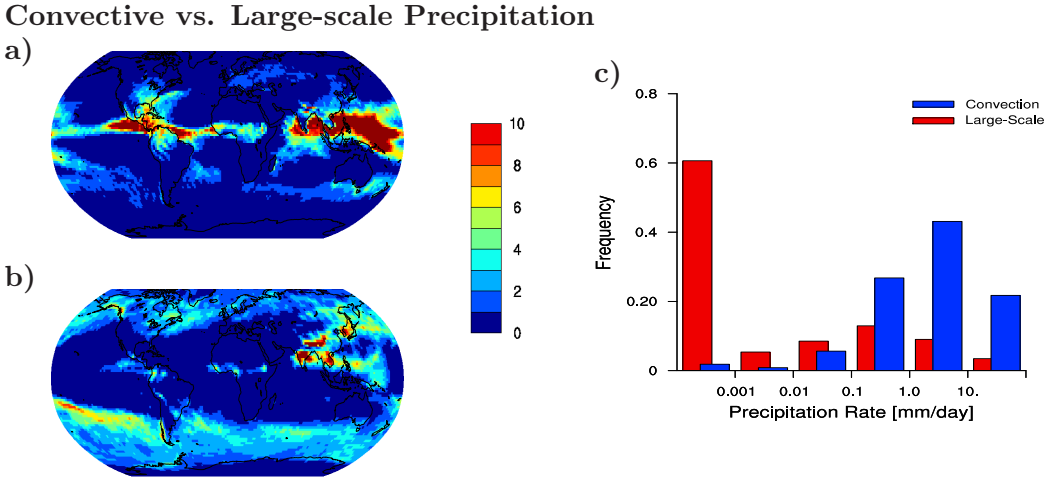

Figure 4.10— ECHAM5 modelled precipitation [mm day $^{-1}$] for JJA 2007: (a) Convective; (b) Large-scale; and (c) Relative frequency of occurrence precipitation rates for large-scale and convective precipitation in ECHAM5 from 45N to 45S.

4.5.1 Californian Stratocumulus

In the Californian stratocumulus cloud regime, the CloudSat retrievals show a clear separation between high-level cirrus and low-level stratocumulus clouds (Fig. 4.9a). The greatest frequency of occurrence of hydrometeors occur within the non-precipitating boundary layer. Comparing the radar histograms of CloudSat retrievals with the CloudSat simulator shows that ECHAM5 captures the bi-modal peak in high and low-level hydrometeors. Unlike the retrievals, however, the high-level clouds are both lower in the atmosphere and precipitate. The simulator detects hydrometeor reflectivities in the mid-levels, which are precipitating hydrometeors. Precipitation in ECHAM5 is separated into two forms: convective or large-scale precipitation. Fig. 4.10 shows the global distribution of convective and large-scale precipitation in addition to their relative frequency of occurrence over the Subtropics and Tropics. Table 4.2 presents the regional contribution of convective and large-scale precipitation rates. Though convective precipitation dominates the surface precipitation rate, the extent to which its frequency contributes to the radar reflectivity histogram is uncertain. A sensitivity experiment presented in following section isolates the contribution of convective precipitation to the radar reflectivity histograms. The results show that the reflectivities at the mid-level are mainly caused by the large-scale precipitation rather than convective precipitation. Within ECHAM5, the high and mid-level large-scale precipitation formed via the ice phase is the result of the sedimenting ice crystals, accretion or aggregation process. As previously mentioned, the moisture available to these processes stems, to a large extent, from the convective mass flux which transports moisture to the upper atmosphere. It is possible that an excessive amount of moisture brought up to the upper atmosphere was transported horizontally to cover the Hawaiian and Californian regions before sedimenting out.

The Californian radar reflectivity histogram shows that throughout the atmospheric column all the simulated radar reflectivities are greater than retrieved. The greatest frequency of occurrence is simulated for hydrometers that are precipitating as they have high radar reflectivities. Hagemann et al. (2006) showed that the zonal and global distribution pattern in ECHAM5 agrees well with the Climate Prediction Center Merged Analysis of Precipitation global annual mean precipitation climatologies from the 1979 to 1999 (Xie & Arkin, 1997). Thus, it can be concluded that the frequency of precipitation is too high but is balanced by an intensity of precipitation which is too low. This conclusion is consistent with the results of Fig. 4.10c. In other words, ECHAM5 precipitates too frequently and the total convective precipitation is underestimated. This supports the findings of Dai (2006) which states that GCMs, including ECHAM5, generally underestimate the contribution and frequency of heavy (> 20 mm day^{-1}) precipitation and overestimate light (< 10 mm day^{-1}) precipitation. This feature was also seen in the Multiscale Modeling Framework (MMF) model using the CloudSat simulator, although only

in the North Pacific region (Marchand et al., 2009).

4.5.2 Hawaiian Shallow Cumulus

Similar to the Californian stratocumulus radar reflectivity histogram, the Hawaiian shallow cumulus CloudSat radar histogram shows a bimodal peak in cloud frequency. There is a maximum in the region of non-precipitating boundary layer clouds and a second in the high-level non-precipitating clouds (Fig. 4.9b). The separation of high cirrus over the shallow cumulus is not as distinct as the stratocumulus cloud regime. The non-precipitating shallow cumulus clouds are deeper and have reflectivities higher in the atmosphere, as well as show a greater diversity in reflectivities. For the retrieved boundary layer clouds there is also a greater frequency of clouds with high reflectivities compared to the Californian stratocumulus region, indicative of more precipitation. The comparison with the model results shows that ECHAM5 captures the general radar reflectivity structure, though lower in the atmosphere. The hydrometeors in ECHAM5, however, are too reflective at all altitudes, particularly in the mid and low-levels. As discussed in the Californian stratocumulus regime, the high radar reflectivities are likely due to the overestimate in precipitation frequency and the associated large hydrometeors size. Although precipitation dominates the mid and low-levels radar reflectivities, the radar remains unattenuated in this region, and it can be seen that there are too few non-precipitating low-level clouds simulated in ECHAM5.

4.5.3 North Pacific

In the North Pacific, frontal clouds are evident in the CloudSat retrievals, with optically thick clouds occurring through out the atmospheric column (Fig. 4.9c). The retrievals show that the greatest frequency of clouds remains in the non-precipitating boundary layer, while conversely ECHAM5 shows the greatest frequency of occurrence in the precipitating region. Compared to the Californian and Hawaiian regions, both the satellite retrievals and ECHAM5 show a greater frequency of precipitation, though the frequency of precipitation in ECHAM5 is greatly overestimated. It is evident from these radar histograms that the precipitation intensity within ECHAM5 must be increased, thereby reducing the frequency of precipitation while maintaining the accumulated precipitation. The CloudSat simulator detects few mid-level non-precipitating clouds, which the satellite retrievals show an abundance of. Once again the high-level clouds detected by the simulator are lower in the atmosphere than those seen in the retrievals.

4.5.4 Tropical West Pacific

Unlike the other three cloud regimes, the CloudSat retrievals show that the clouds in the Tropical West Pacific have a maximum of upper-level non-precipitating ice clouds (Fig. 4.9d). In addition, there is a greater distribution of hydrometeors over all reflectivities and all altitudes compared to the other three cloud regimes. Similarly, ECHAM5 with the radar simulator shows a distribution of hydrometeors over all altitudes, however, the precipitating hydrometeors dominate the radar reflectivity. The radar reflectivities from the radar simulator above 0 dBZe is indicative of rainfall mainly from convection (Table 4.2). This value is based on the ground based observations of Tropical convective precipitation used in Mather et al. (2007). Attenuation by rainfall explains the decrease in reflectivity below the freezing level, which lies at $\sim$ 5 km in the Tropics (Bodas-Salcedo et al., 2008). In this Tropical cloud regime, the simulated reflectivities are too great at all levels. This may be related to an overactive convection as proposed by Marchand et al. (2009) and the excessive mass flux transport to higher-levels by the convective scheme described in Chp. 2.3. It should be reiterated that the high-level clouds appear much lower in the atmosphere compared to the satellite retrievals with the current setting of ice crystal effective radius.

4.5.5 Radar Reflectivity Histogram

In summary, this study of the radar joint cloud altitude-reflectivity joint histograms for the four regional cloud regimes demonstrates ECHAM5 captures the general radar reflectivity structure well. ECHAM5, however, has much a greater frequency of precipitation compared to the satellite retrievals. In all regions examined here, except the Tropics, the greatest frequency of occurrence of hydrometeors from satellite retrievals is within the non-precipitating boundary layer. This, however, is not what is modelled. Aside from the highest levels ($>$ 9 km), the greatest frequency of occurrence of hydrometeors in ECHAM5 is generally within the precipitating half of the histogram, be it ice or liquid water. As the radar reflectivities are dominated by precipitating hydrometeors, especially in the lower-levels, conclusions about the non-precipitating low-level clouds must be treated with caution until the problem regarding the frequency precipitation is fixed.

Lastly, the CloudSat simulator also shows that clouds in ECHAM5 are consistently lower than those in the retrievals. As the zonal plots in Fig. 4.2 show that clouds are indeed being produced high in the atmosphere, it is evident these clouds are not being detected by the radar simulator. Sensitivity experiments showed that this is partly due to an underestimation of cloud ice crystal effective radii, although other influences may include a lack of cloud water content.

4.6 Radar Reflectivity Joint Histograms: Contribution by Precipitation

As mentioned in Sec. 4.2, a sensitivity test was performed in which precipitation was withheld from the COSP lidar and radar simulators. The radar joint cloud altitude-reflectivity histograms for the Californian stratocumulus and Hawaiian shallow cumulus regions of this experiment are shown in Fig. 4.11. The most significant feature of these radar reflectivity histograms is the absence of radar reflectivities $\geq$ -15 dBZe. This implies cloud reflectivities never exceed -15 dBZe in ECHAM5. This is partly due to an assumption regarding the maximum effective radius for cloud particles defined in the micro-physical scheme of ECHAM5. This result allowed for a zonal *'cloud fraction'* from radar reflectivities to be defined in Sec. 4.2. In a similar experiment, Marchand et al. (2009) found a maximum reflectivity of -20 dBZe for clouds in the MMF model; the differences being likely the result of micro-physical assumptions within the two models.

Elimination of the large precipitating particles allows the clouds previously obscured to the radar simulator due to their smaller particles to become evident. Not only are the clouds now detected, the radar clearly shows an abundance of high and mid-level clouds, though it should be noted each altitude is normalized to one. This, however, is most peculiar as the Californian and Hawaiian regions were selected to be representative of cloud regimes in which relatively few high-level clouds and an abundant amount of low-level clouds exists. ECHAM5 evidently overestimates the frequency of occurrence of high-level clouds in these regions. As previously mentioned, the over abundance of high-level clouds is partly associated with the overestimation of cloud base mass-flux in the Tiedtke scheme (Neggers et al., 2004), although there could be other reasons including too little evaporation.

The histograms in Fig. 4.11 show that very few low-level clouds are detected despite the selection of two regions which should have a large fraction of low-level clouds. Further study regarding whether the low-level clouds shown in Fig. 4.6 have low radar reflectivities, or if excessive high-level clouds attenuate the radar signal would be interesting. Additionally, determining whether the high frequency of low-intensity precipitation is the cause of ECHAM5 underestimate of non-precipitating boundary layer clouds would be valuable.

The plots in Fig. 4.11 additionally provide information regarding precipitation in ECHAM5. Take for example the Californian stratocumulus region where there is precipitation at high-levels. Precipitation in these regions, as previously discussed, is either large-scale or convective precipitation. The Californian stratocumulus region was defined according to geographical region, so whether the precipitation reflectivities come from large-scale or convective events passing through the region is uncertain. A sensitivity

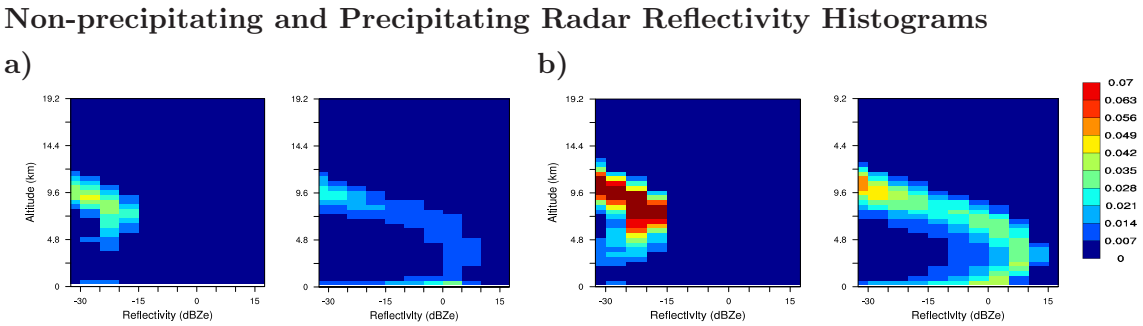

Figure 4.11— Radar Cloud Altitude-Reflectivity Histogram for JJA 2007. (a) Californian Stratocumulus: (Left) without precipitation (Right) with precipitation; (b) Hawaiian Trade Cumulus.

experiment was performed in which the contribution of convective precipitation was eliminated from the lidar and radar simulator. The results show that convective precipitation contributes to the radar reflectivity histogram mainly in two regions (Fig. 4.12): the high-level, low reflectivity region, and the mid- to low-level regions of high-reflectivity. The convective contribution, however, to the regions above 3.5 km with reflectivities >-15 dBZe are minimal, so there the large-scale precipitation is dominant.

Simply sampling over a geographical region region, may be reflecting locational biases in different clouds regimes and as such the results may be misleading. This leads to desire for sampling by large-scale environment, which is done in the next section. It aims to determine whether the sampling is causing large amount of high level clouds and precipitation.

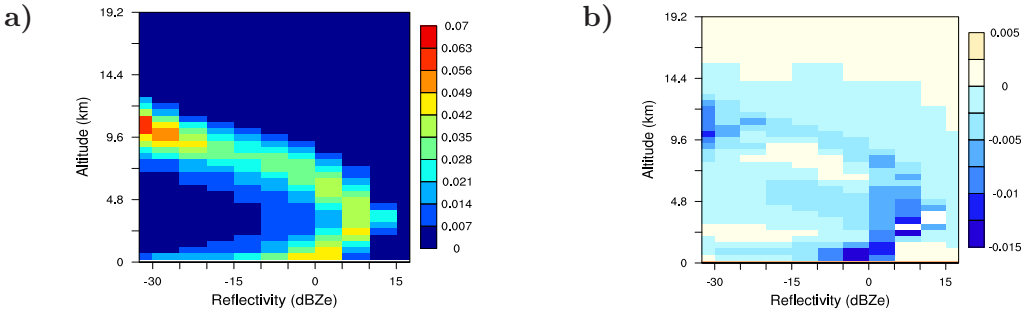

Figure 4.12— (a) Hawaiian radar cloud altitude-reflectivity histogram for July 2007; (b) Elimination of convective contribution from control run.

4.7 Radar Reflectivity Joint Histograms: Dynamical Regimes

This section delves further into the radar joint cloud altitude-reflectivity histograms of the stratocumulus and shallow cumulus cloud regimes. Previously these cloud regimes were defined by geographical area (Chp. 4.5). In this section, the stratocumulus and shallow cumulus cloud regimes are defined by large-scale environmental dynamics. Stratocumulus and shallow cumulus clouds are classified according to the large-scale vertical velocity (ω), at 500 hPa and 700 hPa, and the lower tropospheric stability (LTS $\equiv \theta_{700hPa} - \theta_{sfc}$) (Klein & Hartmann, 1993; Bony et al., 2004; Medeiros & Stevens, 2009). The vertical velocities are first used to identify regions of large-scale subsiding motion, which are indicative low-cloud regimes. These regions are then separated into stratocumulus and shallow cumulus cloud regimes using the LTS. Regions of strong subsidence are defined as areas where $\omega_{500hPa} \geq 10$ hPa day^{-1} and $\omega_{700hPa} \geq 10$ hPa day^{-1} and LTS ≥ 18.55 K indicates stratocumulus while LTS < 18.55 K defines shallow cumulus (Medeiros & Stevens, 2009). For the satellite retrievals, the monthly mean of vertical velocity and potential temperature (θ) from the European Centre for Medium-Range Weather Forecasts reanalysis data set (ERA-Interim) are used. The ERA-Interim stratocumulus and shallow cumulus dynamical cloud masks for JJA 2007 are presented in Fig. 4.13 alongside the ECHAM5 mask. The radar reflectivities from within these regions were used to create the radar reflectivity histograms presented in Fig. 4.7.

The dynamical cloud masks of both stratocumulus and shallow cumulus for ERA Interim and ECHAM5 are rather similar in their geographical distributions, although ECHAM5 underestimates the extent of subsidence regions, particularly stable shallow cumulus. Despite the similar dynamical cloud masks, the resulting radar reflectivity histograms are very different (Fig. 4.14). Not only are the dynamical radar histograms for satellite retrievals and ECHAM5 different from one another, they are vastly different compared to the regional radar histograms previously presented. The radar reflectivity histograms of the dynamical stratocumulus (Fig. 4.7b) and shallow cumulus (Fig. 4.7f) clouds are much more reflective than the regional histograms of the satellite retrievals (Fig. 4.5). In addition, the distinction between the high-level cirrus and low-level boundary layer clouds is no longer pronounced. Evidently, some regions of stratocumulus and shallow cumulus have more mid-level cloud; which makes it difficult to distinguish between the two cloud regimes. It can be concluded that sampling solely according to dynamical conditions is insufficient for satellite retrievals. The dynamical stratocumulus and shallow cumulus clouds of the retrievals were further sub-sampled for the same geographical area, over to the Californian and Hawaiian as previously described, to compare with the regional radar reflectivity histograms. These are plots are presented in Fig. 4.7a and Fig. 4.7d. It can be concluded from the series of plots that not all stratocumulus and shallow cumulus

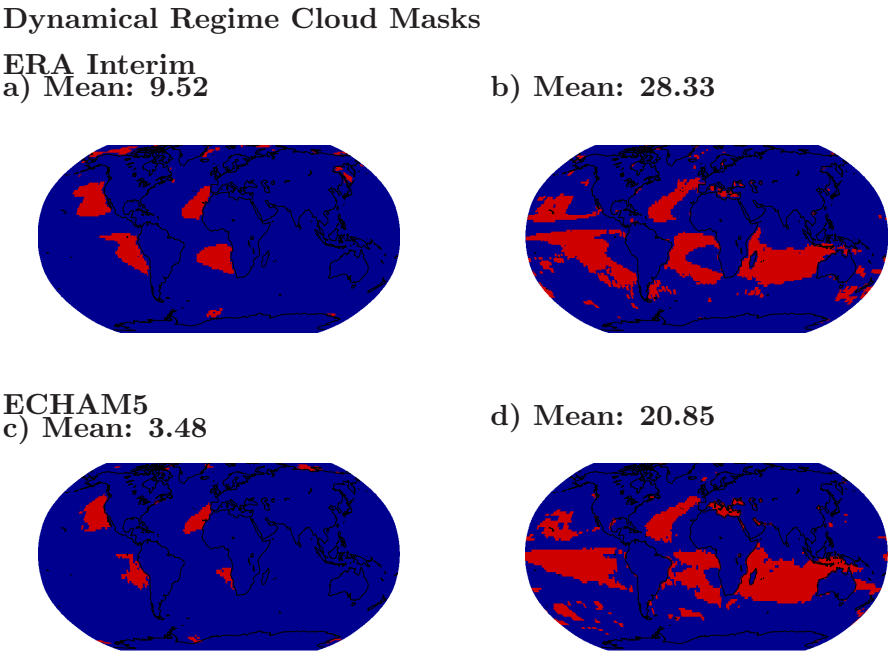

Figure 4.13— Dynamical Cloud Mask for JJA 2007. Top row: ERA interim (a) Stratocumulus; (b) Shallow Cumulus. Bottom row: ECHAM5 (c) Stratocumulus; (d) Shallow Cumulus. Values indicate the fraction of the globe covered by the regimes.

regions, when defined dynamically according to Medeiros & Stevens (2009), have the same reflectivities signature despite having the same large-scale environmental properties.

The radar joint cloud altitude-reflectivity histograms of ECHAM5, when sampled according to dynamical regimes, have very different structures compared to both the satellite retrievals and regional subsets. The radar reflectivities of the dynamical regimes in ECHAM5 have more mid-level clouds with varying reflectivities; as seen in the satellite retrievals. Both the satellite retrievals and ECHAM5 show that not all subsidence regions have the same properties since the structure of the mean radar reflectivities are vastly different compared to the Californian and Hawaiian subsets. The radar reflectivity histograms of the Californian and Hawaiian subsets of the dynamically sampled subsidence regions in ECHAM5 are much closer to the satellite retrievals compared to the simple geographically sampled region. In fact using the dynamical mask, then sampling over area is a better way of identifying cloud regime properties in the model.

4.8 Conclusions

With the advent of space-borne active instruments, a richer data set has become available for the evaluation of global models. As stated in Solomon et al. (2007), "The better a model simulates the complex spatial patterns and seasonal and diurnal cycles of present

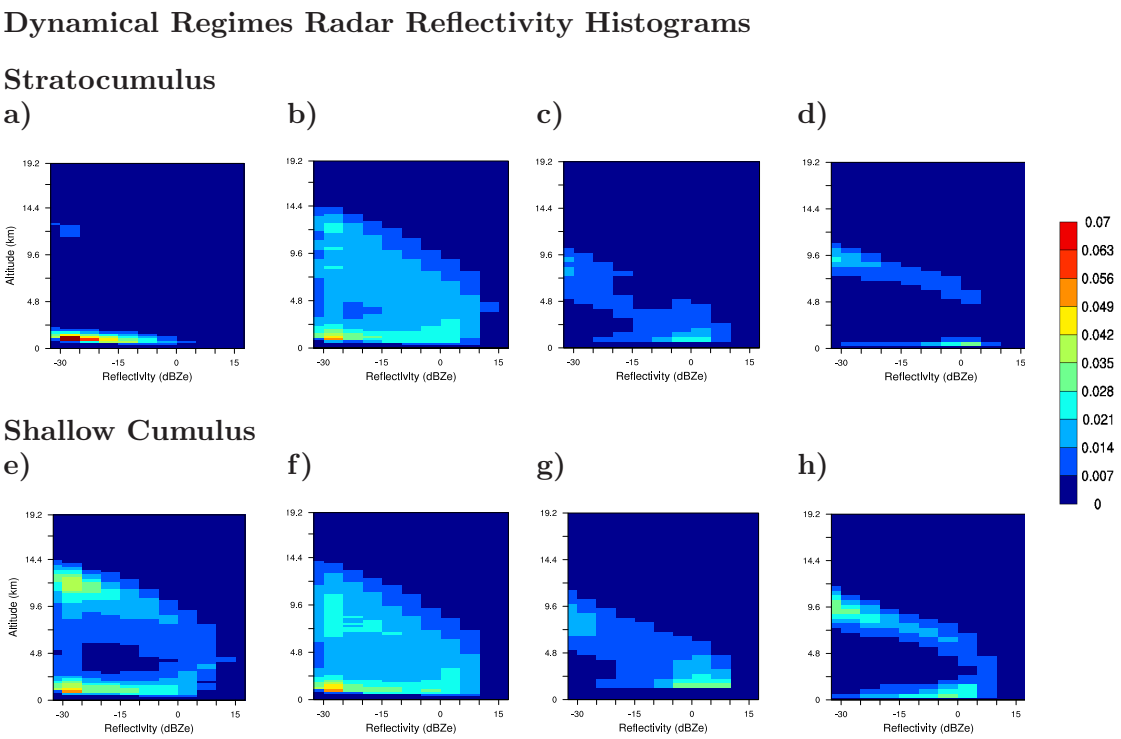

Figure 4.14— Radar Cloud Altitude-Reflectivity Histogram from Dynamical Regimes for JJA 2007. Top: Stratocumulus (a) Californian subset of CloudSat dynamical stratocumulus, (b) CloudSat dynamical stratocumulus, (c) ECHAM5 dynamical stratocumulus, (d) Californian subset of ECHAM5 dynamical stratocumulus. Bottom: Shallow Cumulus. (e) Hawaiian subset of CloudSat dynamical shallow cumulus, (f) CloudSat dynamical shallow cumulus, (g) ECHAM5 dynamical shallow cumulus, (h) Hawaiian subset of ECHAM5 dynamical shallow cumulus.

climate, the more confidence there is that all the important processes have been adequately represented", and so we endeavor to evaluate ECHAM5's ability to simulate the present climate by comparing it to CALIPSO and CloudSat satellite retrievals.

In order to compare ECHAM5 with the satellite retrievals, it was necessary to incorporate the lidar and radar satellite simulators. While using these simulators in the study of low-level (Sub)Tropical clouds modelled in ECHAM5, it was essential that we both demonstrate the tools at hand and understand their limitations.

In the process of studying the low-level clouds in ECHAM5 we learned that ECHAM5 captures large-scale features such as the projected distribution of total cloud cover, as well as high-level clouds and cloud characteristics associated with the Hadley circulation well. The lidar and radar simulators, however, have limited applications for evaluating low-level clouds in certain situations due to model errors. These errors include: an overestimation of high-level, optically thin clouds; an underestimation of the effective ice radius assumed in ECHAM5; and an overestimation of the precipitation frequency at low intensities.

The overestimation of high-level, optically thin clouds in ECHAM5 attenuates the lidar signal prematurely high in the atmosphere limiting the amount of clouds detected at lower

levels. Gehlot (2010) found the overestimate in high-level clouds stems from the excessive transport of mass into the upper atmosphere via convection which takes longer to evaporate and sediment out. This problem is exacerbated by the fact that the ice crystal effective radius is underestimated which leads to scattering ratios that are too large for a given ice crystal content.

The underestimation of ice crystal effective radius in ECHAM5 causes high-level clouds to have high scattering ratios, which attenuates the lidar artificially high in the atmosphere. Additionally, the underestimation of ice crystal effective radius renders the high-clouds undetectable to the radar simulator, which, compared to the observations, are too low in atmosphere. The sensitivity study proved that changing the ice crystal effective radius had a greater impact on the cloud optical thickness than dividing the cloud ice content by a factor of two.

It is vital that the precipitation scheme is improved in regards to the frequency and intensity of precipitation. The radar simulator showed that precipitation in ECHAM5, which accounts for all radar reflectivities $>$ -15 dBZe, is too frequent. Since the accumulated precipitation compares well to observations, it can be inferred that the intensity is too low. It was determined that large-scale precipitation dominates the radar joint cloud altitude-reflectivity histogram, and the contribution by convective precipitation is minor. An overestimation in the precipitation frequency also implies that there are consistently large rain or snow particles in the atmosphere which dominate the radar reflectivity, rendering non-precipitating low-level clouds undetected by the radar simulator. These two model errors limit the lidar and radar simulators when studying the non-precipitating boundary layer clouds. Despite these limitations, however, we can still conclude that the (Sub)Tropical boundary layer clouds in ECHAM5 are underestimated and too optically thick. This may imply that the effective radius of liquid water particles are underestimated; which will be studied in the future. In the future, it would also be interesting to determine whether there is a significant difference between assuming sub-column liquid and ice water content of a grid-box compared to the prescribed inhomogeneity factor.

Studying the radar reflectivity histograms also demonstrated that identifying boundary layer clouds according to the large-scale subsidence is insufficient. It was shown that even in areas of strong subsidence often higher-level clouds are captured. Only when the large-scale dynamics is used in conjunction with geographical sub-sampling is there fruitful identification low-level cloud regimes. Furthermore, the lower-tropospheric stability criterion is not sufficient to clearly separate stratocumulus and shallow cumulus clouds in the satellite retrievals.

We learned that high-level clouds and the convection scheme in ECHAM5 should be revised to produce fewer high-level clouds and that the assumed ice crystal effective radius should be doubled. In regards to the boundary layer clouds, the frequency of precipitation

must be decreased in ECHAM5 while increasing cloud cover and decreasing the cloud optical thickness.

Chapter 5

Comparing Boundary Layer Schemes

How do different representations of boundary layer clouds in the ECHAM5 GCM improve the present cloud and precipitation distributions?

As described in Chapter 4 low-level clouds in ECHAM5 are poorly represented compared to CALIPSO and CloudSat satellite retrievals; motivating the study of new parameterizations of low-level clouds. In the following chapter, three new parameterization schemes will be evaluated using the CALIPSO and CloudSat simulators and compared to the standard ECHAM5 convective mass-flux scheme (referred to as ECHAM5_Std; Tiedtke, 1989). The three new schemes include: (i) a modified version of the Tiedtke (1989) scheme in which a new convective trigger is employed (referred to as ECHAM5_Trig; Roeckner & Esch, 2010); (ii) a bulk parameterization of the effects of transient shallow cumulus clouds (referred to as ECHAM5_VSMF; Von Salzen & McFarlane, 2002; Isotta, 2010); and (iii) a Dual Mass Flux (DMF) scheme adjusted to better represent shallow convection (referred to as ECHAM5_DMF; Neggers et al., 2009). These changes are primarily to the parameterization of shallow convection.

If a scheme captures the boundary layer clouds and the transitions between different cloud types well, it indicates the vertical turbulence fluxes of heat, moisture and momentum and their relationship to cloud cover have been successfully modelled (Siebesma et al., 2003; Svensson et al., 2000; Karlsson et al., 2008). If different boundary layer regimes, which have vastly different radiative effects, are poorly reproduced by models in present-day simulations, it is unlikely these models will show much skill in reproducing cloud regime type feedbacks (Webb et al., 2001). This study will focus on the Tropics and mid-latitudes, specifically from 45 °N to 45 °S. This region is especially important as the sensitivity of marine boundary layer clouds to changing environmental conditions currently constitutes the main source of uncertainty in Tropical cloud feedbacks within GCMs (Bony & Dufresne,

2005).

5.1 Boundary Layer Scheme Descriptions

5.1.1 Convective Mass-flux with Modified Convective Trigger (Trig)

ECHAM5_Trig model includes a modified version of the convection scheme in ECHAM5_Std, more specifically in regards to the convective trigger. In the standard version of ECHAM5, convection occurs if surface air, lifted dry-adiabatically to the lifting condensation level, is found to be more buoyant than the environmental air. The buoyancy of the surface air parcel is defined as the difference in virtual temperature between the parcel and the environment. To account to some degree for sub-grid variability, a constant of 0.5 K is added to the virtual temperature of the parcel. This adjustment is referred to as the convective trigger. In the ECHAM5_Trig model the convective trigger is modified such that the constant 0.5 K is replaced with more physical value, the standard deviation of the virtual potential temperature (Roeckner & Esch, 2010). This term is calculated at the lifting condensation level in the same manner as the vertical diffusion of heat and moisture desctibed in Chp. 2.4 and then applied to all sub-cloud layers. Lower and upper thresholds of 0.025 and 1.0, respectively, have been applied to the standard deviation of virtual potential temperature. Once convection occurs, the standard Tiedtke (1989) convection scheme is employed, though the buoyancy term includes the dependency on the variance of virtual potential temperature (refer to Chapter 2.3).

5.1.2 Bulk Parameterization: Effects of transient shallow cumulus (VSMF)

The ECHAM5_VSMF model includes a change to the representation of shallow convection made by Isotta (2010). Shallow convection, previously represented by the Tiedtke (1989) scheme, is replaced by the Von Salzen & McFarlane (2002) scheme. The Von Salzen & McFarlane (2002) shallow convection scheme is a bulk parameterization of an ensemble of transient shallow cumulus clouds, which accounts for two key processes: the life cycle of shallow cumulus clouds, and inhomogeneities in the horizontal distribution of in-cloud properties. Both processes are greatly affected by the entrainment and detrainment rates, which differ over the lifetime of shallow cumulus cloud (Fig. 5.1). In developing shallow cumulus clouds, inhomogeneities in cloud properties arise from the entrainment of environmental air in narrow regions near the top of rising cumulus cloud (Kuo, 1965). When shallow cumulus clouds reach their maximum heights, rapid decay associated with lateral mixing occurs. This is approximated as an abrupt lateral detrainment of cloudy

air into the environment (Von Salzen & McFarlane, 2002). As such, entrainment and detrainment are separated into two categories: those which occur at the top of rising clouds and those which occur at the sides of clouds, below the rising top.

The shallow convection scheme in ECHAM5_VSMF begins by launching a test parcel from either the lowest three model levels or the surface, whichever has the highest moist static energy. The test parcel, representative of an ascending cloud, is lifted from the boundary layer through the level of free convection up to the level of neutral buoyancy. The ascent of the parcel is affected by entrainment and detrainment. If the pressure difference between the level of neutral buoyancy (LNB) and the level of free convection (LFC) is less than 300 hPa and if the ascent velocity is sufficiently strong to allow the test parcel to travel between two vertical levels in a timestep, shallow convection is permitted. Otherwise the clouds are classified as stratiform. The closure linking the cloud-base mass-flux with the convective vertical velocity scale, following Grant (2001), is based on a simplified turbulent kinetic energy (TKE) budget (Isotta, 2010). Should either of the following three conditions hold:(i) shallow convection does not trigger a cloud; or (ii) the level of neutral buoyancy is above the $0\,^{\circ}C$ level; or (iii) the depth of the LNB-LFC exceeds 300 hPa; then the Tiedtke (1989) scheme is employed to determine if deep or mid-level convection exists (Isotta, 2010). The work of Isotta (2010) found that the incorporation of the Von Salzen & McFarlane (2002) representation of shallow convection increased the low-level stratus and stratocumulus clouds, including the (Sub)Tropical regions.

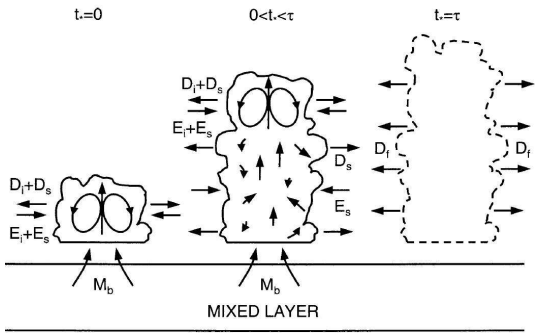

Figure 5.1— A simplified life cycle of a shallow cumulus cloud where E_i and D_i is indicative of entrainment and detrainment at the top of the cloud, E_s and D_s denotes entrainment and detrainment at the lateral boundaries and D_f is complete detrainment (Von Salzen & McFarlane, 2002).

5.1.3 Dual Mass Flux (DMF)

As shown in Chapter 2.1 the time evolution of the large-scale equations for heat and moisture can be broken up into two parts: (i) the tendency due to turbulent mixing and convection; and (ii) the tendency due to advection and diabatic processes. In the standard ECHAM5 model, the tendency due to turbulent mixing is parameterized in terms

of eddy diffusivity, while convection in parameterized in terms of the convective mass-flux (Tiedtke, 1989). In the ECHAM5_DMF model version, the turbulent mixing parameterization includes *both* eddy diffusivity and an advective mass-flux (Neggers et al., 2009) (Eq. 5.1). The eddy diffusivity term is paramerterized as a function of turbulent kinetic energy (Roeckner et al., 2003). The advective mass-flux represents organized updrafts (Siebesma et al., 2007).

$$\overline{w'\phi'}_{turb} = A^K \overline{w'\phi'}^K + A^{up} \overline{w'\phi'}^{up} \tag{5.1}$$

In the Dual Mass Flux (DMF) equation (Eq. 5.1) w is the vertical velocity, ϕ represents the total specific humidity (q_t) and liquid water potential temperature (θ_l). The superscript K denotes the turbulent mixing due to eddy diffusion and *up* denotes the turbulent mixing due to organized updrafts. A^{up} is the area fraction covered by the organized updrafts (fixed at 10 %) and the remainder $A^K = 1 - A^{up}$ is the area covered by eddy diffusion (Neggers et al., 2009). The advective mass-flux (updrafts) is broken up into two parts: dry and moist updrafts (Eq. 5.2).

$$\begin{aligned} A^{up}\overline{w'\phi'}^{up} &= M_{dry}(\phi_{dry} - \overline{\phi}) + M_{moist}(\phi_{moist} - \overline{\phi}) \\ &= a_{dry} w_{dry}(\phi_{dry} - \overline{\phi}) + a_{moist} w_{moist}(\phi_{moist} - \overline{\phi}) \end{aligned} \tag{5.2}$$

$(\phi - \overline{\phi})$ denotes the excess in ϕ of the dry and moist updraft over its environment (Neggers et al., 2009). The volumetric mass-flux (M) for dry and moist updrafts is composed of the area fractions (a) covered by the dry and moist updrafts as well as vertical velocity (w). The partitioning of the bulk advective updraft amongst dry and moist updrafts allows for a smooth transition between the representation of different boundary layer clouds (Neggers et al., 2009). By changing the ratio of a_{dry} and a_{moist}, different cloud regimes can be represented (Fig. 5.2). For example, stratocumulus clouds would have $a_{moist} = 1$ and $a_{dry} = 0$, while the converse would be true for areas of solely dry convection. Areas with fractional cloud cover, such as those covered by shallow cumulus clouds, can be represented by some flexible ratio of a_{moist} and a_{dry}. The a_{moist} term is explicitly parameterized as a function of the proximity to saturation and the stability of the transition layer between turbulent mixed layer and convective cloud layer (Neggers et al., 2009). $w_{dry,moist}$ is determined by vertically integrating the rising plume model (Siebesma et al., 2007) from an initial state (Neggers et al., 2009).

The ECHAM5_DMF also includes the formulation of vertical turbulent diffusion on conserved variables by Siegenthaler-Le Drian (2010). Previously, turbulent diffusion in ECHAM5 was done on non-conserved variables which served to smooth the vertical profile of total water, destroying the cloud. Siegenthaler-Le Drian (2010) found that turbulent

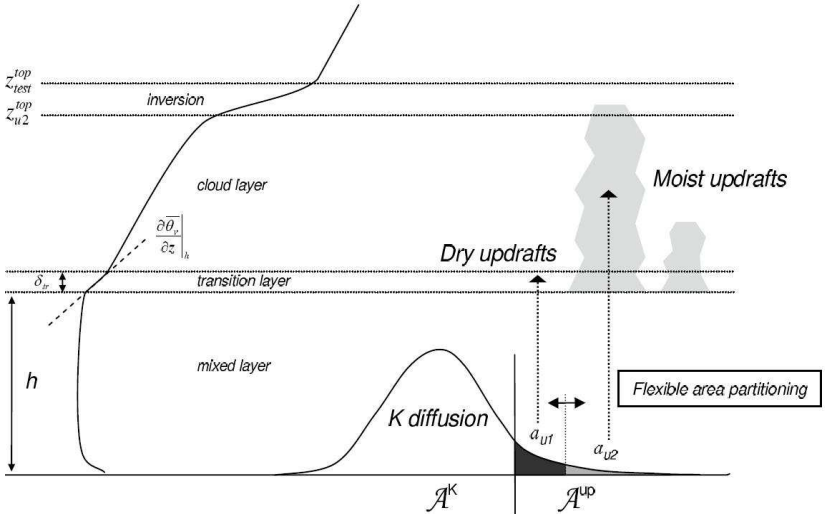

Figure 5.2— Structure of dual mass flux. $A_{up} = a_{u1} + a_{u2}$ represents advective updrafts, while A_K represents diffusive motions. The a_{u1} fraction represents dry updrafts which do not reach the lifting condensation level (dark grey), while the a_{u2} fraction represents updrafts which condense and become positively buoyant cumulus clouds (light-grey) (Neggers et al., 2009).

diffusion on conserved variables, in combination with decreasing the minimal width of the total mixing ratio PDF, increased the cloud cover.

The current implementation of the ECHAM5_DMF, at the time of manuscript submission, remains preliminary. There remain key issues in the implementation which need to be addressed, including: (i) the interaction of the boundary layer statistical cloud scheme with the radiation scheme; and (ii) improvement of surface fluxes. Currently the dissociation between clouds and radiation causes large top of the atmosphere (TOA) biases in radiative fluxes, and the preliminary solution to surface fluxes is still being tested, and unfortunately not yet in 3D. The foreseen changes, however, are not expected to change the cloud behavior much. These issues will be addressed via an on-going collaboration with R. Neggers (KNMI) and will be resolved soon.

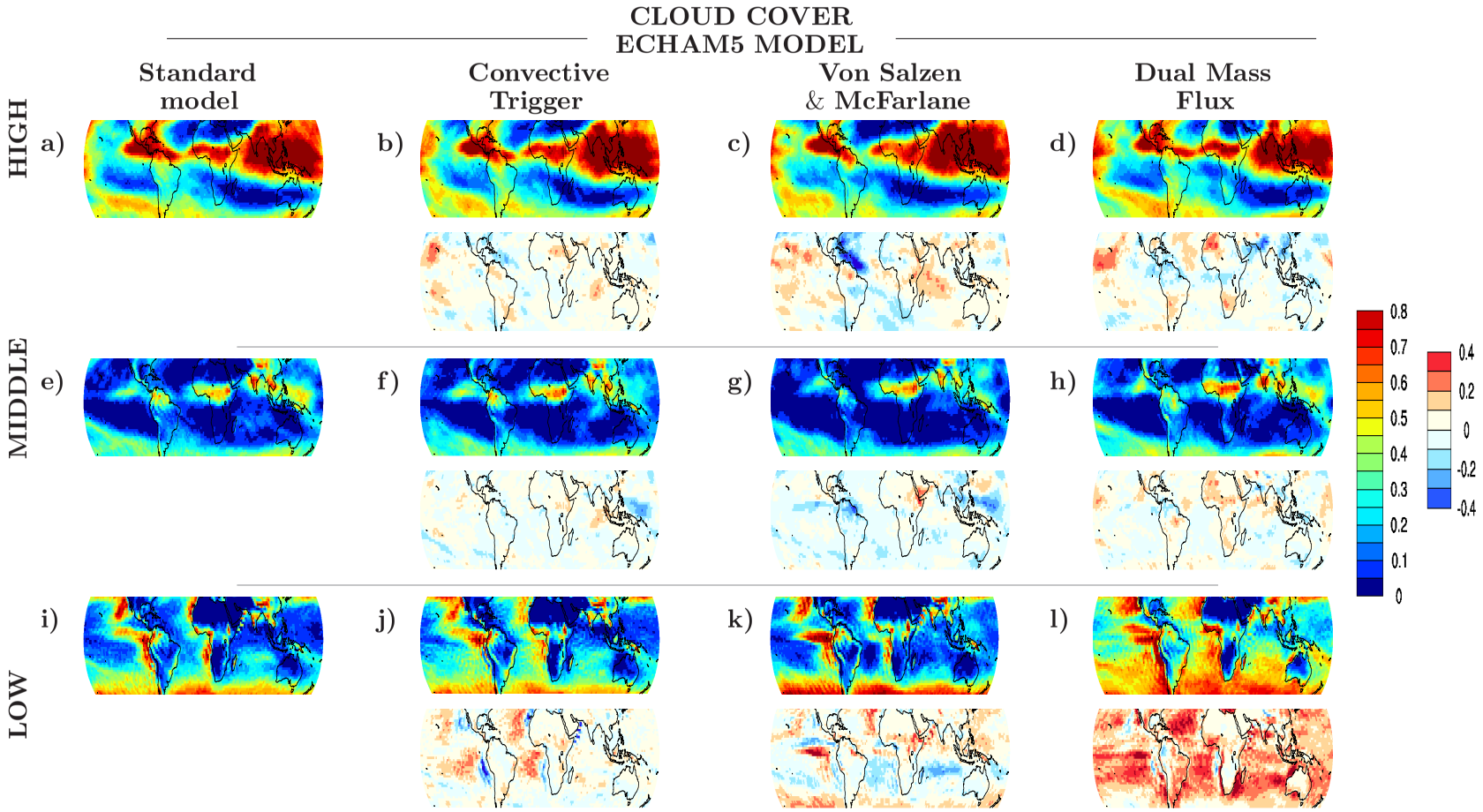

Figure 5.3— High, mid, and low-level cloud cover maps from 45 °N to 45 °S, including differences to the standard scheme, for the three new boundary layer schemes (JJA 2007).

5.2 Comparison of Boundary Layer schemes

The comparison of the three new boundary layer schemes will be broken up into three sections: (i) the purely modelled cloud cover; (ii) the cloud cover as determined by the lidar simulator; and (iii) the reflective properties of hydrometeors as determined by the radar simulator. The comparison of the three schemes will be initially made with the standard ECHAM5 model as it is vital to understand the differences amongst model versions before beginning the analysis with the satellite simulators. This will be followed by the comparison of the new schemes with the CALIPSO and CloudSat satellite retrievals.

5.2.1 Differences in purely modelled cloud cover

The comparison of the high, middle, and low-level cloud fractions will specifically focus on the regions from 45 °N to 45 °S which, as seen in Chapter 4, are poorly represented in standard ECHAM5. The modelled cloud fraction of each scheme is presented in Fig. 5.3 along with their respective differences to the ECHAM5_Std cloud cover. For clarity the following analysis is divided into three parts: comparison of the high-level cloud fraction produced by the three new schemes and standard ECHAM5, followed by the mid and low-level clouds. Understanding the changes in the high-level clouds, however, requires an appreciation of the changes to low-level clouds.

Differences in high-level cloud cover

In general all three schemes have distributions of high-level cloud cover similar to the ECHAM5_Std model, although the three schemes show a slight increase in the cloud cover. The differences in high-level cloud cover are generally less than ± 20 %, though there are localized regions in which the cloud cover changes by ± 20 % (i.e. over Hawaii). Both ECHAM5_VSMF and ECHAM5_DMF have more pronounced regional differences compared to the ECHAM5_Std than ECHAM5_Trig model (e.g. less high-level clouds over the Gulf of Mexico and also over continental mid-latitudes of the Northern Hemisphere). The regional differences vary amongst the schemes and share only one common feature which is an increase in the cloud cover over the western Pacific. Thus, it is likely the general increase in the high-level cloud cover is caused by reasons unique to each scheme.

In the case of ECHAM5_Trig the new formulation of the convective trigger has lead to a more stringent governance of buoyant parcels of air. Parcels previously satisfying the criteria for shallow convection no longer succeed. The implications are three-fold: (i) the frequency of shallow convection decreases; (ii) only the strongest convective events spur convection; and (iii) convection now stems from a moister boundary layer implying a larger transport of moisture to the higher atmosphere.

The increase in high-level Tropical cloud cover in the ECHAM5_VSMF model has been

attributed to an increase in the frequency of mid-level convection in the Tropics in Isotta (2010). Since mid-level and deep convection is represented by the Tiedtke (1989) scheme, which is known to have small entrainment and detrainment rates, strong detrainment occurs at the cloud top accounting for the high-level Tropical clouds.

The ECHAM5_DMF model shows an overall increase in the high-level cloud cover, particularly over the oceans, however, there is in fact a decrease in the cloud cover over the ITCZ. This is because the ECHAM5_DMF allows for more vertical mixing throughout the atmosphere column compared to the Tiedtke (1989) scheme, and is therefore less likely to form convective anvils at the tropopause. Hence, there is a decrease in cloud cover over the ITCZ.

Differences in mid-level cloud cover

In regards to the mid-level cloud cover all three schemes show very little change to the standard model, remaining within a range of $\pm$ 20 % of the ECHAM5_Std cloud cover. The differences which do exist amongst the mid-level clouds of the schemes differ in both sign and region. For example, both the ECHAM5_Trig and ECHAM5_VSMF models generally show a decrease in cloud cover over the oceans, whereas the ECHAM5_DMF shows an increase of cloud cover over the continents. As previously discussed, the ECHAM5_Trig and ECHAM5_VSMF schemes suppress the frequency of occurrence of shallow convection, implying less transport of moisture to the mid-levels. In the case of ECHAM5_DMF, more mixing throughout the atmosphere implies the cloud tops will be lower than previously determined, hence, slightly more mid-level clouds particularly over the land where convection is stronger.

Differences in low-level cloud cover

As expected the greatest difference between the three new schemes and the standard model is in the low-level cloud cover. In the ECHAM5_Trig model the convective trigger acts to suppress spurious convection, reducing ventilation of the boundary layer by shallow convection. This allows moisture to build up within the boundary layer, increasing the amount of low-level clouds particularly over the oceans.

In general, the increase in low-level cloud cover of ECHAM5_VSMF is not as great as the changes seen in ECHAM5_Trig. The increase, however, can be attributed to the reduction in vertical mixing of moisture resulting from a lower frequency of shallow convection activity (Isotta, 2010). Unlike ECHAM5_Trig, these changes are not systematic. For example, not all cumulus regions show an increase in cloud cover, in fact over the southern Atlantic ocean there is a large decrease in cloud cover. Isotta (2010) attributes the decrease in mid-latitude low-level clouds to an increase in shallow convection that leads to a decrease in liquid water path and reduced cloud cover

In comparison to the ECHAM5_Trig and ECHAM5_VSMF models, the ECHAM5_DMF shows the largest difference in cloud cover compared to ECHAM5_Std. The low-level cloud cover over the (Sub)Tropical oceans increases significantly; over 30 % in many regions (e.g. Atlantic ocean). While an increase in cloud fraction of 20 to 30 % may appear extreme, bear in mind ECHAM5 had cloud fractions of less than 10 % in many regions, which is well below values retrieved from satellites. The production of clouds in the ECHAM5_DMF model is the result of the different transport and cloud schemes employed, which has a double moment PDF. Depending on the skewness of the PDF, with the same moisture in the boundary layer, more clouds can be produced. As with the other two schemes, the ECHAM5_DMF shows a decrease in the stratocumulus cloud cover directly off the continents.

Summary of differences of the purely modelled clouds

In summary, three new low-level cloud parameterizations have been compared with the ECHAM5_Std model. The cloud cover maps demonstrated that all three schemes improve the low-level cloud cover, particularly over the oceans. Of the three schemes, the ECHAM5_DMF produced the greatest amount of oceanic low-level clouds in the (Sub)Tropics. Although the ECHAM5_DMF is still a preliminary version, of the three new boundary layer cloud parameterizations, the ECHAM5_DMF improves the cloud cover over the ocean while maintaining stratocumulus cloud cover. The ECHAM5_Trig also improves the oceanic cloud cover, however, the stratocumulus cloud cover is reduced. The three new schemes also prove that some of the stratocumulus cloud deck in ECHAM5_Std is caused by artificial triggering of shallow cumulus clouds.

Changes to the low-level clouds impact the mid- and high-level clouds. The comparison of the four parameterization schemes is summarized in regards to zonal cloud fraction in Fig. 5.4. The zonal plots reiterate the slight increase in high-level cloud cover in some regions, very little change in mid-level clouds and a larger change to the low-level cloud cover.

5.2.2 Cloud Radiative Forcing

The cloud radiative forcing (CRF) is a common measure of the impact of clouds on the Earth's radiation budget. CRF refers to the radiative impact of clouds on the Earth's radiation budget at TOA (Eq. 5.3), where positive values indicate a warming of the system while negative values indicate cooling.

$$\begin{aligned} CRF|_{net} &= (LW_{\uparrow} - LW_{\uparrow clearsky}) + (SW_{\uparrow} - SW_{\uparrow clearsky}) \\ &= CRF|_{LW} + CRF|_{SW} \end{aligned} \tag{5.3}$$

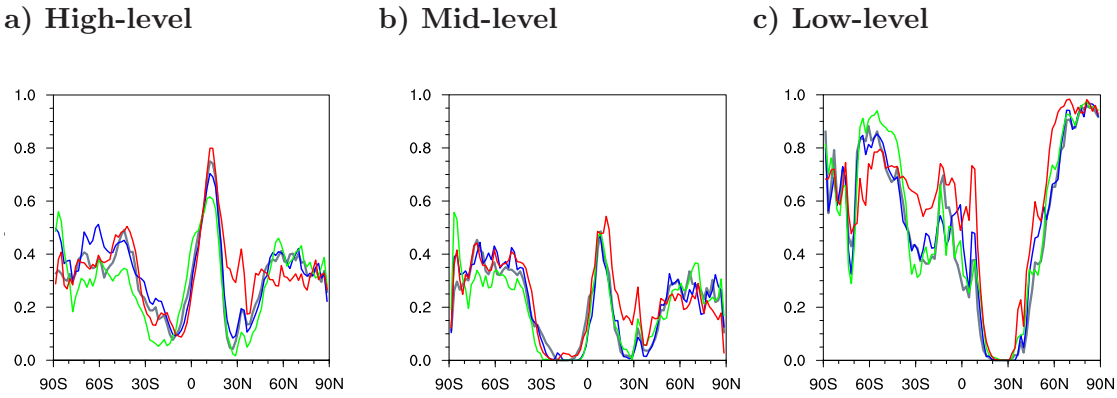

Figure 5.4— Zonal cloud cover for (a) high, (b) mid, and (c) low-level of each scheme. ECHAM5_Std (Gray), ECHAM5_Trig (blue), ECHAM5_VSMF (green) and ECHAM5_DMF (red).

The $CRF|_{net}$ is commonly divided into outgoing long-wave (LW) and shortwave (SW) components. These components are determined by calculating the difference in LW and SW radiation of the system with and without clouds (i.e. clear sky conditions), thereby isolating the radiative impact of clouds. From Eq. 5.3 it can be seen that the CRF depends on the properties of the clear sky conditions (surface albedo, aerosol load, atmospheric absorption) and cloud properties (optical depth, vertical distribution and cover) (Karlsson et al., 2008). In general, the shortwave component is negative as clouds reflect incoming solar radiation, reducing the energy entering the system, thus having a cooling effect. The long-wave component is typically positive as clouds emit at a lower temperature, thereby having a warming effect.

In the following tables, the global mean CRF of each schemes are presented. Note that the $*$ is simply a reminder that the ECHAM5_DMF is a preliminary version which is not yet coupled with the radiation scheme.

The $CRF|_{net}$ of the ECHAM5_Std, ECHAM5_Trig and ECHAM5_VSMF schemes are nearly identical (Table 5.1). Since it appears that the projected cloud fraction of the three schemes are very similar, it is not surprising that the CRF$|_{net}$ are similar. The slight changes to the $CRF|_{net}$ are mainly the result of differences in the $CRF|_{SW}$ and indirectly the differences in low-level cloud cover. Although ECHAM5_Trig has a greater amount of low-level cloud cover compared to the ECHAM5_Std model, its CRF$|_{net}$ is lower. Comparably, the ECHAM5_VSMF model has greater amount of low-level cloud also, yet its CRF$|_{net}$ is larger compared to the ECHAM5_Std. This implies that within the boundary layer, the three schemes have different geographical distributions of cloud types.

Further study of the low-level cloud fraction over the ocean is done by first identifying areas of large-scale subsidence (refer to Chp. 4.7). The area of dynamical subsidence is further divided into stratocumulus and shallow cumulus cloud cover (Table 5.2). The total

Table 5.1— Global-mean Cloud Radiative Forcing (CRF) for JJA 2007.

Experiment	CRF$\|_{SW}$ [W m^{-2}]	CRF$\|_{LW}$ [W m^{-2}]	CRF$\|_{net}$ [W m^{-2}]	Total cld frac.(%)	Low cld frac.(%)
Standard	-49.7	28.2	-21.6	64.52	37.55
Trig	-49.4	28.3	-21.0	65.01	39.12
VSMF	-50.1	28.1	-22.0	65.40	40.37
DMF *	-64.7	31.3	-33.5	70.63	49.10

area covered by subsidence is very similar for all schemes, as are the areas of dynamically defined stratocumulus and shallow cumulus. The associated $CRF|_{SW}$, however, differ. Between the ECHAM5_Std, ECHAM5_Trig and ECHAM5_VSMF models, the $CRF|_{SW}$ differs by ~ 6 W m^{-2} in the stratocumulus region even though the dynamically defined area only differs by 0.08 %. Similarly, the shallow cumulus clouds have a ~ 6 W m^{-2} with only a 1 % difference in the dynamically defined area. This implies that the cloud properties of each cloud regime within each of the three parameterizations are very different. Thus, changing the low-level cloud cover parameterizations has a profound effect on the $CRF|_{SW}$, particularly those overlying the dark ocean surface.

Table 5.2— Cloud Radiative Forcing: Area of dynamical subsidence over the global ocean for JJA 2007.

Experiment	Over Ocean					
	Total	Total	Stratocumulus		Shallow Cumulus	
	CRF $\|_{SW}$ [W m^{-2}]	Dyn. Sub. area(%)	CRF $\|_{SW}$ [W m^{-2}]	Dyn. Sub. area(%)	CRF $\|_{SW}$ [W m^{-2}]	Dyn. Sub. area(%)
Standard	-32.2	24.33	-54.7	3.48	-28.5	20.85
Trig.	-35.5	23.85	-50.3	3.37	-33.1	20.48
VSMF	-35.4	24.11	-56.9	3.45	-26.9	19.86
DMF *	-56.7	24.12	-61.6	3.66	-55.9	20.46

5.2.3 Difference in lidar detected cloud cover

As in the previous chapter the lidar simulated cloud cover maps for the three new parameterization schemes will be evaluated against ECHAM5_Std in terms of high, mid and low-level clouds. Additionally, the schemes will be compared with the CALIPSO satellite retrievals.

Difference in lidar high-level cloud cover

The high-level cloud cover of the three schemes, as derived by the lidar simulator, have very similar distributions to ECHAM5_Std (Fig. 5.6 a - e). This is not unexpected as the purely modelled cloud cover of the three schemes, previously shown in Fig. 5.3, did not show

much change compared to ECHAM5_Std. The three schemes, however, show a decrease in the area covered by the highest cloud fractions (i.e. over the Tropical West Pacific). Compared to the CALIPSO satellite retrievals, the four models continue to show good agreement in cloud amount though the high-level cloud cover is slightly overestimated by the models within the ITCZ and underestimated in the subsiding branches of the Hadley cell.

Difference in lidar mid-level cloud cover

The differences amongst the purely modelled mid-level clouds of the three schemes and ECHAM5_Std were shown to be relatively small (Fig. 5.3); and as such the lidar simulator shows very little difference amongst the mid-level clouds (Fig. 5.6 f - j). Unfortunately, none of the new schemes improves the mid-level cloud cover and the mid-level cloud amounts remain vastly underestimated compared to the satellite retrievals.

Difference in lidar low-level cloud cover

The low-level cloud cover derived by the lidar simulator, rather surprisingly, shows little difference amongst ECHAM5_Std, ECHAM5_Trig and ECHAM5_VSMF models (Fig. 5.6 k - o). According to Fig. 5.3, both the ECHAM5_Trig and ECHAM5_VSMF have showed improvements in the (Sub)Tropical low-level cloud cover, including significant regional increases over 20 %. This, however, is not evident from the low-level cloud cover maps produced by the lidar simulator. Evidently, the lidar simulator does not capture all changes in the modelled low-level cloud cover.

Take for example the ECHAM5_Trig model, focusing on the stratocumulus region off the west coast of South America it can be seen that indeed some of the cloud cover changes were captured, however, a vast majority of the clouds over the ocean were not. Further study of this phenomenon has shown that mainly regions with a modelled cloud cover greater than ~ 30 % are captured, though underestimated, by the lidar simulator. Recalling that clouds are identified by the lidar simulator if the diagnosed scattering ratio of a grid-box surpasses a defined threshold. Clearly low cloud fractions return scattering ratios which do not exceed the cloud threshold and as a result the lidar simulator indicates less low-level cloud cover. This is likely exacerbated in areas where high-level clouds have already weakened the lidar's intensity. In the case of the ECHAM5_Trig model, whilst the low-level cloud cover improved on the order of 10 % to 20 %, the previous cloud cover in many areas were closer to 0 % and so the cloud optical thickness remains below the threshold which the lidar simulator captures. As a result, the low-level cloud fraction derived the lidar simulator for both the ECHAM5_Trig and ECHAM5_VSMF models remain nearly identical to the ECHAM5_Std model. Thus, the ECHAM5_Trig and ECHAM5_VSMF models appear to underestimate the lidar derived low-level cloud cover compared to the

CALIPSO satellite retrievals. Future sensitivity studies regarding the exact threshold of cloud cover necessary for the liar simulator to accurately detect clouds would be useful.

Of the three new boundary layer schemes, the lidar simulator best captures the changes made by the ECHAM5_DMF model. Fig. 5.3 demonstrated that the low-level cloud cover increased significantly in the ECHAM5_DMF model; particularly over the oceans. As a result the low-cloud cover derived by the lidar simulator also shows an improvement. Although the modelled cloud cover of the ECHAM5_DMF model is greatest of all the schemes and best captures the low-level ocean clouds; compared to the low-level cloud cover retrieved by the CALIPSO satellite, the low clouds remains underestimated, particularly in the stratocumulus regions.

a) High-level **b) Mid-level** **c) Low-level**

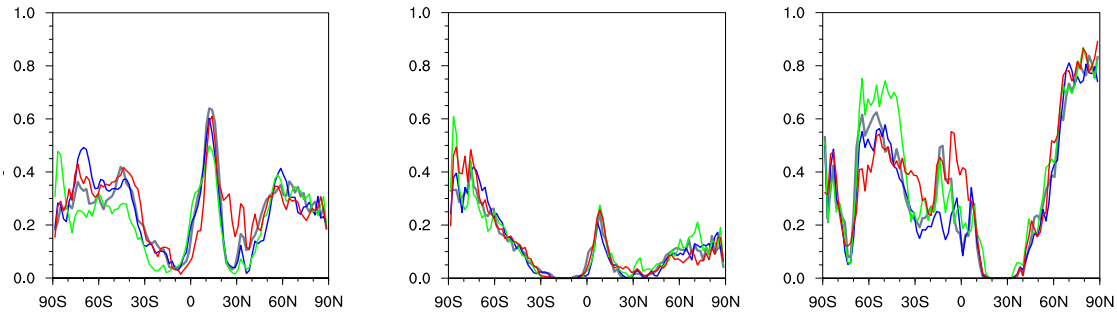

Figure 5.5— High, mid, and low-level zonal cloud cover for each scheme as seen by the lidar simulator. ECHAM5_Std (Gray), ECHAM5_Trig (blue), ECHAM5_VSMF (green) and ECHAM5_DMF (red).

Summary of differences in lidar cloud cover

In summary, the evaluation of the ECHAM5_Trig, ECHAM5_VSMF and ECHAM5_DMF schemes using the lidar simulator with the purely modelled results demonstrated that the lidar simulator diagnoses less the cloud cover (Fig. 5.4 and 5.5), particularly where there are few low-level clouds. The lidar derived cloud cover maps also show that the changes made by the ECHAM5_Trig and ECHAM5_VSMF to the low-level clouds were not captured by the lidar simulator. This implies that many of the new low-level clouds produced by the schemes occur below higher-level clouds and that many of the low-level clouds produced are optically thin.

Since the lidar simulator did not capture the changes to the boundary layer clouds of the ECHAM5_Trig and ECHAM5_VSMF scheme, the lidar derived low-level clouds of these schemes are very similar to the ECHAM5_Std model and as such appear to underestimate the low-level clouds compared to CALIPSO satellite retrievals.

The lidar simulator captures the increase in low-level cloud cover made by the ECHAM5_DMF model best. Despite the vast improvement and the high cloud fraction

modelled, the lidar simulator indicates that it too still underestimates the low-level cloud cover compared to satellite retrievals.

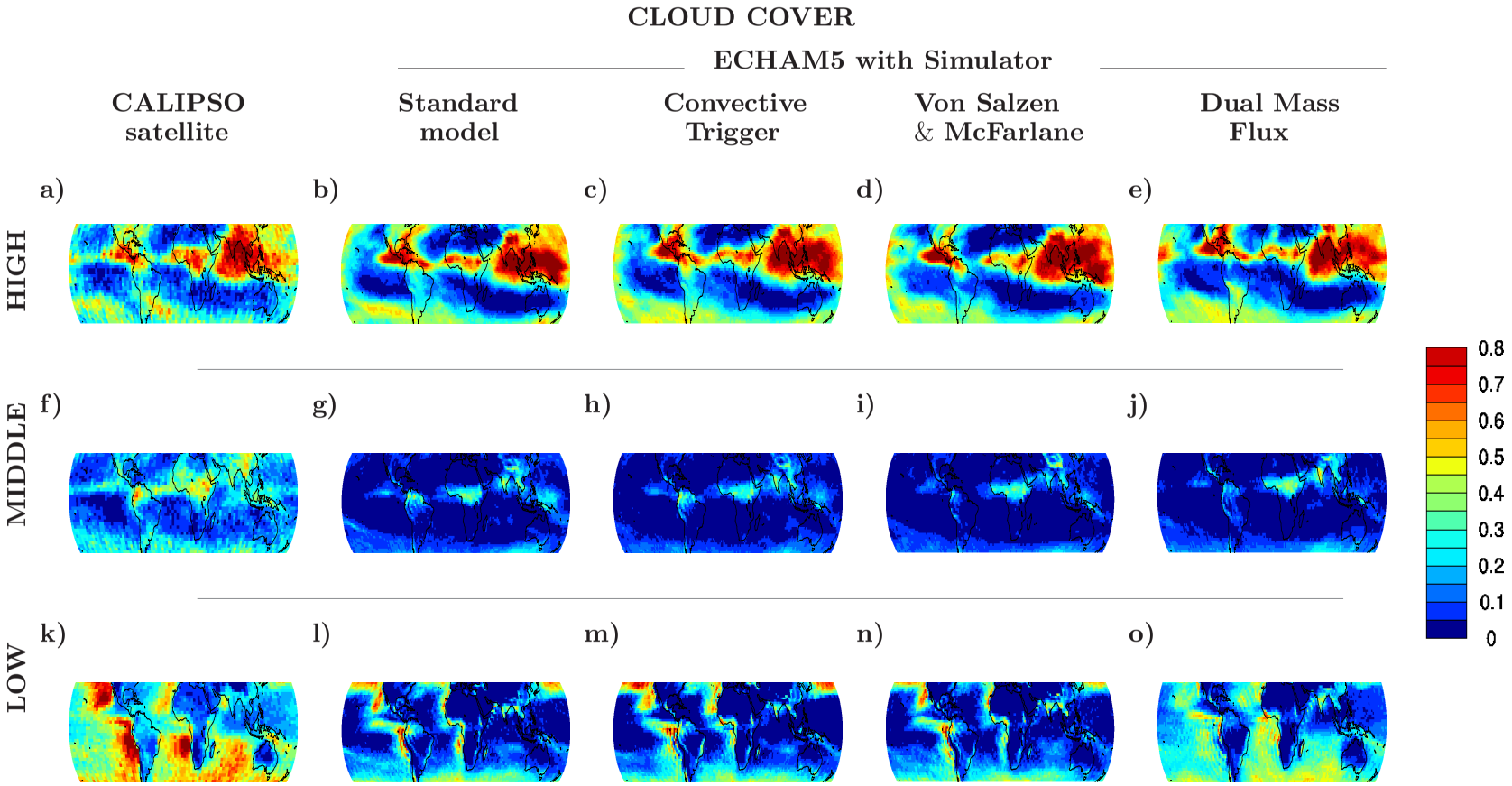

Figure 5.6— High, mid, and low-level cloud cover maps for JJA 2007 from $45\,^{\circ}\mathrm{N}$ to $45\,^{\circ}\mathrm{S}$. Left to Right: CALIPSO satellite retrievals, Standard ECHAM5, Convective Trigger, Von S. & McF., and Dual Mass Flux. All model versions include the lidar simulator.

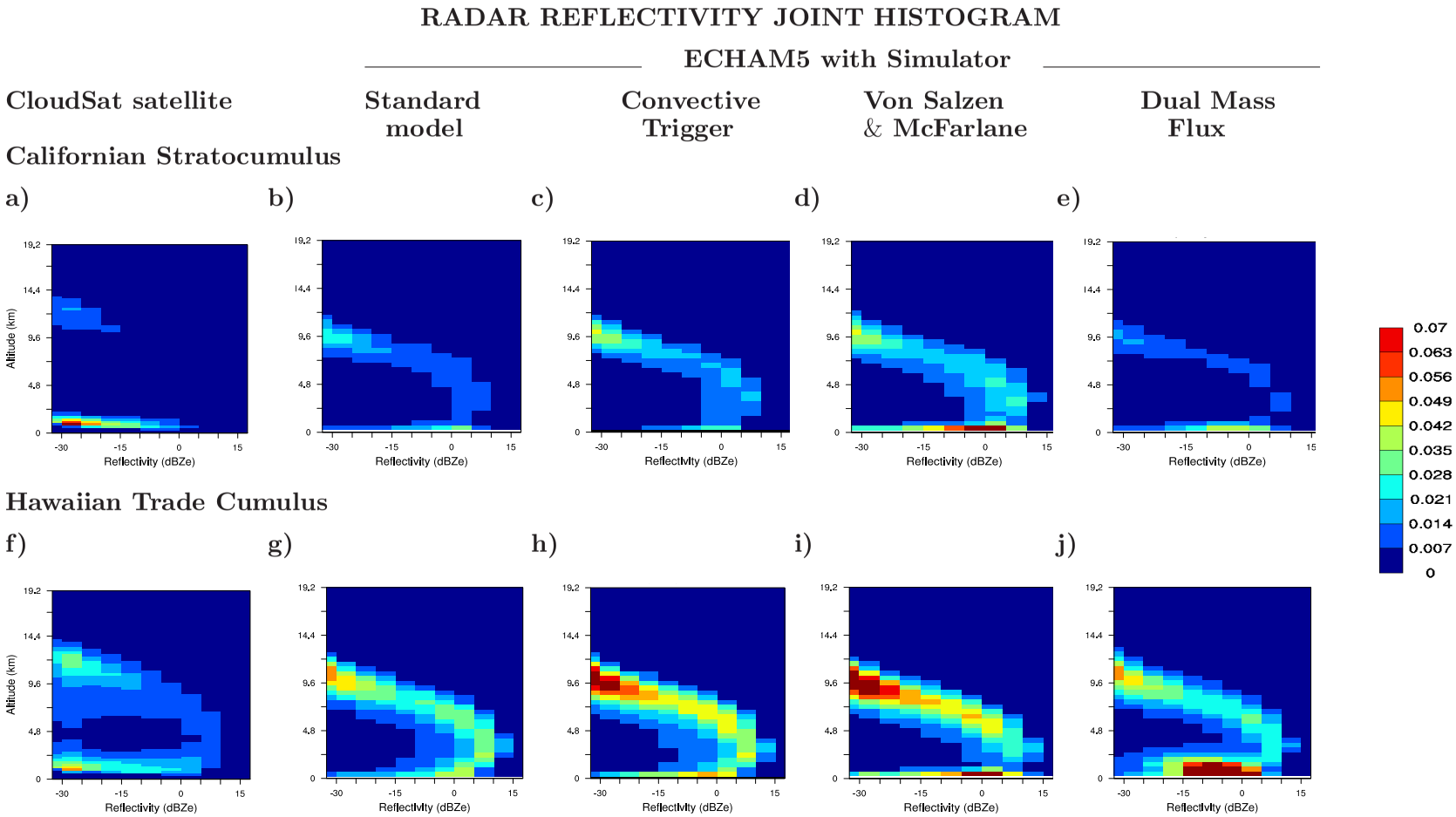

Figure 5.7— Cloud Altitude-Reflectivity Histogram for the Californian Stratocumulus and Hawaiian Trade Cumulus Cloud Regimes for JJA 2007.

5.2.4 Using CloudSat Radar Observations and Simulator

In Chapter 4.5 the regional joint histograms of cloud altitude and radar reflectivity for four different regions were introduced. In this section, the radar reflectivity histograms of the three boundary layer parameterization schemes will be evaluated for the Californian stratocumulus and Hawaiian shallow cumulus regions (Fig. 5.7). The radar reflectivity histograms are very useful in evaluating the regional distributions of clouds and precipitation. For this study four quadrants of the histogram, which can be roughly divided into liquid and ice hydrometeors around the 5 km mark, and precipitating vs. non-precipitating hydrometeors at reflectivities of -15 dBZe, will be compared. Unlike Chapter 4.5 this study will not be divided amongst regions, but rather amongst the three parameterization schemes. The evaluation according to scheme, when comparing the results with the ECHAM5_Std and CloudSat retrievals, will assure that the changes have been caused by the parameterizations.

Difference in radar reflectivities to ECHAM5_Std

Comparison of the Californian stratocumulus histograms of the ECHAM5_Std and ECHAM5_Trig models show an increase in the frequency of occurrence of high-level non-precipitating ice clouds (Fig. 5.7). The increased transport of moisture to the upper atmosphere is caused by convective events which stem from a moister boundary layer. The additional moisture brought into the upper atmosphere increases the likelihood of precipitation at high altitudes as seen in the radar reflectivity histogram (> -15 dBZe). In fact, all altitudes of ECHAM5_Trig show an increase in the frequency of precipitation occurrence (> -15 dBZe) compared to the ECHAM5_Std model. The increase in precipitation frequency, however, is mostly at a lower intensity since many of its reflectivities are between -5 to 0 dBZe. It should be noted that in the lowest level, the reflectivity of the precipitation decreased. Despite the increase in precipitation frequency, the likelihood of detecting low-level non-precipitating clouds with the radar simulator did not increase. In fact fewer low-level clouds in the non-precipitating part of the histogram are detected even though there are more low-level clouds modelled (Fig. 5.8). Since it is not likely the radar signal became attenuated under the given conditions, it implies that the low-level clouds modelled are optically thinner than in the ECHAM5_Std model. This corroborates the conclusions derived from the lidar simulator. This effect may be exacerbated if effective radius of cloud liquid water is underestimated. The Hawaiian shallow cumulus radar reflectivity histograms shows many of the same features as the Californian stratocumulus; including the increase in high-level ice clouds and frequency of precipitation. Unlike the Californian region, however, more non-precipitating boundary layer clouds develop.

As with ECHAM5_Trig model, the ECHAM5_VSMF shows a greater frequency of high-level ice clouds and precipitation compared to ECHAM5_Std in the Californian stratocu-

mulus region (Fig. 5.7). The increase in precipitation frequency generally occurs in regions of high radar reflectivities, indicative of large hydrometeors and hence strong precipitation events. This is consistent with the conclusions of Isotta (2010) who determined ECHAM5_VSMF increased the frequency of mid-level convection in the Tropics. The increase in convection events provides both more moisture to the upper atmosphere for precipitation in addition to larger particles and higher reflectivities. In regards to the lowest layers of the atmosphere the ECHAM5_VSMF shows a significant increase in precipitation frequency, which is due to the incorporation of the life-cycle of shallow cumulus clouds. Abrupt detrainment at the end of the shallow cumulus life-cycle provides large amounts of moisture for precipitation in the low-levels of the atmosphere. This is also likely the cause of a break in the precipitation reflectivities around 2 km. Despite the increase in frequency of precipitation, the ECHAM5_VSMF model also shows an increase in the frequency non-precipitating boundary layer clouds in the Californian stratocumulus region. The same holds true for the Hawaiian shallow cumulus region.

The ECHAM5_DMF, unlike the previous two schemes, shows a decrease the frequency of high-level clouds and precipitation. This is likely due to the strong mixing within the atmospheric column which keeps the majority of the moisture with the lowest layers of the atmosphere. Thus, there is a reduction in the amount of moisture transported to the upper atmosphere. The development of non-precipitating boundary layer clouds is not evident as the peak in reflectivities remains in the precipitating half of the histogram, obscuring the clouds. There is, however, a slight shift towards lower radar reflectivities. In the Hawaiian shallow cumulus region, the most prominent feature is the increase of low-reflectivity hydrometeors in the lowest-levels, particularly in the non-precipitating region of the histogram. Though the ECHAM5_DMF overestimates the frequency of precipitation at the lowest levels, it is the only scheme which succeeds to increase the amount of non-precipitating boundary layer clouds significantly and improve the higher altitude clouds.

Difference in radar reflectivities to CloudSat retrievals

Despite the fact the lidar simulators did not show much difference amongst the cloud cover of the ECHAM5_Std, ECHAM5_Trig and ECHAM5_VSMF schemes, the distribution of water in the atmospheric column is quite different, particularly within the precipitating half of the radar reflectivity histogram. All schemes have a significantly larger precipitation frequency compared to the CloudSat satellite retrievals. Both the ECHAM5_Trig and ECHAM5_VSMF schemes vastly overestimate the transport of moisture into the high-levels, and consequently the high-level precipitation. Only the ECHAM5_DMF shifts the peak frequency of occurrence towards lower reflectivities, though the peak remains in the precipitating half of the histogram. None of the schemes are able to capture the peak in

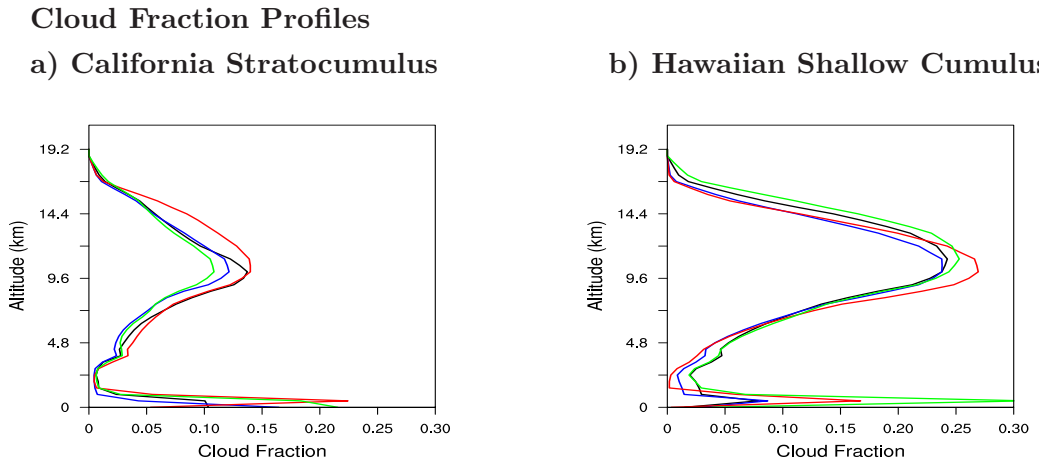

Figure 5.8— Regional cloud fraction profiles for JJA 2007: ECHAM5_Std (black); ECHAM5_Trig (Blue); ECHAM5_VSMF(Red); ECHAM5_DMF(Green).

the non-precipitating boundary layer clouds that is seen in the satellite retrievals. Though all schemes show different distributions of radar reflectivities, the differences amongst the schemes are less than their respective differences to the CloudSat retrievals. The ECHAM5_DMF model, despite being a preliminary version, best resembles the CloudSat retrievals. Since precipitation dominates the radar signal it may be of interest to take a closer look at the partitioning of convective and large-scale precipitation between the schemes. This will be done in the next section.

5.3 Changes in precipitation

The radar reflectivity histograms of each new parameterization scheme shows a frequency of precipitation greater than retrieved by CloudSat. In order to understand the differences in the radar reflectivity histograms of the three schemes, the differences in precipitation must first be considered. As in Chp. 4.5 the division of precipitation amongst large-scale and convective precipitation is presented for the region of Hawaii for varying precipitation intensities. As in the global scenario, the greatest frequency of precipitative events are large-scale low-intensity events (Fig. 5.9). The convective events occur more frequently at much greater intensities. Compared to the global model, the Hawaii region of ECHAM5_Std shows an increase in the lowest intensity precipitation events. The following section looks at the differences in precipitation frequency of the three schemes compared to ECHAM5_Std.

Of the three new parameterization schemes, the changes in the ECHAM5_Trig precipitation frequency are the smallest (i.e. less than 0.25). The large-scale precipitative events show a decrease in the lowest intensity events and an increase in the mid-range events. Similarly convective events show a decrease in the frequency of occurrence in the lowest

intensity events and an increase in the highest intensity events. This most likely caused by the suppression of shallow convection which implies that only the strongest convective events are allowed to develop. This in turn transports moisture more effectively to higher altitudes, acting as an input to the large-scale moisture budget and thus increasing the intensity large-scale precipitation.

The greatest changes in precipitation occur in the ECHAM5_VSMF scheme. Although Isotta (2010) states ECHAM5_VSMF does not change the amount of surface precipitation, there is a significant change in the partitioning of large-scale and convective precipitation. Focusing on the convective precipitative events, there is a significant increase in the frequency of precipitation in the lowest intensity precipitation bin. Conversely, high intensity convective precipitation events decrease significantly. Both of which are likely due to the inclusion of the life-cycle of shallow cumulus and detrainment of moisture. The large-scale precipitation shows a decrease of the lowest intensity events and an increase in the mid-intensity events. The changes to the large-scale precipitation events are likely due to the abrupt detrainment of moisture into the atmosphere at the end of the shallow cumulus life cycle.

The ECHAM5_DMF shows the greatest change in large-scale precipitation. As in the other two schemes, but to a larger extent, there is a decrease in the frequency of precipitation in the lowest intensity bin and an increase in the mid-level intensity bin of large-scale precipitation. The convective precipitation shows a distribution of changes, with an increase in the lower intensity events and a decrease in the highest intensity events. This is likely due to the increase in low-level cloud amount which increases the likelihood of higher intensity precipitation.

In summary all three schemes show a decrease in the frequency of the low-intensity bin of large-scale precipitation and increase in the mid-intensity of precipitation. In regards to the convective precipitation, there are no systematic changes in the distribution of precipitation intensities. Despite the fact that the radar simulator shows an overestimation of precipitating hydrometeors in the histograms, the three new schemes all show an improvement in the distribution of precipitation at the surface.

5.4 Conclusions

In this chapter, four different representations of boundary layer clouds were compared with satellite retrievals using the CALIPSO and CloudSat simulators. Along with the standard ECHAM5 model, the three new parameterizations included a modified version of the Tiedtke (1989) scheme (ECHAM5_Trig), a bulk parameterization of transient shallow cumulus clouds (ECHAM5_VSMF), and a dual mass flux scheme (ECHAM5_DMF).

From the plots of purely modelled cloud cover, the high- and mid-level clouds show

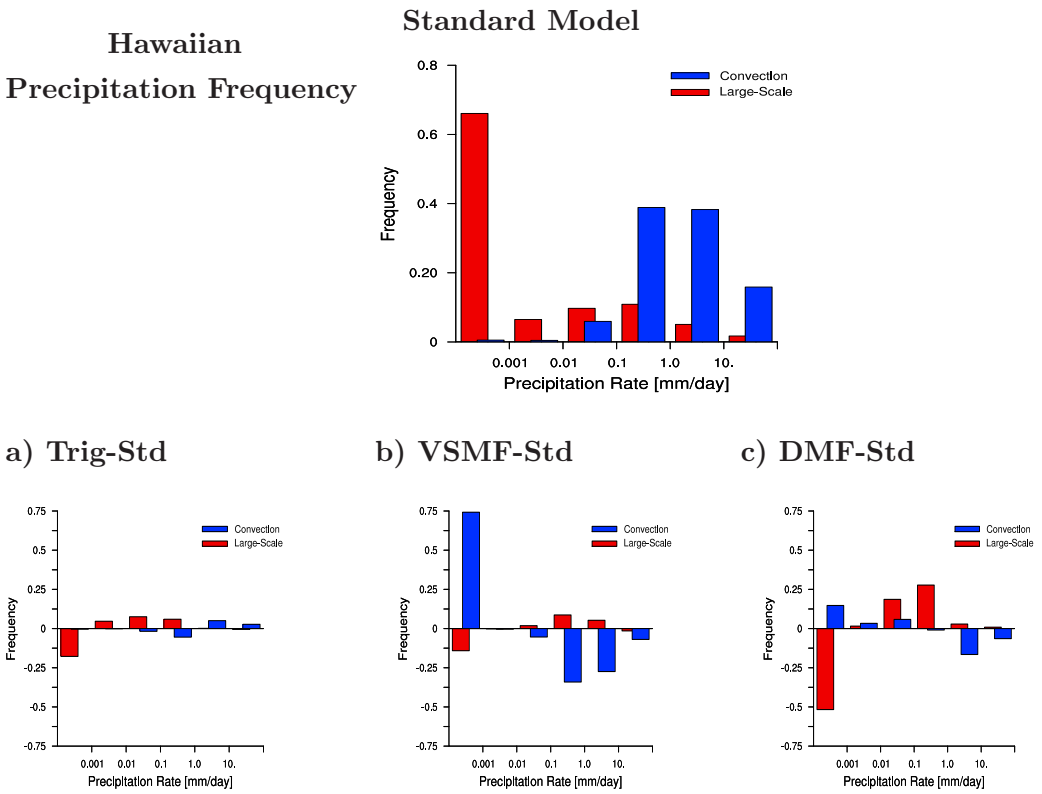

Figure 5.9— Frequency of occurrence of large-scale and convective precipitation events of varying intensities over Hawaii (JJA 2007). Top: ECHAM5_Std. Bottom: (Left) Difference between ECHAM5_Trig and ECHAM5_Std; (Middle) Relative difference between ECHAM5_VSMF and ECHAM5_Std; and (Right) Difference between ECHAM5_DMF and ECHAM5_Std.

very little difference compared to the ECHAM5_Std model. All three models improve the low-level cloud cover, particularly over the oceans. Of the three schemes, the preliminary version of ECHAM5_DMF produces the most low-level clouds, followed by the ECHAM5_VSMF and ECHAM5_Trig. The projected cloud cover of the ECHAM5_Std, ECHAM5_Trig and ECHAM5_VSMF models do not differ much; and as such the radiative balances and cloud radiative effects at the top of the atmosphere are very similar.

The lidar simulator does not capture much of the change to the low-level cloud cover in the ECHAM5_Trig and ECHAM5_VSF models, especially where the cloud cover is low. This implies that many of the changes to the low-level cloud cover occur below high-level clouds and that the new clouds may be optically thin. The lidar simulator also shows less increase in the low-level cloud cover by the ECHAM5_DMF, but of the three new schemes, this scheme most resembles the CALIPSO satellite retrievals. All three models still underestimate the low-level cloud compared to the retrievals.

Despite the fact that the projected cloud covers appear very similar from the lidar simulator diagnoses, the radar simulator shows us that the distribution of moisture in the atmosphere is different amongst the schemes. It appears that increasing the low-level cloud cover also increased frequency of high-level clouds in the regions investigated. This

is likely because convection stemming from a moister boundary layer transports more moisture to the higher altitudes. Since deep- and mid-level convection in ECHAM5_Trig and ECHAM5_VSMF are still parameterized by Tiedtke (1989), known for overestimating the mass-flux, it is not surprising that the frequency of high-level clouds is overestimated according to the radar joint cloud altitude-reflectivity histogram. If high-level ice clouds are present, their impact on the out-going long wave radiation may cancel out the changes in short-wave radiation due to increased low-level cloud cover. The overestimation in the frequency of high-level clouds may also lead to the overestimation in high-level precipitation seen in the radar reflectivity histograms. As concluded in the previous chapter, precipitation continues to be too frequent in the ECHAM5. The overly frequent precipitation, however, is not the reason non-precipitating boundary layer clouds are not detected in the radar reflectivity histograms in the Californian stratocumulus and Hawaiian shallow cumulus regions. It is more likely that the clouds produced in these two regions are optically thin. Of the three schemes, the preliminary ECHAM5_DMF model produces the most non-precipitating boundary layer clouds and shows them at slightly higher altitudes, in better agreement with CloudSat. All in all, the differences between the satellite retrievals and those simulated by the model are larger than differences amongst the schemes themselves.

From the radar reflectivity histograms, all the models show an overestimation in precipitation frequency, but further study shows that the overestimation of precipitation frequency stems from different causes. The partitioning between large-scale and convective precipitation differs for each scheme, including differences in intensity. All the schemes show an improvement by decreasing low-intensity large-scale precipitation and increase in higher intensity precipitation. There is, however, no systematic change in the convective precipitation.

Chapter 6

Cloud Climate Feedbacks

How do cloud-climate feedbacks differ due to different representations of low-level clouds?

Climate sensitivity, as defined by the Intergovernmental Panel on Climate Change (IPCC), is the change in global mean surface temperature with a a doubling of greenhouse gases (expressed as carbon dioxide equivalents) after equilibrium has been reached (Solomon et al., 2007). Climate sensitivity is dependent on many feedback parameters including water vapor, surface albedo, lapse rate and clouds. The feedbacks are both positive and negative in sign implying they will either amplify or diminish the climate system's response, respectively. Intermodel comparisons have shown that cloud feedbacks remain the largest source of uncertainty in climate sensitivity (Cess et al., 1990; Soden & Held, 2006; Ringer et al., 2006; Bony & Dufresne, 2005). For the purpose of this study, cloud feedback will be defined as the difference between a *present day* and *perturbed climate* experiments' cloud radiative forcing, following Cess et al. (1990). The cloud radiative forcing, as defined in Chp. 5.2.2, is the impact of clouds on the Earth's radiation budget at the top of the atmosphere.

In this chapter, the cloud-climate feedbacks of the three boundary layer schemes will be compared with both the standard ECHAM5 and two previous versions of ECHAM from the 1990s. The different representations of boundary layer processes implies the atmospheric dynamics and vertical distribution of cloud properties are varied, which in turn affects the radiative heating profile and hydrological cycle via convection (Stephens, 2005). Bony & Dufresne (2005) traced the main source of uncertainties in Tropical cloud feedback within climate model to marine boundary layer clouds; including stratocumulus and shallow trade cumulus. Since these low level clouds cause the largest variations in the Earth's radiation budget (Hartmann et al., 1992) and have distinct radiative effects, changes in their relative frequency of occurrence in the perturbed climate scenario may lead to different cloud feedbacks. In the following sections the sensitivity of cloud-climate feedbacks to different representations of low-level clouds, specifically shallow and stratocu-

mulus clouds, are examined.

6.1 Cloud-Climate Feedbacks

The cloud-climate feedback is calculated from the net cloud radiative forcing ($CRF|_{net}$), defined in Chp. 5.2.2, of the present day and perturbed climate experiments. The perturbed climate experiment is one in which the sea surface temperature (SST) has been increased by 2 K. This experimental setup has been found to be a simple, idealized, computationally efficient analogy to the $2\times CO_2$ climate change experiments (Cess et al., 1989). By prescribing the climate change and then deriving the radiative forcing, this setup acts as an *inverse climate change simulation* (Cess et al., 1989).

From the present day and perturbed climate experiments the differences in $CRF|net$ and global-mean radiative forcing (G) are calculated. The radiative forcing is the change in the net solar and infrared radiative fluxes at the top of the atmosphere (TOA) resulting from the +2K SST perturbation (Eq. 6.1). Note that the negative sign in front of ΔLW term accounts for the fact that outgoing radiation is negative and incoming radiation is positive at the top of the atmosphere in ECHAM5.

$$G = -(LW|_{+2KSST} - LW|_{present}) - (SW|_{+2KSST} - SW|_{present}) \tag{6.1}$$

The cloud feedback parameter (ΔCRF/G) can then be calculated. A positive ΔCRF/G means that cloud feedback acts to amplify the warming (Cess et al., 1990). A negative Δ CRF/G, however, does not necessarily imply clouds dampen climate sensitivity (Ringer et al., 2006). Soden & Held (2006) found that many of the 14 GCMs evaluated in the study demonstrated a reduction in $CRF|_{net}$, yet had positive cloud-climate feedbacks; and concluded the change in cloud radiative forcing was not a reliable measure of the sign or absolute magnitude of cloud-climate feedback. This is because ΔCRF includes a contribution from the water vapor feedback via the long-wave clear sky fluxes. In a warmer climate the clear-sky fluxes may be larger than in the present day climate, due to water vapor feedbacks. Thus, when the ΔCRF is calculated with a larger the clear-sky term (Eq. 6.1 & 5.3), the ΔCRF is reduced by some amount related to the water vapor feedback, and may potentially be negative.

The experimental set-up for the present day and perturbed climate scenario are run for a three month spin up, followed by a six month averaging time under perpetual July conditions. The experiments are run in a perpetual July mode where the sea ice and snow are held fixed to eliminate surface albedo feedbacks associated with ice/snow changes (Cess et al., 1996). In addition, soil moisture is fixed to avoid excessive drying in the perpetual July simulations. It should be noted that under the perpetual July scenario, the equator to pole temperature gradient is not taken into consideration and as such the

cloud feedbacks may not be representative of a coupled atmosphere-ocean-land model, nor one with an interactive cryosphere (Cess et al., 1996).

6.2 Cloud-Climate Feedback: Comparison of Schemes

Under the experimental set up described in Section 6.1, the cloud-climate-feedback parameters have been calculated for the standard ECHAM5 model (ECHAM5_Std), and for two of the three new boundary layer schemes described in Chp. 5.1 (Fig. 6.1). These include the convective trigger (ECHAM5_Trig) and the transient shallow cumulus (ECHAM5_VSMF). It should be noted that the cloud-climate-feedback of the third new boundary layer scheme, the eddy diffusivity dual mass flux (ECHAM5_DMF), is shown but not included in the discussion. As described in Chp. 5.1, the preliminary ECHAM5_DMF implementation is not yet in radiative balance (at time of submission), however, the ongoing collaboration with R. Neggers suggests the implementation will likely be completed in the near future.

The cloud-climate-feedback parameters of the ECHAM5_Std, ECHAM5_Trig and ECHAM5_VSMF models are plotted alongside the cloud-climate-feedback parameters of two previous versions of ECHAM (denoted as ECHAM90 and ECHAM96) published in Cess et al. (1996). Though the ECHAM GCM has evolved significantly in the last decade, it is interesting to see whether the trend of converging, moderate values of cloud-climate feedback parameters presented in Cess et al. (1996) still holds for the ECHAM model. It is also interesting to see how changes to the cloud-climate feedback parameter due to different low-level cloud parameterizations compare to the changes made to ECHAM90 and ECHAM96, and ECHAM96 and ECHAM5, respectively. The differences between the cloud-climate feedbacks of ECHAM90 to ECHAM96 are due to the inclusion of: a prognostic cloud water content, interactive cloud optical properties, a different radiative transfer code and convection scheme, and most importantly a change in the cloud optical properties. The strong positive cloud feedback in ECHAM90 had been attributed to an artifact due to the improper choice the prescribed cloud droplet radius making clouds too bright. The overly bright clouds, in combination with a reduction in cloud amount in the warmer climate, produced a strong positive SW feedback (Cess et al., 1996). The differences between the ECHAM96 and ECHAM5_Std, as described in Roeckner et al. (2003), include changes in the advection scheme, long-wave radiation scheme, prognostic equations for cloud liquid water and cloud ice, cloud micro-physics and cloud cover parameterization. The results of the previous versions of ECHAM are comparable with the ECHAM5 experiments as they have identical experimental setups.

The cloud feedback parameters (ΔCRF/G) of the three ECHAM5 experiments all show a positive feedback (Fig. 6.1), similar to the experiments of Soden & Held (2006). A positive feedback implies an amplification of the surface warming. This changes the

vertical distribution of water vapor, liquid water and ice crystals in the atmosphere, and thereby the radiative balance a the top of atmosphere radiation, temperature profile of the atmosphere and hydrological cycle.

In Cess et al. (1990) and Cess et al. (1996), the cloud-climate feedbacks of 19 GCMs were compared. In both cases, the cloud-climate feedback parameters remained within the range of -0.5 to 2. In Cess et al. (1990) the models demonstrated a wide spread in cloud-climate feedbacks, which narrowed considerably in Cess et al. (1996) when the majority of cloud-climate feedback parameters became more modest in nature (i.e. ΔCRF/G < 0.5). Compared to the Cess et al. (1996) models, ECHAM5_Std, ECHAM5_Trig and ECHAM5_VSMF have large cloud-climate feedback parameters (i.e. ΔCRF/G > 1.0). Thus, the trend towards converging, moderate values of cloud-climate feedbacks does not hold for the ECHAM GCM.

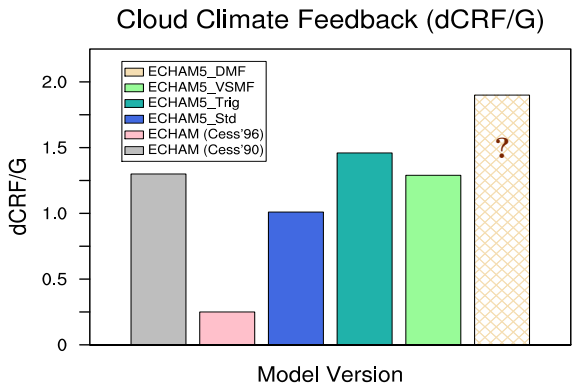

Figure 6.1— The cloud feedback parameters (ΔCRF/G) of the ECHAM5_Std, ECHAM5_Trig and ECHAM5_VSMF models under perpetual July conditions following Cess et al. (1990) alongside two older versions of ECHAM.

Table 6.1— Cloud Climate Feedbacks for the ECHAM5_Std, ECHAM5_Trig and ECHAM5_VSMF models with their corresponding total and low cloud cover for the present day scenario and the associated change for in a perturbed climate.

Experiment	$\frac{\Delta CRF}{G}\|_{net}$ [W m^{-2}]	Present Total cld. cov.(%)	Δ Total cld. cov.(%)	Present Low cld. fra.(%)	Δ Low cld frac.(%)
Standard	1.01	62.16	-1.41	20.89	-1.77
Trig.	1.46	64.42	-2.06	22.86	-1.83
VSMF	1.29	64.81	-1.41	25.68	-1.80
DMF	N/A	N/A	N/A	N/A	N/A

For each model, the corresponding values of total and low-level cloud cover for the present climate, along with their respective changes in the perturbed climate scenario, are presented in Table 6.1. All three models show a decrease in the total cloud cover in a warmer climate; similar to that seen in the 19 GCMs presented in Cess et al. (1990). In order to determine the cause of the decrease in total cloud cover, it is best to look at where

the changes occurred, specifically the boundary layer clouds, to seek an explanation.

The low-level cloud cover, like the total cloud cover, also decreases in the warmer climate, which implies the large-scale environmental conditions play a greater role in the overall decrease in cloud cover than the individual cloud parameterization schemes. The amount which the cloud cover changes and the fraction which remains, in addition to the ratio of cloud type, however, depends on the parameterization. These results support the statement that differences in cloud feedbacks are due to changes in individual clouds rather than fundamental differences in the response of individual cloud types posed by Ringer et al. (2006). The changes to the low-level cloud cover are not directly echoed in the changes of total cloud cover, thus it is evident changes to low-level clouds impact high- and mid-level cloud cover, and thereby the radiation budget.

There does not appear to be a relationship between the cloud-climate feedback parameter and the initial total cloud cover nor its change in the perturbed climate. This, however, does not appear to be true for low-level clouds. The greater the changes in low-level cloud cover, the greater the cloud-climate feedback parameter.

A further study of the low-level clouds, specifically those over the oceans, is shown in Table 6.2. The area of dynamical subsidence over the oceans are separated into stratocumulus and shallow cumulus regimes according to the vertical velocity and lower tropospheric stability (described in Chp. 4.7). The area covered by dynamically defined shallow cumulus far exceeds that of the dynamically defined stratocumulus, however, the $CRF|_{SW}$ associated with the stratocumulus is nearly twice as large. The three models show an increase in the dynamical stratocumulus area and decrease in the dynamical shallow cumulus area in the warmer climate compared to the present day scenario, thus there is a stabilization of the lower troposphere. Further study of this phenomena will be presented in the following section.

Table 6.2— Cloud-Climate Feedbacks: Area of dynamical subsidence over the ocean for a perpetual July scenario (averaged over 6 months). The difference between the perturbed climate and present day scenario is included.

Experiment	Over Ocean							
	Stratocumulus				Shallow Cumulus			
	$CRF\|_{SW}$ [W m^{-2}]	$\Delta CRF\|_{SW}$ [W m^{-2}]	Dyn. sub. area(%)	ΔDyn. sub. area(%)	$CRF\|_{SW}$ [W m^{-2}]	$\Delta CRF\|_{SW}$ [W m^{-2}]	Dyn sub. area (%)	ΔDyn sub. area(%)
Standard	-55.15	11.67	4.82	1.31	-26.73	3.50	21.77	-2.44
Trig.	-58.03	11.94	4.71	1.51	-31.22	4.75	21.70	-1.18
VSMF	-67.59	1.21	2.69	1.36	-31.43	4.01	21.81	-0.67

Summary

Using three different methods of representing shallow convection in the boundary layer, a positive cloud-climate feedback for each was derived. Implications of a positive cloud-

climate feedback include further reduction of cloud cover which in turn further warms the Earth's surface. Though all three parameterizations all show a positive cloud-climate feedback, there is a spread amongst the models. The cause of the spread, however, is difficult to isolate from the three models as they employ very different parameterizations.

6.3 Cloud-Climate Feedback: Convective Trigger Sensitivity to buoyancy threshold

A sensitivity experiment was performed with ECHAM5_Trig in order to better understand the spread in cloud-climate feedbacks due to low-level clouds. As described in Chapter 5.1, the sub-grid variability of buoyancy is accounted for by calculating the variance in virtual potential temperate. In the ECHAM5_Trig model, the variance of virtual potential temperature must remain with the bound of a minimum (*minbuoy*) of 0.025 K and maximum of 1.0 K (*maxbuoy*). The minimum value of the variance of virtual potential temperature inadvertently governs the amount of low-level clouds. For example, a higher value of *minbuoy* implies convection is triggered more easily, allowing for increased mixing throughout the atmospheric column. This both dries out the boundary layer while distributing moisture throughout the column, thus producing fewer low-level clouds. Conversely, low values of *minbuoy* implies convection is suppressed, allowing moisture to build up in the boundary layer, conducive to low-level cloud cover conditions. For the purpose of this study, the cloud fraction in the present climate will be referred to as initial cloud cover. Experiments with small values of *minbuoy* have large cloud covers in the present climate; conversely, experiments with large values of *minbuoy* have little cloud covers in the present climate.

Figure 6.2 shows the cloud-climate feedbacks of seven perpetual July experiments with varying *minbuoy*. The values of *minbuoy* which are tested include: 0.0 K, 0.0025 K, 0.0125 K, 0.025 K, 0.125 K, 0.25 K, and 0.50 K.

The results of this study show that the cloud-climate feedback is indeed dependent on the value of *minbuoy*, and therefore the initial amount of low-level cloud cover the model produced, as proposed by Roeckner & Esch (2010). The low-level cloud cover corresponding to each of the sensitivity experiments are shown in Table 6.3.

Table 6.3— Cloud-climate feedbacks of seven perpetual July experiments with varying *minbuoy* [K] and their low-level cloud cover (%).

	minbuoy [K]						
	0.0	0.0025	0.0125	0.025	0.125	0.25	0.50
$\frac{\Delta CRF}{G}\|_{net}$ [W m^{-2}]	2.45	2.63	1.43	1.46	1.11	1.27	0.64
Present low cld. frac (%)	23.84	23.96	23.54	22.86	22.23	21.75	21.04
Perturbed low cld. frac (%)	21.54	21.81	21.38	21.03	20.37	19.83	19.15

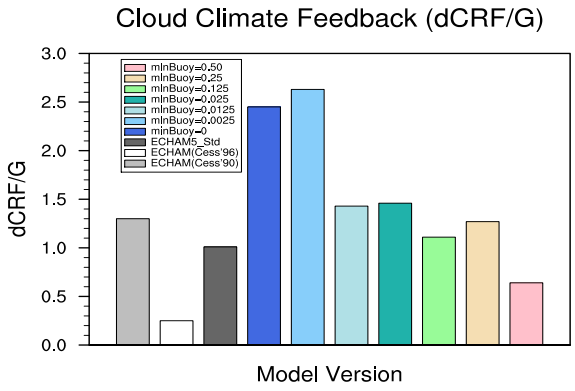

Figure 6.2— Perpetual July following Cess et al. (1990): Convective Trigger Sensitivity Experiment.

Not surprisingly, the perturbed climate experiments produced fewer clouds for all cases of *minbuoy* (Table 6.1). Since low-level clouds directly affect the CRF_{SW}, and thereby the ΔCRF/G, studying the changes in the CRF_{SW} between the present day and the perturbed climate scenario of each sensitivity experiment may shed light into the causes of the CCF spread. The CRF_{SW} in the warmer scenario is weaker than the present day; as expected due to the decrease in the low-level cloud amount (Fig. 6.3). The decrease in CRF_{SW}, however, is greater for high values of initial cloud cover than low values of initial cloud cover. The CRF_{SW} in turn is affected by both the area cover by low-level clouds and the type of boundary layer cloud. Thus, it will be important to look at the changes in low-level cloud cover in addition to the type of boundary layer clouds present.

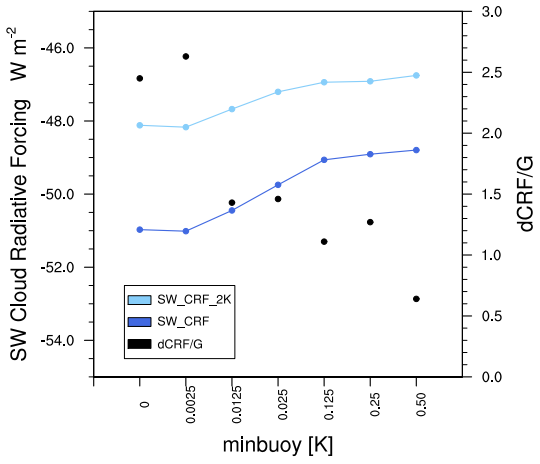

Figure 6.3— Cloud-climate feedback (black dots; scale on Right) for ECHAM5_Trig sensitivity under perpetual July conditions with contribution to short wave cloud radiative forcing (W m^{-2}) for the present (navy) and perturbed (blue) climate.

The low-level cloud fraction defined by pressure level and area of large-scale dynamical subsidence along with the cloud-climate feedbacks of each ECHAM5_Trig sensitivity ex-

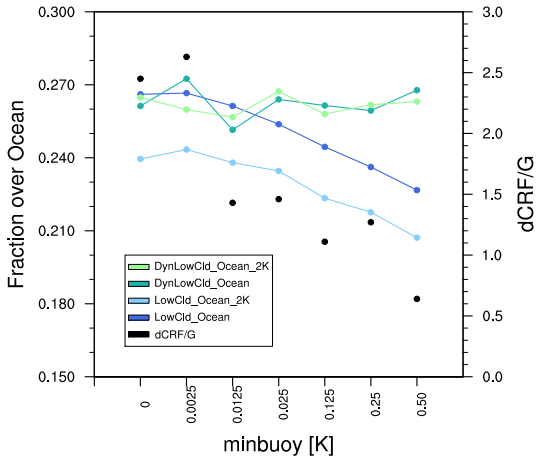

Figure 6.4— Cloud-climate feedback (black dots, scale on Right) for the ECHAM5_Trig sensitivity experiments under perpetual July conditions are presented alongside their corresponding fraction (scale on Left) of low-level clouds over the ocean (blue) and area of dynamical subsidence (green) for the present (dark colors) and perturbed climate (light colors).

periment are shown in Fig. 6.4. The low-level cloud cover show a distinct decrease in cloud cover in the warmer climate and corresponds the decrease in outgoing CRF_{SW} radiation reflected seen in Fig. 6.3. Additionally, the more low-level clouds there are in the present climate, the greater the decrease in low-level clouds. This may be because cloud cover is bounded from below (i.e. can not be less than zero). If in an idealized example, the cloud cover was to decrease by 0.3 in a warmer climate, then the present day scenario with more cloud cover (e.g. 0.4) would decrease by 0.3 to 0.1, whereas a present the present day climate with fewer clouds (e.g. 0.2) would decrease by 0.2 to 0. Thus, the scenario with greater cloud cover would decrease more than one with fewer clouds.

Studying the areas of large-scale subsidence, however, indicates very little change between the present day and perturbed climate. This implies the area covered by large-scale subsidence does not change. Nonetheless, within the subsidence area partitioning between stratocumulus and shallow cumulus regimes does change much. The area covered by shallow cumulus clouds decreases whilst the area covered by stratocumulus clouds increases in a warmer climate (Fig. 6.5). Since these two cloud regimes are defined dynamically, this implies the atmosphere in a warmer climate is more stable, i.e. the upper atmosphere temperature changes faster than the lower atmosphere. This can be explained by the lapse rate feedback. In the present day climate, the temperature profile in the lower troposphere follows the moist adiabat, which transitions to the dry adiabat as it nears the upper troposphere. In a warmer climate, the temperature profile of the lower troposphere continues to follow the moist adiabat, however, an increase in moisture transported into the upper troposphere implies the temperature profile follows the moist adiabat higher into the atmosphere. Thus, the temperature change is greater for the upper troposphere

than the lower troposphere. This leads to a more stable atmosphere (LTS) and hence less mixing of the boundary layer, providing ideal conditions for stratocumulus cloud cover.

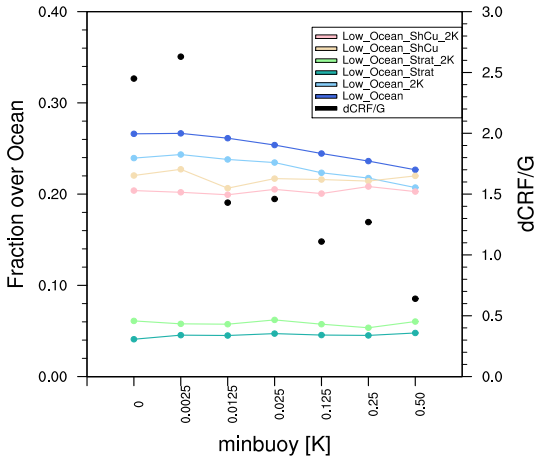

Figure 6.5— Cloud-climate feedback (Right, black dots) for the ECHAM5_Trig sensitivity experiments under perpetual July conditions are presented with the area cover by dynamically defined stratocumulus (present-day: dark green, warmer climate: light green) and shallow cumulus (present-day: orange, warmer climate: pink) cloud regimes (Left).

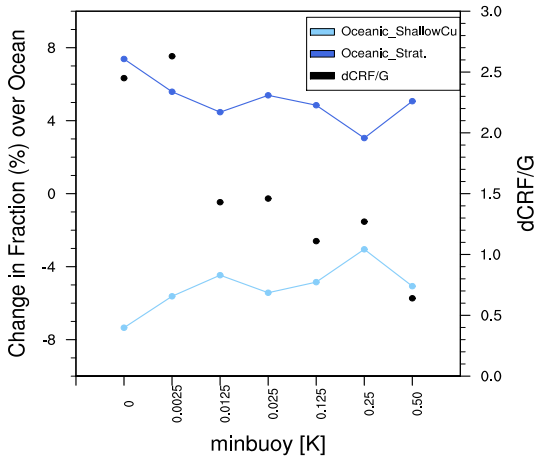

Figure 6.6— Relative change to the area (Left scale) of dynamically defined stratocumulus (dark blue) and shallow cumulus (light blue) regimes over the ocean with their cloud-climate feedbacks (black, Right scale) under perpetual July conditions.

Fig. 6.6 shows the relative change to the areas covered by stratocumulus and shallow cumulus in the warmer climate. There does not appear to be a relationship between relative change in area, for either stratocumulus or shallow cumulus, and cloud-climate feedbacks. Nor does there appear to be a correlation between the changes in stratocumulus or shallow cumulus cloud area with respect to initial cloud fraction.

The spread amongst the cloud-climate feedback parameters of the three boundary layer

schemes, presented in the previous section (Fig. 6.1), is encapsulated within the ′extremes′ of the ECHAM5_Trig cloud-climate feedback sensitivity experiments. The cloud-climate feedback parameters in ECHAM5_Trig range from 2.63 to 0.64 though the low-level cloud cover has difference of less than 3 %. This exceeds the cloud-climate feedback range of -0.5 to 2 presented in Cess et al. (1996).

If the initial amount of cloud cover affects the cloud-climate feedback, then the conclusions regarding cloud-climate feedbacks to date may be misleading. Many of the current versions of the 19 GCMs presented in Cess et al. (1996) underestimate the amount of low-level clouds (Chepfer et al., 2009), which would imply the cloud-climate feedbacks of these models may have been underestimated as well. If the amount of boundary layer clouds in these GCMs was to increase, then the ECHAM5_Trig experiments would imply that the cloud-climate feedback parameter of the models would increase. Simply put any model with a boundary layer parameterization scheme which produces an abundance of clouds likely has a high cloud-climate feedback parameter.

In the future, it may be useful to determine whether the frequency of convection, itself, has an impact on the cloud-climate-feedback. This study demonstrates that the frequency, in the ECHAM5_Trig, is directly correlated with the cloud-climate feedback parameter (Table 6.3). It was shown that the more often convection is called, the lower the cloud-climate feedback. If this holds true for other schemes then boundary layer parameterizations with a high frequency of convection will have a lower present day low-level cloud cover and thus a lower cloud-climate feedback. Conversely, a boundary layer parameterization with a low frequency of convection produces a large amount low-level clouds will have a high cloud-climate feedback. Further study of this is needed.

Summary

The cloud-climate feedback experiments using the ECHAM5_Trig parameterization shows that cloud-climate feedbacks are related to the frequency of convection, and thereby the amount of present day low-level clouds. The greater the low-level cloud cover in the present climate, the greater the cloud-climate feedback. The relationship between low-level cloud amount and cloud-climate feedback is related to the fact that low-level cloud cover decreased more in the experiments with higher present day low-cloud cover than those with fewer present day low-cloud cover in a warmer climate.

Unlike the low-level cloud fraction, which decreases in a warmer climate, the area covered by subsidence remained the same in warmer climate. Within the subsidence area, however, the partioning between shallow cumulus and stratocumulus cloud regimes did change somewhat. For all experiments, the area covered by the stratocumulus cloud regime increases whereas the area of shallow cumulus decreases. This implies that in a warmer climate, the stability of the atmosphere increases. There was no systematic difference in

stabilization of the atmosphere with cloud-climate feedbacks were found.

6.4 Outlook: Application of Satellite Simulators

In the future, it would be interesting to determine whether the quality with which a given scheme represents the present climate and its variability, using a metric from the CALIPSO and CloudSat satellite retrievals, can be used to constrain cloud-climate-feedbacks.

If we were to attempt to identify a property from the ECHAM5 experiments performed to date, then the amount of low-level clouds would be best as a starting point. This could be used along with the lidar simulator cloud fraction maps, which identify the projected cloud cover, similar to the one the radiation scheme uses. This would help identify parameterizations which most resemble satellite retrievals. Though it may be said that if the model looks more like the observations then there is likely going to be higher cloud-climate feedbacks. In regards to the radar simulator, the radar reflectivity histograms may be useful in identifying schemes which produce the greatest frequency of non-precipitating boundary layer clouds. Of course, one must be aware that the precipitation frequency, which is often overestimated in GCMs, may obscure the boundary layer clouds in some situations.

6.5 Conclusions

In this chapter the cloud-climate feedbacks of three different boundary layer schemes are compared. The ECHAM5_Std, ECHAM5_Trig and ECHAM5_VSMF boundary layer schemes were run in an idealized climate change experiment. All three schemes have a positive cloud-climate feedback parameter, which according to Cess et al. (1996) have high-sensitivities amplifying the surface warming. The three schemes show rather similar values of cloud-climate feedbacks, which is not surprising considering that the three schemes showed similar cloud distributions as discussed in the previous chapter. Thus, the cloud-climate feedbacks show very little spread.

In order to better understand the sensitivity of cloud-climate feedbacks to cloud amount, a single scheme was studied. The ECHAM5_Trig was selected and its cloud cover varied. By governing the frequency of convection, several scenarios were produced in which the low-level cloud cover varied. By allowing convection to occur frequently, several scenarios were produced in which few low-clouds existed. Conversely, convection was suppressed to produce several scenarios where many low-level clouds existed. These scenarios were run in perturbed climate experiments, and their results suggest that the cloud-climate feedback is related to the present day cloud cover. Experiments with fewer present day low-level clouds had lower cloud-climate feedbacks than those with a higher

present day low-level cloud cover.

If this conclusion holds true for all GCMS, then those GCMs which employ parameterizations yielding few low-level clouds have low cloud-climate feedbacks. This would also imply that estimates of cloud-climate feedbacks to date are likely underestimated as many GCMs underestimate the low-level cloud cover.

Further study of the low-level clouds demonstrated that identification of low-level cloud regimes by large-scale dynamical subsidence, specifically the vertical velocity, is insufficient. Often times, higher-level clouds are captured along with low-level clouds, the evidence is in the fact that the area covered by large-scale subsidence did not decrease in the warmer climate although the low-level cloud cover did. This is also supported by the radar reflectivity histograms shown in Chp. 4.7. Using the dynamical division of vertical velocity at 500 and 700 hPa alone proved to be an insufficient measure, however, using it along with the LTS criterion was shown to be much better. Within the subsiding area, the results show that the area covered by dynamically defined stratocumulus clouds increases in a warmer climate, whereas the area covered by dynamically defined shallow cumulus decreases. This means that in a warmer climate, the atmosphere is more stable. The variability in the dynamically defined cloud fractions, however, were found to be unrelated to the cloud-climate feedbacks.

Chapter 7

Conclusions and Outlook

7.1 Summary and Conclusions

This thesis assesses the representation of clouds and precipitation in the ECHAM5 GCM using CALIPSO and CloudSat satellite retrievals for the purposes of better understanding cloud-climate feedbacks. This study is the first to make use of active space-borne lidar and radar measurements, as well as their simulators, in the evaluation of ECHAM5. The aim is to identify model weaknesses, particularly regarding the boundary layer, using the active instruments which allow for the vertical distribution of clouds and their properties in ECHAM5 to be evaluated against global observations. Three new shallow convection schemes in ECHAM5 are compared to observations. The influence of the schemes on simulated cloud-climate feedbacks is then investigated.

In order to compare CALIPSO and CloudSat satellite retrievals with ECHAM5, the Cloud Feedback Model Intercomparison Project's CALIPSO and CloudSat simulators have been implemented. This allows us to account for retrieval attributes, such as instrument sensitivity and sampling techniques. Satellite simulators enable a direct comparison between satellite retrievals and model output by using the same definition for clouds.

The thesis is divided into three sections, each of which addresses the following questions:

- How well does ECHAM5 represent clouds and precipitation in the present climate?
- How do different representations of boundary layer clouds in the ECHAM5 GCM improve the present cloud and precipitation distributions?
- How do cloud-climate feedbacks differ due to different representations of low-level clouds?

7.1.1 How well does ECHAM5 represent clouds and precipitation in the present climate?

The evaluation of ECHAM5 using the CALIPSO and CloudSat satellite retrievals initially required two forms of analysis: (i) between the model and the satellite simulator output; and (ii) between the satellite simulator and satellite retrievals. This allowed us to identify model features which intrinsically limit the lidar and radar simulators.

The high, mid and low-level cloud cover maps from the lidar simulator indicate that ECHAM5 captures large-scale features well. For example, the geographical distribution of high-level clouds and cloud characteristics associated with the Hadley circulation. High-level cloud cover, however, is overestimated, particularly the most optically thin ones. In regards to the mid- and low-level clouds, the ECHAM5 model significantly underestimates the mid-level clouds and (Sub)Tropical low-level clouds. The low-level clouds which are produced are optically too thick. These features can be seen in the zonal hydrometeor fraction of both the lidar and radar simulator. The overestimation of high-level clouds attenuates the lidar signal prematurely high in the atmosphere limiting the amount of clouds detected at lower levels. The lidar scattering ratio histograms demonstrated that attenuation of the lidar was exacerbated by an underestimation of the ice crystal effective radius, which lead to significantly larger scattering ratios for a given ice crystal content. The underestimation of the ice crystal effective radius also rendered high-clouds undetectable to the radar simulator, which are too low in atmosphere compared to the observations.

The zonal hydrometeor fraction derived by the radar simulator indicates that the hydrometeor fraction in the Tropics and in the boundary layer are overestimated. The overestimation can be attributed to precipitation. This was demonstrated by the radar reflectivity histograms. From the histograms it could also be inferred that the frequency of precipitation is too high and the intensity too low. The overestimation in precipitation frequency is mainly due to large-scale rather than convective precipitation. The continuous presence of precipitation implies that there are large precipitation particles in the atmosphere, dominating the radar reflectivity.

Studying the radar reflectivity histograms has demonstrated that identifying boundary layer clouds according to the large-scale subsidence is inadequate. It was shown that even in areas of strong subsidence, often higher-level clouds exist and are captured by the radar. Only when large-scale dynamics are used in conjunction with geographical sub-sampling is there fruitful identification low-level cloud regimes. Furthermore, the lower-tropospheric stability criterion is insufficient for clearly separating stratocumulus and shallow cumulus clouds in the satellite retrievals.

In conclusion, in order for ECHAM5 to capture the present climate and its variability better, the representation of high-level clouds and the convection scheme need to be improved. The projected distribution of high-level clouds needs to be maintained, yet its

reflectivity reduced. Additionally, the assumed ice crystal effective radius should be doubled. In regards to the boundary layer, the frequency of precipitation must be decreased in ECHAM5 while increasing cloud cover substantially, particularly over the (Sub)Tropical oceans. The cloud optical thickness of the boundary layer clouds should be reduced to maintain the shortwave cloud radiative effects.

7.1.2 How do different representations of boundary layer clouds in the ECHAM5 GCM improve the present cloud and precipitation distributions?

It was shown that in comparison to both the ISCCP and CALIPSO satellite retrievals the ECHAM5 GCM underestimates low-level clouds; particularly in the (Sub)Tropics. Previous studies identified marine boundary clouds as being the main source of uncertainties in Tropical cloud-climate feedbacks (e.g. Bony & Dufresne, 2005). The more models poorly represent cloud distributions in present-day simulations, the less confidence we have in the model to predict the distribution of clouds in the perturbed climate (e.g. Webb et al., 2001).

As such, three new boundary layers schemes were incorporated into the ECHAM5 GCM and evaluated against both the standard model and the CALIPSO and CloudSat retrievals. These schemes include a modified version of the Tiedtke (1989) scheme (ECHAM5_Trig); a bulk parameterization of transient shallow cumulus clouds (ECHAM5_VSMF); and a dual mass flux scheme (ECHAM5_DMF). This study focused on the distribution of clouds from 45 °N to 45 °S and within the Hawaiian stratocumulus and California shallow cumulus regions.

A comparison of the purely modelled cloud maps with ECHAM5_Std showed that the high- and mid-level clouds of the three schemes changed very little compared to the standard scheme. The three new schemes, however, improved the low-level cloud cover, particularly over the oceans. Much of the changes to the low-level cloud cover in the ECHAM5_Trig and ECHAM5_VSMF models, though, was not captured lidar simulator. This is especially true where there are few low-level clouds. This implies that many of the changes to the low-level cloud cover occur below high-level clouds or that the clouds are optically thin. In regards to the preliminary version of ECHAM5_DMF, the low-level cloud cover increased significantly and the lidar simulator was able to capture most of the changes. In spite of having the greatest amount of low-level clouds, even the ECHAM5_DMF underestimates the low-level cloud cover compared to the retrievals.

The study of the three models over the Californian stratocumulus and Hawaiian shallow cumulus cloud regimes using the radar reflectivity histograms demonstrated that the distribution of clouds and precipitation are very different amongst the schemes, despite having similar projected cloud covers. The radar reflectivity histograms also show that

the new boundary schemes increased the frequency of occurrence of high-level clouds in the ECHAM5_Trig and ECHAM5_VSMF models in these regions. This is likely due to convection stemming from a moister boundary layer and the Tiedtke (1989) convection scheme overestimating the convective mass-flux.

The radar reflectivity histograms demonstrate that the precipitation frequency continues to be overestimated in all versions of the ECHAM5 model. Further study of the precipitation in the ECHAM5_Trig, ECHAM5_VSMF and ECHAM5_DMF indicates that the overestimation in precipitation frequency stems from different partitioning of large-scale and convection precipitation and of differing intensities. Regardless of the overestimation in precipitation frequency, all schemes improve the frequency of large-scale precipitation by decreasing the number of low-intensity events and increasing in higher intensity events. The convective precipitation showed no systematic change amongst the schemes.

The boundary layer clouds in the ECHAM5_Trig, ECHAM5_VSMF and to some extent the ECHAM5_DMF are not evident in the stratocumulus and shallow cumulus radar reflectivity histograms. In these regions, the overestimation of precipitation frequency is not likely the reason non-precipitating boundary layer clouds are not detected, but rather it is likely the clouds produced by the new schemes are optically too thin. Of all the schemes, only the preliminary version of the ECHAM5_DMF produces non-precipitating clouds throughout the boundary layer and at higher altitudes, in better agreement with CloudSat.

In conclusion, all three boundary layer schemes improve the representation of low-level clouds. The differences amongst the schemes, however, are less than those compared to the satellite retrievals. The preliminary version of the ECHAM5_DMF shows the most promise in producing non-precipitating boundary layer clouds. With its modified transport scheme, the ECHAM5_DMF does not appear to overestimate precipitation to the same extent as in the other models.

7.1.3 How do cloud-climate feedbacks differ due to different representations of low-level clouds?

The ECHAM5_Std, ECHAM5_Trig and ECHAM5_VSMF boundary layer schemes were run in an idealized climate change experiment. The preliminary version of ECHAM5_DMF was excluded from this experiment as the boundary layer scheme was not yet coupled to the radiation scheme. The comparison of the ECHAM5_Std, ECHAM5_Trig and ECHAM5_VSMF cloud-climate feedbacks show that all three models have positive cloud-climate feedback parameters; whose amplitudes fall within the high-sensitivity range according to Cess et al. (1996). This implies a strong amplification of the surface warming.

The three models have similar values of cloud-climate feedbacks which is related to the fact that the ECHAM5_Std, ECHAM5_Trig and ECHAM5_VSMF models all have a

similar cloud distributions. The variation in cloud-climate feedbacks can be traced back to differences in the $CRF|_{SW}$ which suggested the properties of low-level clouds differ.

To better understand the sensitivity of cloud-climate feedbacks to low-level clouds, the ECHAM5_Trig model was selected for a sensitivity study. The low-level cloud cover was varied by governing the frequency of convection. The results suggest that cloud-climate feedbacks are related to the present day cloud cover. Experiments with fewer present day low-level clouds had lower cloud-climate feedbacks, whereas experiments with a greater amount of present day low-level cloud cover had higher cloud-climate feedbacks.

Should this conclusion hold true for all GCMS, then estimates of cloud-climate feedbacks to date are likely underestimated as many GCMs underestimate the low-level cloud cover. As the representation of boundary layer clouds improve, the increase in low-level cloud cover will likely increase cloud-climate feedbacks.

Studying the low-level clouds in the idealized climate scenario has also demonstrated that in a warmer climate, within the area of dynamical subsidence, the dynamically defined area covered by stratocumulus clouds increases, whereas the shallow cumulus area decreases. This is because the atmosphere in the warmer climate is more stable. This shift, though, is not correlated with the simulated cloud-climate feedbacks. The change in cloud types, with differing radiative properties, adds to the fact that the overall low-level cloud cover decreases.

In conclusion the cloud-climate feedbacks of the different boundary layer schemes in ECHAM5 showed little variability yet high-sensitivity. If the amount of boundary layer clouds are indeed correlated with the cloud-climate feedback parameter, improvement of low-level clouds in GCMs will increase the sensitivity of cloud-climate feedbacks.

7.2 Outlook

In the immediate future, the implementation of ECHAM5_DMF will be finalized to include the coupled cloud and radiation scheme. The ECHAM5_DMF will then be evaluated using the lidar and radar simulators and run within the cloud-climate feedback experiment. The magnitude of the ECHAM5_DMF cloud-climate feedback parameter will provide valuable insight into whether different boundary layer schemes in a single model have wide range of feedback strengths. In addition, the experiment will also shed light on whether the there is indeed a relationship between the amount of low-level cloud cover in the present climate and cloud-climate feedbacks. Compared to the ECHAM5_Trig and ECHAM5_VSMF models, the ECHAM5_DMF produced the largest differences in projected low-level cloud cover compared to the ECHAM5_Std model. Many of the newly formed clouds in the ECHAM5_DMF model were also detected by the lidar simulator, and it will be interesting to determine whether the cloud fraction derived by the lidar simulator can be used to

constrain cloud-climate feedbacks.

This study has identified some key issues in ECHAM5 which must be addressed; including increasing the effective radius of ice crystals. It would be interesting to determine whether the increased ice crystal size will reduce the amount of optically thin clouds, those with $\tau < 0.03$, allowing for the lidar simulator to detect more high-level clouds; as well as, determine if the increased particle size will improve the high-level cloud amount by increasing the sedimentation and aggregation rate, precipitating out the highest-level clouds. It will also reduce the scattering ratio of the highest-level clouds so that the lidar can penetrate further into the atmosphere.

In a similar manner, the effective radius of liquid water particles should be evaluated. The lowest-level clouds all have very large lidar scattering ratios, which may be artificially large for a given water content if the effective radius is underestimated. It would be of interest to determine whether the low-level clouds have underestimated effective radii for liquid water particles or if the low-level clouds are optically too thick because of too large in-cloud water and ice contents. For that purpose it may be of interest to use the PARASOL satellite retrievals, with its simulator, which would allow for the reflectances (i.e. albedo) of ECHAM5's clouds to be compared with observations (refer to Appendix A). The reflectances will allow one to determine if the ratio of cloud water content to total cloud cover of ECHAM5's clouds are reasonable. It might be useful to investigate the influence of sub-grid variability the optical thickness of clouds.

Since the cloud water content is closely tied to the precipitation scheme in a model, it may be interesting to use the radar simulator to evaluate various precipitation schemes; including different large-scale and convection parameterizations. The convection scheme, as we have seen in ECHAM5, currently transports an excessive amount of moisture high into the atmosphere. The frequency of convection should also be studied in regards to cloud-climate feedbacks. As we saw in Chp. 6.3, the greater the frequency of convection in ECHAM5_Trig, the greater the cloud-climate feedback.

While active satellites are the best platforms we have to date which provide global coverage of the boundary layer, they were not specifically designed to support boundary layer science. In the future, measurements of the thermodynamic structure (e.g. temperature and water content) in the sub-cloud layer will be valuable. Only improvement of modelling strong gradients (i.e. in temperature and water) as well as turbulent structures will help us address the uncertainty in cloud-climate feedbacks.

List of Figures

3.1 A-Train constellation of Earth-observing satellites. 11
3.2 Schematic of Lidar Scattering Ratio Histogram. 13
3.3 Map of Regional Cloud Regimes 14
3.4 CloudSat cloud masking algorithm (Marchand et al., 2008). 16
3.5 ISCCP cloud classification histogram (Rossow & Schiffer, 1999). 17
3.6 SCOPS 19

4.1 High, mid, and low-level cloud cover maps 31
4.2 Zonal Hydrometeor Fraction: Lidar and Radar 32
4.3 Attenuation Frequency 33
4.4 Lidar Histograms: Cloud Regimes 36
4.5 Lidar Histograms: Sensitivity Experiments 41
4.6 Modelled cloud profile over California & Hawaii 41
4.7 Cloud fraction frequency of Sub-Tropics 42
4.8 Zonal Hydrometeor Fraction: Sensitivity Experiments 43
4.9 Radar Histograms: Cloud Regimes 45
4.10 Precipitation Rates 45
4.11 Radar Histograms: Contribution by precipitation 50
4.12 Radar Histogram: Convective contribution 50
4.13 Dynamical Cloud Masks 52
4.14 Radar reflectivity histograms: Dynamical Regimes 53

5.1 Life cycle of shallow cumulus cloud 59
5.2 Dual mass flux schematic 61
5.3 Cloud cover maps: Model Only 62
5.4 Comparison of zonal cloud cover 66
5.5 Comparison of zonal cloud cover as seen by lidar 69
5.6 Cloud cover maps: Model with simulator 71
5.7 Radar reflectivity histograms: Scheme comparison 72

5.8 Regional cloud fraction profiles 75
5.9 Precipitation frequency of schemes 77

6.1 Cloud-Climate Feedbacks: Comparison of schemes 82
6.2 Cloud Climate Feedbacks: Sensitivity Experiment 85
6.3 CCF: Sensitivity of CRF_{SW} 85
6.4 CCF: Area of dynamical subsidence 86
6.5 CCF: Stratocumulus and Shallow cumulus cloud regimes 87
6.6 CCF: Change in areas of Stratocumulus and Shallow cumulus cloud 87

A.1 PARASOL reflectivity 102
A.2 Joint reflectivity-cloud cover histograms: Daily 103
A.3 Frequency of occurrence of cloud cover: Daily 103
A.4 Joint reflectivity-cloud cover histograms: Monthly 104
A.5 Frequency of occurrence of cloud cover: Monthly 104

List of Tables

4.1 Global Cloud Cover 26
4.2 Regional Precipitation Rates 45

5.1 Global Cloud Radiative Forcing 67
5.2 Global Cloud Radiative Forcing: Area of dynamical subsidence 67

6.1 Cloud-Climate Feedbacks & Cloud Cover 82
6.2 Cloud-Climate Feedbacks & Area of Dynamical Subsidence 83
6.3 Cloud-Climate Feedbacks: Sensitivity Study 84

Appendix A

Parasol

A.1 PARASOL Retrievals and Simulator

As seen in Chp. 4.3, clouds in ECHAM5 produce large scattering ratios in the lidar joint cloud altitude-scattering ratio histograms, which is akin to optical thickness. In order to study the clouds more closely, the reflectances from the PARASOL satellite and satellite simulator will be compared. The cloud reflectivity is analogous to albedo, may allow us to understand the optical properties of cloud in ECHAM5. This study will compare the PARASOL retrieved reflectances for JJA 2007 with those simulated using the COSP-v1.2.1 PARASOL simulator in ECHAM5.

The PARASOL (Polarization and Anisotropy of Reflectance for Atmospheric Sciences coupled with Observations from a Lidar) satellite measures the solar radiation reflected by the Earth using the POLDER (Polarization and Directionality of the Earth's Reflectances) sensor. As part of the A-train constellation from December, 2004 to December, 2009, the passive POLDER radiometer retrieved polarized, multi-directional reflectances using a wide field camera with 16 spectral bands. These bands range from 443 nm to 1020 nm and include polarized filters. The retrieved POLDER satellite products include the cloud amount, cloud pressure, cloud optical thickness, cloud albedo and cloud thermodynamic phase (Parol et al., 2003).

The PARASOL simulator takes the model-simulated profiles of cloud water and cloud fraction for each sub-column within a grid box from the lidar simulator, in the form of liquid and ice water cloud optical thickness. The optical thickness is then used in a look-up table to determine a PARASOL reflectance.

A.1.1 PARASOL Reflectivity Maps

The global maps of PARASOL reflectivity are presented in Fig. A.1. Note that the PARASOL satellite does not obtain retrievals for the Southern Hemisphere high latitudes, which lies in polar night during JJA, hence unable to reflect sunlight. The satellite re-

trievals show the largest reflectivities in the high latitudes and smallest reflectivities over the Subtropical oceans, though low-level stratocumulus clouds, for example off the coast of South America, have a local maximum.

In comparison to the satellite retrievals, ECHAM5 shows an overestimation in the reflectivities of clouds in the ITCZ and polar regions, and an underestimation in the reflectivities over the Subtropical oceans and stratocumulus regions. The latter comes as no surprise as there are few clouds modelled over the Subtropical oceans, and as such there is a low liquid water content. Similarly, the area covered by stratocumulus clouds are underestimated in ECHAM5 and has a low liquid water content. Over the ITCZ, the high reflectivities seen in ECHAM5 are likely the result of the underestimated effective ice crystal radius, described in Chp. 4.4, which artificially increases the clouds optical thickness, and in turn the reflectance. In the polar regions, however, the reflectance of clouds in ECHAM5 is underestimated. This implies the polar clouds in ECHAM5 are not optically thick enough.

The reflectivities of these maps can be used in conjunction with the CALIPSO total cloud cover to produce the joint reflectivity-cloud cover histograms in the following section.

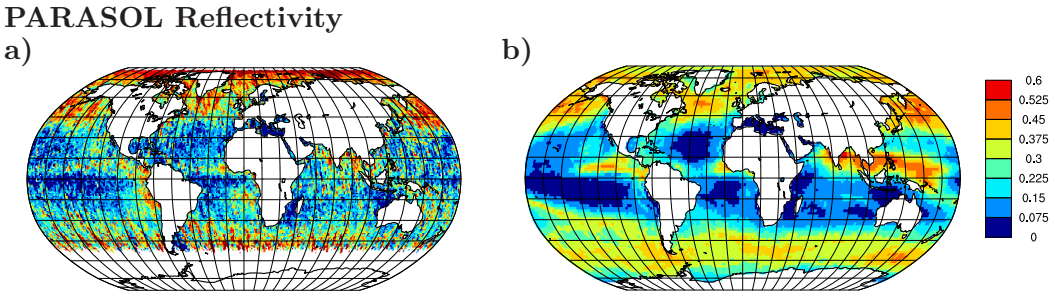

Figure A.1— PARASOL reflectivity for JJA 2007. (a) PARASOL satellite retrieval; (b) ECHAM5 with PARASOL Simulator.

A.1.2 Joint Reflectivity-Cloud Cover Histograms

The joint histograms of PARASOL reflectivity and its corresponding CALIPSO total cloud cover for JJA 2007 are determined from daily values and monthly means. The study composed from the different means show how ECHAM5 captures the relationship between optical thickness and cloud cover, useful for the study of cloud feedbacks. In each figure the histograms are created from the PARASOL and CALIPSO satellite retrievals and satellite simulator are shown. It should be noted that satellite retrievals for PARASOL were only available for 63 days within JJA 2007 period.

The joint reflectivity-cloud cover histogram composed from daily (i.e. at 15:00 hr UTC) averages is roughly bimodal, which can divided by low cloud covers (< 0.4) and high cloud

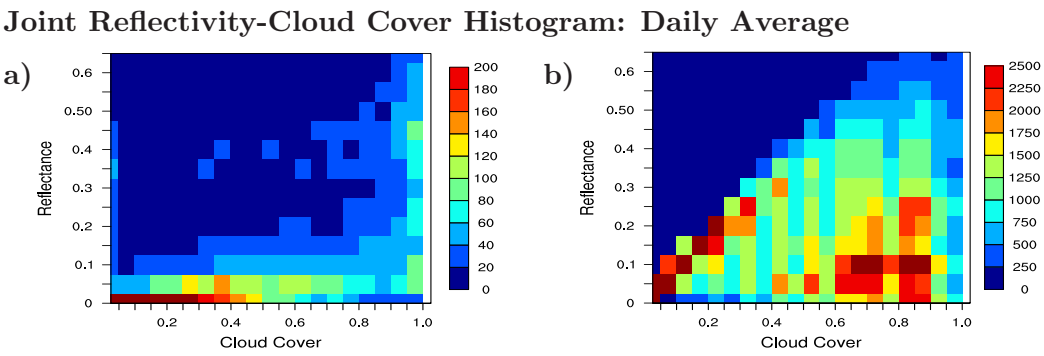

Figure A.2— Joint reflectivity-cloud cover histograms for JJA 2007 composed from daily averages. (a) Satellite retrievals of PARASOL reflectivity and CALIPSO total cloud cover; (b) ECHAM5 with PARASOL simulator reflectivities and CALIPSO simulator total cloud cover.

covers (≥ 0.4) (Fig. A.2a). The majority of reflectivities for the low cloud covers are less than 0.05 because CALIPSO, as previously mentioned, is sensitive to high-level optically thin clouds. These clouds have a very small effect on the reflected short-wave radiation detected by PARASOL, thus the reflectance is close to the background albedo of the ocean surface (~ 0.05). Areas with high cloud covers have a greater distribution of reflectivities.

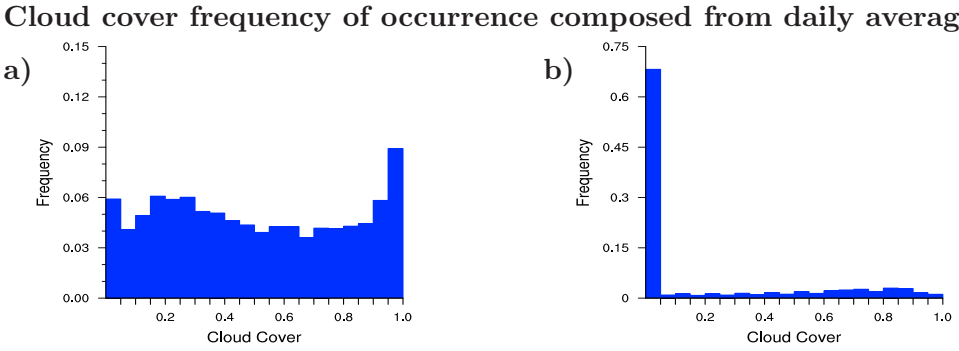

Figure A.3— Frequency of occurrence of cloud cover for JJA 2007 composed from daily averages. (a) Satellite retrievals of CALIPSO total cloud cover; (b) ECHAM5 with CALIPSO simulated total cloud cover.

The distribution of reflectivities in ECHAM5 are greater than those observed for all cloud covers. The fact that low cloud covers have relatively large reflectivities obtained by the PARASOL simulator, implies the clouds modelled in ECHAM5 are optically thicker than observed. The optical thickness stems from the total cloud liquid and ice water per cloud cover. This would imply that ECHAM5 overestimates the cloud water content per cloud cover. As such, the distribution of total cloud cover from JJA 2007, from both CALIPSO and ECHAM5, are plotted in Fig. A.3. Models have a hard time producing grid boxes with cloud covers of 1, as the grid box is so large the cloud cover is typically less than 1 at temporal averages (Fig. A.3b). As such, the seasonal mean composed from monthly averages are also compared (Fig. A.4).

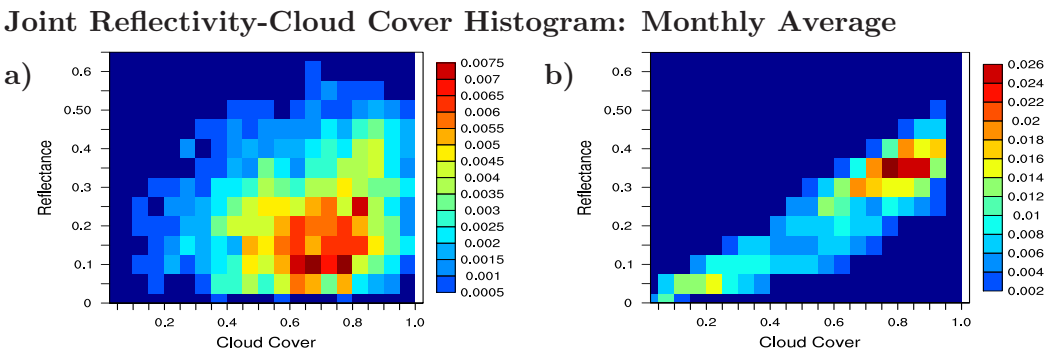

Figure A.4— Joint reflectivity-cloud cover histograms for JJA 2007 composed from monthly averages. (a) Satellite retrievals of PARASOL reflectivity and CALIPSO total cloud cover; (b) ECHAM5 with PARASOL simulator reflectivities and CALIPSO simulator total cloud cover.

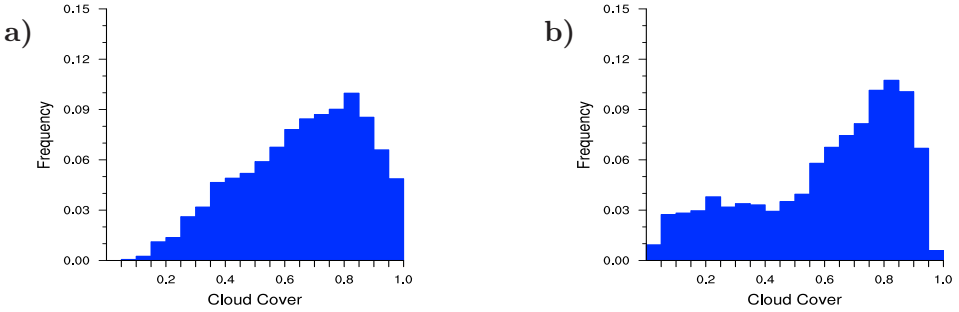

Figure A.5— Frequency of occurrence of cloud cover for JJA 2007 composed from monthly averages. (a) Satellite retrievals of CALIPSO total cloud cover; (b) ECHAM5 with CALIPSO simulated total cloud cover.

The joint reflectivity-cloud cover histograms composed from daily averages differ greatly from the monthly averaged ones. The seasonal PARASOL satellite retrievals no longer have many cloud covers less than 0.2 or equal to 1.0 (Fig. A.4)a. This is because it is unlikely that a pixel (gridbox) remains entire clear (or cloudy) for the entire month. The PARSOL satellite reflectances correspondingly become more variable as different cloud systems pass through an area having different water contents, thus different reflectivities. The PARASOL retrievals show a greater distribution of reflectivities compared to ECHAM5. This may be due to the frequency of occurrence of cloud cover (Fig. A.5). ECHAM5 has a greater frequency of occurrence of low cloud fractions than are seen in the CALIPSO cloud cover. This shift towards a greater frequency in higher cloud cover ranges (0.6 to 0.8) is also why a shift in the PARASOL peak frequency of occurrence towards the high cloud cover. The peak in PARASOL reflectances are around 0.1 to 0.2, which is much lower than the peak reflectances of 0.3 and 0.4 as seen in ECHAM5.

Bibliography

Battaglia, A. and Simmer, C. (2008). How does multiple scattering affect the space-borne w-band radar measurements at ranges close to and crossing the surface-range? *IEEE Trans. Geosci. Remote Sens.* **46(6)**, 16441651, doi:10.1109/TGRS.2008.916085.

Bodas-Salcedo, A., Webb, M. J., Brooks, M. E., Ringer, M. A., Williams, K. D., Milton, S. F., and R., W. D. (2008). Evaluating cloud systems in the met office global forecast model using simulated cloudsat radar reflectivities. *J. Geophys. Res.* **113**, doi:10.1029/2007JD009620.

Bony, S. and Dufresne, J. (2005). Marine boundary layer clouds at the heart of tropical cloud feedback uncertainties in climate models. *Geophys. Res. Lett.* **32**, L20806, doi:10.1029/2005GL023851.

Bony, S., Dufresne, J., LeTreut, H., Morcrette, J., and Senior, C. (2004). On dynamic and thermodynamic components of cloud changes. *Climate Dynamics* **22**, 7186.

Cess, R., Potter, G., Blanchet, J., Boer, G., Del Genio, A., Deque, M., Dymnikov, V., Galin, V., Gates, W., Ghan, S., Kiehl, J., Lacis, A., Le Treut, H., Li, Z.-X., Liang, X.-Z., McAvaney, B., Meleshko, V., Mitchell, J., Morcrette, J.-J., Randall, D., Rikus, L., Roeckner, E., Royer, J., Schlese, U., Sheinin, D., Slingo, A., Sokolov, A., Taylor, K., Washington, W., Wetherald, R., Yagai, I., and M.-H., Z. (1990). Intercomparison and interpretation of climate feedback processes in 19 atmospheric general circulation models. *J. Geophys. Res.* **95**, 16601–16615, doi:10.1029/JD095iD10p16601.

Cess, R., Potter, G., Blanchet, J., Boer, G., Ghan, S., Kiehl, J., Letreut, H., Li, Z., Liang, X., Mitchell, J., Morcrette, J., Randall, D., Riches, M., Roeckner, E., Schlese, U., Slingo, A., Taylor, K., Washington, W., Wetherald, R., and Yagai, I. (1989). Interpretation of cloud-climate feedbacks as produced by 14 atmospheric gerneral-circulation models. *Science* **245**, 513–516.

Cess, R. D., Zhang, M. H., Ingram, W. J., Potter, G. L., Alekseev, V., Barker, H. W., Cohen-Solal, E., Colman, R. A., Dazlich, D. A., Del Genio, A. D.,

Dix, M. R., Dymnikov, V., Esch, M., Fowler, L. D., Fraser, J. R., Galin, V., Gates, W. L., Hack, J. J., Kiehl, J. T., Le Treut, H., Lo, K. K.-W., McAvaney, B. J., Meleshko, V. P., Morcrette, J.-J., Randall, D. A., Roeckner, E., Royer, J.-F., Schlesinger, M. E., Sporyshev, P. V., Timbal, B., Volodin, E. M., Taylor, K. E., Wang, W., and Wetherald, R. T. (1996). Cloud feedback in atmospheric general circulation models: An update. *J. Geophys. Res.* **101(D8)**, 79112,794, doi:10.1029/96JD00822.

Chen, T. and Rossow, W. (2002). Determination of top-of-atmosphere longwave radiative fluxes: A comparison between two approaches using scarab data. *J. Geophys. Res.* **107**, ACL 6–(1–13). NO. D8, 4070, 10.1029/2001JD000914.

Chepfer, H., Bony, S., Cesana, G., Dufresne, J., Konsta, D., Winker, D., Tanr, D., Nam, C., Zhang, Y., Klein, S., Cole, J., and Bodas-Salcedo, A. (2009). Evaluation of cloudiness simulated by climate models using calipso and parasol. In *Joint CALIPSO-CloudSat Science Team Meeting*.

Chepfer, H., Bony, S., Winker, D., Cesana, G., Dufresne, J., Minnis, P., Stubenrauch, C., and Zeng, S. (2010). The gcm oriented calipso cloud product (calipso-goccp). *J. Geophys. Res.* **115, D00H16**, doi:10.1029/2009JD012251.

Chepfer, H., Bony, S., Winker, D., Chiriaco, M., Dufresne, J., and Sèze, G. (2008). Use of calipso lidar observations to evaluate the cloudiness simulated by a climate model. *Geophys. Res. Lett.* **35**, L15704, doi:10.1029/2008GL034207.

Collis, R. and Russell, P. (1976). *Laser Monitoring of the Atmopshere: Lidar Measurement of Paricles and Gases by Elastic Backscattering of Differential Absorption*. Hinkley, E. Ed. Springer-Verlag.

Dai, A. (2006). Precipitation characteristics in eighteen coupled climate models. *J. Climate* **19**, 46054630.

Frisch, S., Shupe, M., Djalalova, I., Feingold, G., and Poellot, M. (2002). The retrieval of stratus cloud droplet effective radius with cloud radars. *J. Atmospheric and Oceanic Technology* **19**, 835–842.

Gehlot, S. (2010). *Feedbacks between convection and climate: Analysis with global modeling and satellite observations*. Ph.D. thesis, University of Hamburg, Germany Department Geowissenschaften.

Grant, A. (2001). Cloud-base fluxes in the cumulus-capped boundary layer. *Quart. J. Roy. Meteor. Soc.* **127**, 407421.

Hagemann, S., Arpe, K., and Roeckner, E. (2006). Evaluation of the hydrological cycle in the echam5 model. *J. Climate* **19**, 3810–3827.

Harrison, E., Minnis, P., Barkstrom, B., Ramanathan, V., Cess, R., and Gibson, G. (1990). Seasonal variation of cloud radiative forcing derived from the earth radiation budget experiment. *J. Geophys. Res.* **95**, 18 68718 703.

Hartmann, D., Ockert-Bell, M., and Michelsen, M. (1992). The effect of cloud type on earths energy balance: Global analysis. *J. Climate* **5**, 12811304.

Haynes, J. (2007). Quickbeam radar simulation software users guide v 1.1a. *Colorado State University Department of Atmospheric Science Fort Collins, CO, USA* **1**, 1–18.

Haynes, J., Marchand, R., Luo, Z., Bodas-Salcedo, A., and Stephens, G. (2007). A multipurpose radar simulation package: Quickbeam. *Bull. Amer. Meteor. Soc.* **88**, 17231727.

Hogan, R. J. and Illingworth, A. J. (2000). Deriving cloud overlap statistics from radar. *Quart. J. Roy. Meteo. Soc.* **126(569A)**, 2903–2909R.

Isotta, F. A. (2010). *Shallow cumulus clouds parameterization in the climate model ECHAM5-HAM.*. Ph.D. thesis, Diss., Eidgenssische Technische Hochschule ETH Zurich, Nr. 18881. doi:10.3929/ethz-a-006027106.

Karlsson, J., Svensson, G., and Rodhe, H. (2008). Cloud radiative forcing of subtropical low level clouds in global models. *Climate Dynamics* **30**, 779–788, DOI: 10.1007/s00382–007–0322–1.

Klein, S. and Hartmann, D. L. (1993). The seasonal cycle of low stratiform clouds. *J. Climate* **6**, 1588–1606.

Klein, S. and Jakob, C. (1999). Validation and sensitivities of frontal clouds simulated by the ecmwf model. *Monthly Weather Review* **127**, 25142531.

Kuo, H. L. (1965). On formation and intensification of tropical cyclones through latent heat release by cumulus convection. *J. Atmos. Sci.* **22**, 4063.

Lin, S. J. and Rood, R. B. (1996). Multidimensional ux form semi-lagrangian transport. *Monthly Weather Review* **124**, 2046–2068.

Liu, G. (2004). Approximation of single scattering properties of ice and snow particles for high microwave frequencies. *J. Atmos. Sci.* **61**, 2441–2456.

Lohmann, U. and Roeckner, E. (1996). Design and performance of a new cloud microphysics scheme developed for the echam4 general circulation model. *Climate Dynamics* **12**, 557–572.

Louis, J. F. (1979). A parametric model of vertical eddy fuxes in the atmosphere. *Boundary Layer Meteorology* **17**, 187–202.

Mace, G., Marchand, R., Zhang, Q., and Stephens, G. (2007). Global hydrometeor occurrence as observed by cloudsat; initial observations from summer 2006. *Geophys. Res. Lett.* **34**, L09808, doi:10.1029/2006GL029017.

Marchand, R., Haynes, J., Mace, G., Ackerman, T., and Stephens, G. (2009). A comparison of simulated cloud radar output from the multiscale modeling framework global climate model with cloudsat cloud radar observations. *J. Geophys. Res.* **114**, D00A20 (18 pp.).

Marchand, R., Mace, G., Ackerman, T., and Stephens, G. (2008). Hydrometeor detection using cloudsatan earth-orbiting 94-ghz cloud radar. *J. Atmospheric and Oceanic Technology* **25**, 519–533.

Mather, J., McFarlane, S., Miller, M., and Johnson, K. (2007). Cloud properties and associated radiative heating rates in the tropical western pacific. *J. Geophys. Res.* **112**, D05201, doi:10.1029/2006JD007555.

Medeiros, B. and Stevens, B. (2009). Revealing differences in gcm representations of low clouds. *Climate Dynamics* **doi: 10.1007/s00382-009-0694-5.**

Nam, C. (2007). *Representation of Cloud Overlap in a Climate Model: Evaluation with Satellite Data*. Master's thesis, International Space University, Strassbourg, France.

Neggers, R., Koehler, M., and Beljaars, A. (2009). A dual mass flux framework for boundary layer convection. part i: Transport. *J. Atmos. Sci.* **66**, 1465–1487.

Neggers, R., Siebesma, A., and G., L. (2004). An evaluation of mass flux closures for diurnal cycles of shallow cumulus. *Monthly Weather Review* **132**, 2525–2538.

Nordeng, T. (1994). *Extended versions of the convective parameterization scheme at ECMWF and their impact on the mean and transient activity of the model in the Tropics.*. Tech. rep., ECMWF 206, 41 pp.

Parol, F., Buriez, J., Vanbauce, C., Riedi, J., C.-Labonnote, L., Doutriaux-Boucher, M., Vesperini, M., Seze, G., Couvert, P., Viollier, M., and Breon, F. (2003). Review of capabilities of multi-angle and polarization cloud measurements from polder. *Advances in Space Research* **33**, 1080–1088.

Raschke, E., Ohmura, A., Rossow, W., Carlson, B., Zhang, Y.-C., Stubenrauch, C., and Kottek, M. (2005). Cloud effects on the radiation budget based on isccp data (1991 to 1995). *International Journal of Climatology* **25**, 1103–1125.

Ringer, M., McAvaney, B., Andronova, N., Buju, L., Esch, M., Ingram, W., Li, B., Quaas, J., Roeckner, E., Senior, C., Soden, B., Volodin, E., Webb, M., and Williams, K. (2006). Global mean cloud feedbacks in idealized climate change experiments. *Geophysical Research Letters* **33**, L07718, doi:10.1029/2005GL025370.

Roeckner, E., Buml, G., Bonaventura, L., Brokopf, R., Esch, M., Giorgetta, M., Hagemann, S., Kirchner, I., Kornblueh, L., Manzini, E., Rhodin, A., Schlese, U., Schulzweida, U., and Tompkins, A. (2003). *The Atmospheric General Circulation Model ECHAM5: Part 1. REPORT 349. ISSN 0937-1060*. Tech. rep., Max Planck Institute for Meteorology Hamburg, Germany.

Roeckner, E. and Esch, M. (2010). *Modifications to the trigger of cumulus convection in ECHAM5.*. Tech. rep., Max Planck Institute for Meteorology, Hamburg, Germany. Personal Communication (2010).

Rossow, W. and Schiffer, R. (1999). Advances in understanding clouds from isccp. *Bull. Amer. Meteor. Soc.* **80**, 27 pp.

Rossow, W., Walker, A., Beuschel, D., and Roiter, M. (1996). International satellite cloud climatology project (isccp) documentation of new cloud datasets. *World Meteorological Organization* **WMO/TD-No. 737**, 115 pp.

Raisanen, P., Barker, H., Khairoutdinov, M., and Randall, D. (2004). Stochastic generation of subgrid-scale cloudy columns for large-scale models. *Quarterly Journal of the Royal Meteorological Society* **130**, 20472067.

Schiffer, R.A.and Rossow, W. (1983). The international satellite cloud climatology project (isccp): The first project of the world climate research programme. *Bull. Amer. Meteorol. Soc.* **64**, 779–784.

Seethala, C. and Horváth, A. (2010). Global assessment of amsr-e and modis cloud liquid water path retrievals in warm oceanic clouds. *J. Geophys. Res.* **115(D13202)**, doi:10.1029/2009JD012662.

Siebesma, A., Bretherton, C., Brown, A., Chlond, A., Cuxart, J., Duynkerke, P., Jiang, H., Khairoutdinov, M., Lewellen, D., Moeng, C.-H., Sanchez, E., Stevens, B., and Stevens, D. (2003). A large eddy simulation intercomparison study of shallow cumulus convection. *Journal of Atmos. Sci.* **60**, 12011219.

Siebesma, A., Soares, P., and Teixeira, J. (2007). A combined eddy-diffusivity mass-flux approach for the convective boundary layer. *J. Atmos. Sci.* **64**, 12301248.

Siegenthaler-Le Drian, C. (2010). *Stratocumulus clouds in ECHAM5-HAM.*. Ph.D. thesis, Diss., Eidgenssische Technische Hochschule ETH Zrich, Nr. 18886. doi:10.3929/ethz-a-006073454.

Soden, B. and Held, I. (2006). An assessment of climate feedbacks in coupled oceanatmosphere models. *Journal of Climate* **19**, 3354–3360 .doi:10.1175/JCLI3799.1.

Solomon, S., Qin, D., Manning, M., Chen, Z., Marquis, M., Averyt, K., Tignor, M., and Miller, H. (2007). *Climate Change 2007: The Physical Science Basis, Contribution of Working Group I to the Fourth Assessment Report of the Intergovernmental Panel on Climate Change*. Tech. rep., United Nations Environment Programme: Intergovernmental Panel on Climate Change.

Stephens, G. (2005). Cloud feedbacks in the climate system: A critical review. *Journal of Climate* **18**, 237–273.

Stephens, G. L., Vane, D. G., Boain, R. J., Mace, G. G., Sassen, K., Wang, Z., Illingworth, A. J., O'Connor, E. J., Rossow, W. B., Durden, S. L., Miller, S. D., Austin, R. T., Benedetti, A., Mitrescu, C., and the CloudSat Science Team (2002). The cloudsat mission and the a-train: A new dimension to space-based observations of clouds and precipitation. *In Bull. Am. Met. Soc.* **83**, 1771–1790.

Stubenrauch, C., Del Geniom, A. D., and Rossow, W. B. (1997). Implementation of subgrid cloud vertical structure inside a gcm and its effect on the radiation budget. *J. Clim.* **10**, 273–287.

Sundqvist, H., Berge, E., and Kristjansson, J. (1989). Condensation and cloud studies with a mesoscale numerical weather prediction model. *Mon. Wea. Rev.* **117**, 16411657.

Svensson, G., Tjernstroem, M., and Koracin, D. (2000). The sensitivity of a stratocumulus transition: Model simulations of the astex first lagrangian. *Boundary-Layer Meteorol.* **95**, 5790.

Tanelli, S., Durden, S., Im, E., Pak, K., Reinke, D., Partain, P., Marchand, R., and Haynes, J. (2008). Cloudsats cloud profiling radar after 2 years in orbit: performance, external calibration, and processing. *IEEE Transactions on Geoscience and Remote Sensing* **46**, Issue 11; pp. 3560–3573.

Tiedtke, M. (1989). A comprehensive mass flux scheme for cumulus parameterization in large-scale models. *Monthly Weather Review* **117**, 1779–1800.

Tompkins, A. M. (2002). A prognostic parameterization for the subgrid-scale variability of water vapor and clouds in large-scale models and its use to diagnose cloud cover. *J. Atmos. Sci.* **59**, 19171942.

Vergados, P. and Shepherd, M. (2009). Retrieving mesospheric water vapour from observations of volume scattering radiances. *Ann. Geophys.* **27**, 487501.

Von Salzen, K. and McFarlane, N. (2002). Parameterization of the bulk effects of lateral and cloud-top entrainment in transient shallow cumulus clouds. *J. Atmos. Sci.* **59**, 14051430.

Webb, M., Bony, S., Tselioudis, G., and Bretherton, C. (2007). *The Cloud Feedback Model Inter-comparison Project - Plans for CFMIP-2 Summary of key issues for WGCM meeting (3-5 September, 2007).* Tech. rep., The Cloud Feedback Model Inter-comparison Project.

Webb, M., Senior, C., Bony, S., and Morcrette, J.-J. (2001). Combining erbe and isccp data to assess clouds in the hadley centre, ecmwf and lmd atmospheric climate models. *Climate Dynamics* **17**, Issue 12, pp. 905–922.

Winker, D. (2003). Accounting for multiple scattering in retrievals from space lidar in lidar multiple scattering experiments. *Proc. SPIE Int. Soc. Opt. Eng.* **5059**, 128 139.

Winker, D., Hostetler, C., Vaughan, M., and Omar, A. (2006). *CALIOP algorithm theoretical basis document Part 1 : CALIOP Instrument and Algorithms Overview Release 2.0*. Tech. rep., NASA Langley Research Center PC-SCI-202 Part 1.

Winker, D., Vaughan, M., Omar, A., Hu, Y., Powell, K., Liu, Z., Hunt, W., and Young, S. (2009). Overview of the calipso mission and caliop data processing algorithms. *J. Atmospheric and Oceanic Technology* **26**, 23102323.

Winker, D. M., Hunt, W., and McGill, M. (2007). Initial performance assessment of caliop. *Geophys. Res. Lett.* **34**, L19803,doi:10.1029/2007GL030135.

Winker, D. M., Hunt, W. H., and Hostetler, C. A. (2004). Status and performance of the caliop lidar. *Proc. SPIE* **5575**, 8–15.

Wyser, K. (1998). The effective radius in ice clouds. *J. Climate* **11**, 1793–1802.

Xie, P. and Arkin, P. (1997). Global precipitation: A 17-year monthly analysis based on gauge observations, satellite estimates, and numerical model outputs. *Bull. Amer. Meteor. Soc.* **78**, 25392558.

Die gesamten Veröffentlichungen in der Publikationsreihe des MPI-M
„Berichte zur Erdsystemforschung“,
„Reports on Earth System Science“,
ISSN 1614-1199

sind über die Internetseiten des Max-Planck-Instituts für Meteorologie erhältlich:

http://www.mpimet.mpg.de/wissenschaft/publikationen.html



ISSN 1614-1199